MINERAL TRANSFORMATION OF ACID MINE DRAINAGE IN A LIMESTONE ENVIRONMENT, ZIMAPÁN, MEXICO

A Dissertation

by

LUKE ROBERT MORGAN

Submitted to the Office of Graduate and Professional Studies of
Texas A&M University
in partial fulfillment of the requirements for the degree of

DOCTOR OF PHILOSOPHY

Chair of Committee,	Youjun Deng
Committee Members,	Sam Feagley
	Bruce Herbert
	Arthur Schwab
Head of Department,	David Baltensperger

December 2017

Major Subject: Soil Science

ABSTRACT

After mining operations extract the desired profitable minerals, the large amount of waste remaining can pose a potential environmental hazard due to high concentrations of heavy metals and acid generated by the oxidation of sulfide minerals. The corresponding unearthed mine waste is commonly stored in large open heaps, exposed to weather, leading to cascading geochemical changes that require additional land reclamation. Such a problem occurred in Zimapán, Mexico, known for its mining of copper, zinc, and lead. Operations for approximately 60 years left over 1 million tonnes of mine tailings leading to acid mine drainage (AMD), consequently now in drastic need of remediation. Zimapán lies in an area of limestone-rich bedrock and sediment, which is commonly ground and used to neutralize acidity. Unfortunately, the region still has acidic leachates present and AMD persists as a problem.

The purpose of this research was to better understand mineral transformation, acid generation, and heavy metal mobilization/immobilization in mine tailings in Zimapán, Mexico. This specific region has a unique arid climate and encompasses a limestone geological environment, making it suitable to be a geochemical model applicable for other mine sites around the world with similar environments. The objectives of this study were: 1) to characterize mineral phases and nanoparticles, 2) assemble a comprehensive mineralogical report of the tailing sites located in Zimapán, Mexico, and 3) to identify the arsenic and iron speciation and geochemical processes affected by the carbonate-rich environment.

Mineralogical analysis determined the presence of jarosite, plumbojarosite, goethite, ferrihydrite, hematite, galena, lepidocrocite, scorodite, arsenopyrite, pyrite, garnet, albite, sphalerite, calcite, dolomite, gypsum, mica, chlorite, montmorillonite, and ver-

miculite in mining waste and the surrounding soil. Where the tailings were stored, finding soil and water pH<1 was not rare, but the average was pH 2.5. These highly acidic conditions occurred after the oxidation and dissolution of iron sulfide minerals with sufficient precipitation or moisture, allowing for metal desorption and increasing their mobility. Likewise, the arid environment helped precipitate soluble salts and increase the formation of stable iron oxides that are able to absorb metals.

Heavy metal contamination was prevalent, notably: copper, zinc, lead, and arsenic. With a dangerous amount of arsenic (maximum concentration found was 110,000 mg/kg) it was primarily seen in forms of As^{1-} in arsenopyrite and As^{5+} in scorodite and absorbed iron oxides and to other minerals such as jarosite. Dissolution and re-precipitation of solid phases directly affect heavy metal transformations and translocation. Poorly crystalline nanoparticles of iron oxides and silica are easily susceptible to geochemical changes due to their high surface area, structural defects, high surface charge, and variation of elements in their structure.

Fortunately, metal contaminants in the tailing waste were incorporated into mineral phases before and after oxidation, or sorbed to oxides after oxidation. Lower concentrations of contamination were found in soluble sulfates, suggesting they are not available for release after their original dissolution and yet still exist in the new precipitate. In the soluble sulfates, samples on average had about 25% Fe, up to 6854 mg/kg Cu, up to 465,104 mg/kg Zn, up to 4544 of As, and up to 670 mg/kg of Pb present. Lead showed low bioavailability, consistently found associated with jarosite phases. Similarly, arsenic was incorporated in arsenopyrite, scorodite, or sorbed to iron oxides. Primary ferrous sulfide minerals, such as pyrite and pyrrhotite, were abundant. There were also large amounts of ferric iron in iron oxides and sulfates such as copiapite, goethite, and jarosite.

CONTRIBUTORS AND FUNDING SOURCES

This project was partially funded by Consejo Nacional de Ciencia y Tecnologia (CONACYT), a collaborative research grant program that made this research possible. The program brought Texas A&M University (TAMU) and University of Mexico (UNAM) together to collaborate their technical and scholarly activities; in addition, helped harbor a relationship between two universities that still continues today.

Graduate committee for this dissertation is Youjun Deng, Sam Feagley, Bruce Herbert, and Paul Schwab.

Teaching assistance scholarship was provided by TAMU Department of Soil & Crop Sciences.

NOMENCLATURE

AAS	Atomic Adsorption Spectroscopy
AMD	Acid Mine Drainage
ANC	Acid Neutralization Capacity
AOD	(Acid) Ammonium Oxalate in Darkness is a method to separate noncrystalline soil portion with Fe, Al, and Mn.
ARD	Acid Rock Drainage
Arduino	A set of open-source hardware components and software designed for easy microcontroller board projects that integrate custom user code.
Athena	XAS analysis software
ATSDR	Agency for Toxic Substances and Disease Registry is part of the U.S. Department of Health and Human Services
AVS	Acid Volatile Sulfide
CAA	Clean Air Act. CAA requires EPA to set NAAQS for 6 criteria pollutants: ground-level ozone, PM, carbon monoxide, nitrogen oxides, sulfur dioxides, and lead.
CDC	U.S. Centers for Disease Control and Prevention
CEC	Cation Exchange Capacity
Clay Fraction	< 2 μm sized particles
Clay Minerals	Phyllosilicate minerals and to minerals which impart plasticity to clay and which harden upon drying or firing

CONACYT	Consejo Nacional de Ciencia y Tecnologia, translates to National Council for Science and Technology
CWA	Clean Water Act
Data Viewer	XRF analsysis software
DCB Treatment	Sodium Dithionite-Citrate-Bicarbonate solutions used to remove iron
EPA	U.S. Environmental Protection Agency
EVA	XRD analysis software
FDA	U.S. Food and Drug Administration
FTIR	Fourier Transform Infrared Spectroscopy
GIS	Geographical Information System
GPS	Global Positioning System
HAPs	Hazardous air pollutants
IARC	International Agency for Research on Cancer is a specialized part of WHO
LC-LSF	Linear combination, least-square fitting
LD_{50}	Lethal dose to kill 50% of experimental population
NAAQS	National Ambient Air Quality Standards set by EPA
NESHAP	National Emission Standards for Hazardous Air Pollutants
NIH	U.S. National Institute of Health
NP	Neutralization Potential
NPL	National Priorities List
OM	Organic matter
PM	Atmospheric particulate matter or atmospheric aerosol

PM_{10}	PM $\leq$ 10 μm in diameter
PRB	Permeable Reactive Barrier
PZC	Point of zero charge
PZNPC	Point of zero net proton charge
RBA	Relative Bioavailability
RCRA	Resource Conservation and Recovery Act
Rietveld method	Refinement method for characterizing crystalline structures particularly patterns from neutron and x-ray diffraction
ROS	Reactive oxygen species
RRC	Railroad Commission of Texas (a.k.a. Texas Railroad Commission, TRC)
Sand Fraction	>53 μm sized particles
SEM	Scanning Electron Microscope
Silt Fraction	2 - 53 μm sized particles
SOM	Soil organic matter
Superfund	U.S. Government program to clean hazardous waste sites
TAMU	Texas A&M University
TEM	Transmission Electron Microscope
TCLP	Toxicity Characteristic Leaching Procedure
UNAM	Universidad Nacional Autónoma de México, translates to National Autonomous University of Mexico
USDA	U.S. Department of Agriculture
USGS	U.S. Geological Survey
UST	Underground Storage Tank

VOC	Volatile organic carbon
WHO	World Health Organization is the governing health authority within the United Nations
XAS	X-Ray Absorption Spectroscopy
XRD	X-Ray Diffraction or X-Ray Diffractometer
XRD Commander	XRD instrument control software
XRF	X-Ray Florescence Spectroscopy

TABLE OF CONTENTS

Page

LIST OF FIGURES

FIGURE Page

LIST OF TABLES

1. INTRODUCTION AND LITERATURE REVIEW OF ACID MINE DRAINAGE AND ITS OCCURRENCE IN THE MINING DISTRICT OF ZIMAPÁN, MEXICO

1.1 Acid Mine Drainage

Acid mine drainage (AMD), or acid rock drainage (ARD) is the release of acid and metal-polluted waters from some mining activities. A physically stable pile of mine waste can expel a significant amount of environmentally harmful runoff (Figure 1.1). If present, pyrite and pyrrhotite will oxidize to produce strongly acidic leachates. These iron sulfides, once exposed to air and water after mining operations, will produce AMD unless neutralized with an alkaline compound, usually a derivative of lime or limestone (Johnson and Hallberg, 2005; Akcil and Koldas, 2006).

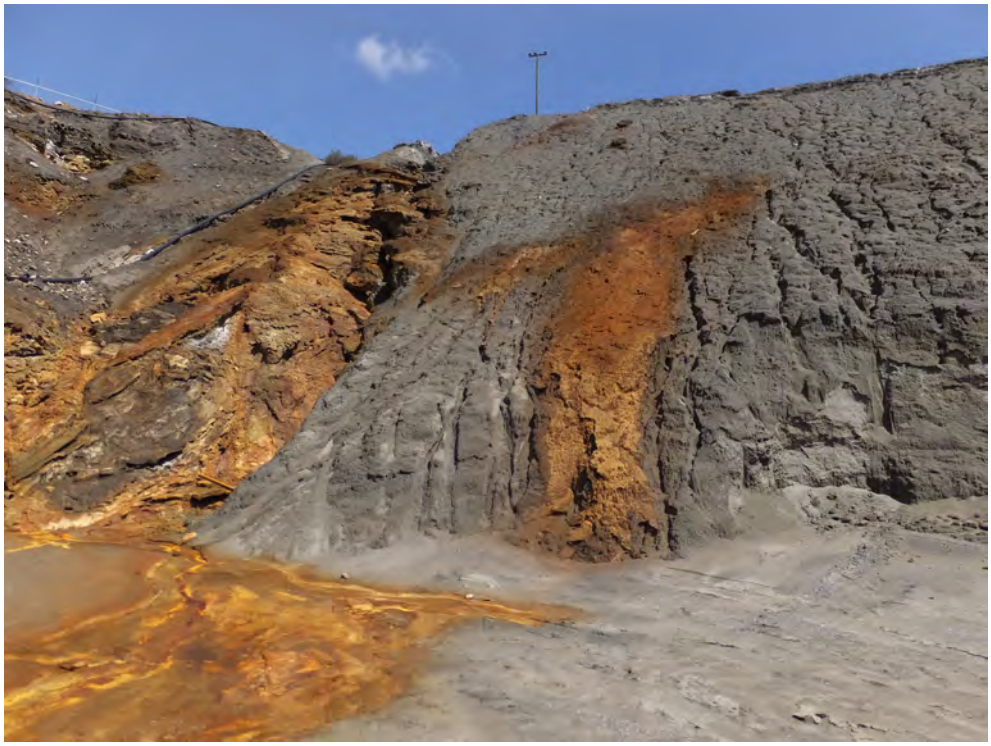

Figure 1.1: Acid mine drainage runoff from a tailing pile at San Miguel Viejo Mine (SMV).

Acid mine drainage and sulfide mineral geochemistry are closely related because sulfur is common mining overburden. The oxidation of pyritic material in mining waste can generate AMD for centuries or longer (Kalin et al., 2006).

The process that produces AMD by oxidation of iron sulfides that were exposed to air and water has been studied extensively (Kalin et al., 2006) and four chemical reactions contribute to the AMD process: iron sulphide oxidation (eq. 1.1), ferrous iron oxidation (eq. 1.2), ferric iron hydrolysis (eq. 1.3), and the oxidation of ferrous sulfide by ferric iron (eq. 1.4), or by both ferric iron and oxygen (eq. 1.5) (Johnson and Hallberg, 2005; Akcil and Koldas, 2006).

$$FeS_2 + \frac{7}{2}\,O_2 + H_2O \longrightarrow Fe^{2+} + 2\,{SO_4}^{2-} + 2\,H^+ \tag{1.1}$$

$$Fe^{2+} + \frac{1}{4}\,O_2 + H^+ \longrightarrow Fe^{3+} + \frac{1}{2}\,H_2O \tag{1.2}$$

$$Fe^{3+} + 3\,H_2O \longrightarrow Fe(OH)_3 + 3\,H^+ \tag{1.3}$$

$$14\,Fe^{3+} + FeS_2 + 8\,H_2O \longrightarrow 15\,Fe^{2+} + 2\,{SO_4}^{2-} + 16\,H^+ \tag{1.4}$$

$$FeS_2 + \frac{13}{2}\,Fe^{3+} + \frac{15}{8}\,O_2 + \frac{17}{4}\,H_2O \longrightarrow \frac{15}{2}\,Fe^{2+} + 2\,{SO_4}^{2-} + \frac{17}{2}\,H^+ \tag{1.5}$$

The first three reactions (eq. 1.1-1.3) can be simplified to show the production of $Fe(OH)_3$ (eq. 1.6).

$$FeS_2 + \frac{15}{4}\,O_2 + \frac{7}{2}\,H_2O \longrightarrow Fe(OH)_3 + 2\,{SO_4}^{2-} + 4\,H^+ \tag{1.6}$$

Iron oxide products can also be reduced back to ferrous iron (eq. 1.7) (Akcil and Koldas, 2006; Cheng et al., 2009; Kuyucak, 2012).

$$Fe(OH)_3 + 3\,H^+ + e^- \longrightarrow Fe^{2+} + 3\,H_2O \tag{1.7}$$

Secondary minerals affecting the migration of heavy metals have been studied before, specifically at a gold mine in Russia. The gold mine had As precipitate with iron sulfur arsenates (i.e. scorodite and hidalgoite) and in jarosite-beudantite (i.e. $Pb_{0.97}K_{0.03}Fe_{2.84}(SO_4)_{1.03}(AsO_4)_{0.97}(OH)_{5.52}$) phases (Roca et al., 1999). These newly formed phases develop a hardened layer that inhibited pore space and made piles discharge rain water at that layer, also leading to an accumulation of AMD

and metals. Discharged rain water that quickly evaporated on the side of waste piles became sulfate salts, until the next heavy rainfall that washed them away in concentrated amounts (Giere et al., 2003).

Different intermediates and temporary iron oxides may form depending on environmental factors such as low pH and available water. Iron oxides and sulfates can readily form in the AMD conditions (eq 1.8 - 1.11).

$$\frac{1}{2}\,Fe_2(SO_4)_3 + 2\,H_2O \longrightarrow \underset{\text{Goethite or lepidocrocite}}{FeOOH} + \frac{3}{2}\,H_2SO_4 \tag{1.8}$$

$$4\,Fe_2(SO_4)_3 + 14\,H_2O \longrightarrow \underset{\text{Schwertmannite}}{Fe_8O_8(OH)_6SO_4} + 11\,H_2SO_4 \tag{1.9}$$

$$\frac{3}{2}\,Fe_2(SO_4)_3 + 6\,H_2O + K^+ \longrightarrow \underset{\text{Jarosite}}{KFe_3(OH)_6(SO_4)_2} + \frac{5}{2}\,H_2SO_4 + H^+ \tag{1.10}$$

$$Fe^{2+} + 4\,Fe^{3+} + 6\,{SO_4}^{2-} + 22\,H_2O \longrightarrow \underset{\text{Copiapite}}{Fe^{2+}{Fe_4}^{3+}(SO_4)_6(OH)_2 \cdot 20\,H_2O} + 2\,H^+ \tag{1.11}$$

Other iron oxide intermediates can form during the process of pH cycling low to high, and environmental changes. For example, magnetite can lead to many iron oxides, such as jarosite can lead to goethite, or magnetite (Moncur et al., 2009):

$$\underset{\text{magnetite}}{Fe^{2+}{Fe_2}^{3+}O_4} + \frac{1}{4}\,O_2 + \frac{9}{2}\,H_2O \longrightarrow 3\,Fe(OH)_3 \tag{1.12}$$

and eventually acidic conditions could redissolve the mineral phase again. Meanwhile, jarosite can incorporate and release cations to the surrounding environment. A general order of incorporation of metals by jarosite is $Cu^{2+} > Zn^{2+} > Co^{2+}$ / Ni^{2+}

/ $Mn^{2+} > Cd^{2+}$ (Dutrizac and Jambor, 2000; Stoffregen et al., 2000).

$$KFe_3(SO_4)_2(OH)_6 \longrightarrow 3\,FeO(OH) + K^+ + 2\,{SO_4}^{2-} + 3\,H^+ \tag{1.13}$$

$$KFe_3(SO_4)_2(OH)_6 \longrightarrow \frac{3}{2}\,Fe_2O_3 + K^+ + 2\,{SO_4}^{2-} + 3\,H^+ + \frac{3}{2}\,H_2O \tag{1.14}$$

$$KFe_3(SO_4)_2(OH)_6 + 3\,H^+ + {SO_4}^{2-} \longrightarrow 3\,\underset{\text{butlerite}}{Fe(SO_4)(OH)} + K^+ + 3\,H_2O \tag{1.15}$$

Primary iron sulfides and sulfates can incorporate metals at almost any point of their transformation. After the dissolution of primary sulfides and low pH dominates, sulfates and oxides are abundant in different forms (Dutrizac and Jambor, 2000).

$$2\,FeSO_4 + H_2SO_4 + \frac{1}{2}\,O_2 \longrightarrow Fe_2(SO_4)_3 + H_2O \tag{1.16}$$

1.2 Heavy Metals in the Environment

Heavy metals are generally defined as metallic chemical elements with high atomic weight and cannot be degraded or destroyed. These metal elements naturally occur in the environment, representing a risk for humans when exposed to high concentrations. Common heavy metals with the greatest public interest are As, Hg, Pb, Cd, Cr, Tl, and Sb due to their toxicity. Elements such as As, Cd, Cr, Pb, and Hg are toxic enough to be considered public health risks. In addition, they are human carcinogens (known or probable) according to the Environmental Protection Agency (EPA), and the International Agency for Research on Cancer (IARC) (Tchounwou et al., 2012). Mineral transformations from primary sulfides to secondary structures can affect a heavy metal's bioavailability at any given time. The dissolution

of As-bearing primary sulfide minerals can be the start of many environmental concerns (Dutrizac and Jambor, 2000; Majzlan et al., 2014; Ramirez-Aldaba et al., 2016; Corkhill and Vaughan, 2009).

$$\underset{\text{arsenopyrite}}{2\,\mathrm{FeAsS}} + 5\,\mathrm{O_2} \longrightarrow \underset{\text{hematite}}{\mathrm{Fe_2O_3}} + \underset{\text{arsenolite}}{\mathrm{As_2O_3}} + 2\,\mathrm{SO_2} \tag{1.17}$$

$$\underset{\text{arsenolite}}{\mathrm{As_2O_3}} + \mathrm{O_2} + 3\,\mathrm{H_2O} \longrightarrow 2\,\mathrm{H_2AsO_4^-} + 2\,\mathrm{H^+} \tag{1.18}$$

$$3\,\mathrm{FeAsS} + 3\,\mathrm{H_2O} \longrightarrow \underset{\text{orpiment}}{\mathrm{As_2S_3}} + 3\,\mathrm{Fe^{2+}} + \mathrm{H_3AsO_3} + 3\,\mathrm{H^+} + 9\,\mathrm{e^-} \tag{1.19}$$

$$\mathrm{FeAsS} \longrightarrow \mathrm{Fe^{2+}} + \frac{1}{2}\underset{\text{realgar}}{\mathrm{As_2S_2}} + 2\,\mathrm{e^-} \tag{1.20}$$

In acidic conditions, the dissolution of arsenopyrite to realgar(As_2S_2) can create arsenic oxides and additional acidity (Corkhill and Vaughan, 2009).

$$\mathrm{As_2S_2} + 14\,\mathrm{H_2O} \longrightarrow 2\,\mathrm{H_3AsO_3} + 2\,\mathrm{SO_4^{2-}} + 22\,\mathrm{H^+} + 18\,\mathrm{e^-} \tag{1.21}$$

$$\mathrm{H_3AsO_3} + \mathrm{H_2O} \longrightarrow \mathrm{H_3AsO_4} + 2\,\mathrm{H^+} + 2\,\mathrm{e^-} \tag{1.22}$$

Iron oxides are found globally at sites near deposits of mine waste. Iron oxides and their derivatives are either crystalline or in the short range ordered forms. They have been used in industry for pigments and vary in color from yellow and red to black. Their structure and particle size can affect their color. The specific surface area of

iron oxides are normally large due to their small particle size, which is a few microns to a few nanometers. The surface area is directly related to the mineral's reactivity of dissolution and dehydroxylation, sorbent efficiency, phase transformations, and thermodynamic stability (Cornell and Schwertmann, 2003). Manganese oxides (i.e. pyrolusite) have a high exchange capacity due to their large specific surface area and can convert As(III) to As(V) (Vodyanitskii, 2009).

The solubility of iron oxides are generally low except in conditions with low pH. Commonly, Fe^{3+} oxides have a low solubility and Fe^{2+} oxides are sparingly soluble. Isomorphic substitution also affects solubility, such as Al in hematite and goethite can increase their stability and decrease solubility. Another factor that can control solubility is the solid phase's age, whether is it is freshly precipitated or aged to inactivity (Cornell and Schwertmann, 2003).

The adsorption capacity of a soil is determined by its threshold for ion substitution. Adsorption of metal ions is correlated to properties such as redox potential, pH, clay type, SOM, Fe and Mn oxides, and calcium carbonate content. Soil factors and solvent properties can also affect the adsorption process.

There is evidence that cation competition exists for adsorption sites, but some studies show inconclusive or contradicting results. Adsorption site competition can change at different pH ranges, concentration, and the types of cations involved. At low concentrations when mineral surface sites are not all filled there can be no competition and thus no limit of adsorption. Additionally, systems where organic ligands adsorb to soil surfaces may enhance metal adsorption by complexation of the surface-adsorbed ligand.

Soil part	Relative order of sorption
Goethite	Cu > Pb > Zn > Co > Cd
Fe oxide	Pb > Cu > Zn > Cd
Montmonorillonite	Cd = Zn > Ni
Kaolinite	Cd > Zn > Ni
Soils	Pb > Cu > Zn/Cd/Ni

Table 1.1: Affinity of metals for soil surfaces (McLean and Bledsoe, 1992).

Arsenic can be found in the environment from natural or anthropogenic sources. Arsenic occurs commonly in the oxidation states -1, 0, +3, +5, with As(III) and As(V) being the most abundant. Arsenic compounds are normally categorized into either inorganic, organic, or arsine gas. Arsenic speciation depends on multiple factors such as redox conditions, pH, biological activity, salinity, and distance from source. In water with limited oxygen, such as deep wells (reducing conditions) arsenites are abundant. Biological mechanisms are able to convert inorganic arsenic compounds to methylated arsenic acids (IARC, 2012). In drinking-water, arsenic primarily occurs as arsenate (AsO_4^{3-}), but it is possible to have high levels of arsenite (AsO_3^{3-}) exist in reduced environments. Trace amounts of methylated species are found more often in biological systems (IARC, 2012).

Copper is an essential micronutrient for plants and is taken up in the form of Cu^{2+}. Copper is important for enzymes in lignin formation in cell walls and for processes such as photosynthesis, respiration, and nitrogen processing. Specifically, Cu is used in CO_2 assimilation, ATP synthesis, comprise plastocyanin (photosynthesis protein), cytochrome oxidase (for the electron transport chain). There has been an increase

in copper in ecosystems due to industrialization, but there are also soils with copper deficiencies. Soils with excess Cu can induce cytotoxic effects in plants such as stress, hinder growth, leaf chlorosis, and increase reactive oxygen species (ROS). Oxidative stress caused by excess Cu can disturb metabolic pathways and damage macromolecules (Yadav, 2010). Two components that strongly affect coppers is soil pH and OM. Organic matter can lower the amount of copper available to plants by limiting mineral fixation, leaching, and availability to plants. Potential copper minerals are chalcopyrite ($CuFeS_2$), chalcocite (Cu_2S), covellite (CuS), and bornite (Cu_5FeS_4). They can experience the following redox reactions (Zeng et al., 2013):

$$CuFeS_2 \longrightarrow \frac{3}{4}\,CuS + \frac{5}{4}\,S^o + \frac{1}{4}\,Cu^{2+} + Fe^{2+} + \frac{5}{2}\,e^- \tag{1.23}$$

$$CuS \longrightarrow S^o + Cu^{2+} + 2\,e^- \tag{1.24}$$

$$CuFeS_2 \longrightarrow Cu^{2+} + Fe^{2+} + 2\,S^o + 4\,e^- \tag{1.25}$$

And in acidic conditions (Lu et al., 2016):

$$CuFeS_2 + 2\,H^+ \longrightarrow CuS + H_2S + Fe^{2+} \tag{1.26}$$

Lead occurs naturally in the environment and also released from anthropogenic sources because its of usefulness in fuels, mining, agriculture, and manufacturing. Lead is released from the use of fossil fuels, lead-acid batteries, ammunitions, solder, paint, chemicals, and x-ray shielding. This use of lead in certain products have been reduced or eliminated, but there are still very high levels present in homes. The greatest risk of lead consumption is to small children, whereas it can be contracted by old paint, dust, or direct contact with soil. Lead can also be consumed through contam-

inated drinking water (Tchounwou et al., 2012). Potential lead minerals are galena PbS, anglesite $PbSO_4$, cerussite $PbCO_3$, and plumbojarosite $PbFe_6^{3+}(SO_4)_4(OH)_{12}$.

The mineral galena can provide sulfur, a precursor for other sulfate minerals. Lead sulfide can transform to lead sulfate and other mineral species through many pathways (Li and Qvarfort, 1996; Dutrizac and Jambor, 2000):

$$PbS + 2\,Fe^{3+} + \frac{3}{2}\,O_2 + H_2O \longrightarrow PbSO_4 + 2\,Fe^{2+} + 2\,H^+ \tag{1.27}$$

$$PbS + H_2SO_4 + \frac{1}{2}\,O_2 \longrightarrow Pb(SO_4) + S^o + H_2O \tag{1.28}$$

$$PbSO_4 + 3\,Fe_2(SO_4)_3 + 12\,H_2O \longrightarrow 2\,[\underset{\text{Plumbojarosite}}{Pb_{0.5}Fe_3(SO_4)_2(OH)_6}] + 6\,H_2SO_4 \tag{1.29}$$

$$PbSO_4 + CuSO_4 + Fe_2(SO_4)_3 + 6\,H_2O \longrightarrow \underset{\text{Beaverite}}{Pb(Fe_2Cu)(SO_4)_2(OH)_6} + 3\,H_2SO_4 \tag{1.30}$$

Zinc is another micronutrient that can be detrimental in excess. Human activies leading to contaminated ecosystems include sewage sludge, urban compost, fertilizers, emissions from municipal waste incinerators, residues from metalliferous mining, metal smelting, amongst others. Excess levels of zinc can hurt plant metabolic functions leading to stunted growth and senescence. Plants with too much zinc have limited root and shoot growth. Zinc can also contribute to chlorosis in leaves of plants. Chlorosis is partially created by iron deficiency as hydrated Zn^{2+} and Fe^{2+} are similar in size (Yadav, 2010). Potential zinc minerals are smithsonite $ZnCO_3$, sphalerite ZnS, zincite ZnO, and willemite Zn_2SiO_4.

The mineral sphalerite can provide sulfur, a precursor for other sulfate minerals (Li and Qvarfort, 1996; Moncur et al., 2009; Dutrizac and Jambor, 2000).

$$\mathrm{ZnS} + 2\,\mathrm{O_2} \longrightarrow \mathrm{Zn^{2+}} + \mathrm{SO_4}^{2-} \tag{1.31}$$

$$\mathrm{ZnS} + 2\,\mathrm{Fe^{3+}} + \frac{3}{2}\,\mathrm{O_2} + \mathrm{H_2O} \longrightarrow \mathrm{Zn^{2+}} + 2\,\mathrm{Fe^{2+}} + 2\,\mathrm{H^{+}} + 1\,\mathrm{SO_4}^{2-} \tag{1.32}$$

$$\mathrm{ZnS} + \mathrm{H_2SO_4} + \frac{1}{2}\,\mathrm{O_2} \longrightarrow \mathrm{ZnSO_4} + \mathrm{S^o} + \mathrm{H_2O} \tag{1.33}$$

$$\mathrm{ZnS} + \mathrm{Fe_2(SO_4)_3} \longrightarrow 2\,\mathrm{FeSO_4} + \mathrm{ZnSO_4} + \mathrm{S^o} \tag{1.34}$$

1.3 Geochemistry of Poorly Crystalline Nanoparticles Formed in Acid Mine Drainage and Their Fate in a Limestone Environment

Arsenic, zinc, lead, copper, nickel and other heavy metals are the major concerns of acid mine drainage, which results from the oxidation of sulfide minerals exposed to moisture and air (Cheng et al., 2009). Liming is one of the most common practices used in the remediation of acid mine tailing and in reclamation of disturbed land containing sulfide minerals. Limestone can neutralize acidity and precipitate heavy metals as hydroxides, oxides, or other species, which can be flocculated into high density sludge (Akcil and Koldas, 2006). For example, treating a lab-made simulated acid mine drainage solution with limestone removed 99.9% As and decreased the concentration in solution from 34.00 mg/L to 0.04 mg/L by co-precipitation with Fe-hydroxides (Romero et al., 2011; Labastida et al., 2013). In theory, acid mine drainage and heavy metal contamination should not occur in limestone sediments due to the abundance of carbonate minerals that can neutralize the acidity.

Several reports from Mexico, USA, Europe, New Zealand, and South America have shown that strongly acidic materials that have a pH as low as one or two are

common in oxidized mine tailings that are originated from skarn deposits in limestone sediments (Armienta et al., 2012).

1.4 Co-precipitation of Arsenic in Nanoparticles and Colloids of Acid Mine Drainage

The processes controlling the transformation and transport of arsenic in acid mine drainage are well known (Cheng et al., 2009). When iron hydroxides or iron hydroxyoxides precipitate upon neutralization of the acidity, rapid arsenic removal from the solution can occur either through co-precipitation (Burton et al., 2010; Carlson et al., 2002), or the formation of inner-sphere and outer-sphere complexes (Asta et al., 2009; Cheng et al., 2009). Jarosite can form in acid mine drainage and it can incorporate As and Pb in its structure (Figueiredo and da Silva, 2011; Savage et al., 2005). The incorporated As can be released by abiotic or biotic processes to the environment when the pH is increased (Smith et al., 2006; Smeaton et al., 2012).

Newly formed colloids and nanoparticles can play significant roles in the transformation and transport of arsenic and the other heavy metals due to their large specific surface area, abundant structural defects, and incorporation of several elements in their structures. These factors make the colloids and nanoparticles more susceptible to environmental changes and therefore, they can regulate the chemistry of problematic arsenic and heavy metals in surface water and ground water.

1.5 Using Zimapán as an Analog for AMD in Arid, Carbonate-Rich Environments

The area in which Zimapán is located is unique overall but a representative location that can share individual characteristics with other mine sites; characteristics such as geology, climate, precipitation, topography, or vegetation. The mining region of Zimapán, Mexico lies in an arid, mountainous, calcareous environment that has its advantages and disadvantages. The mountain valley that contains the tailings

makes hydrological paths with distinct slope and direction. In addition, the arid environment with low precipitation and high evaporation could lessen the effects of AMD. However, they can be more susceptible to dust storms and erosion due to lack of vegetation (Razo et al., 2004). Analogs are important as they can provide foresight for a site's risk and reclamation issues. An area with the same climate and contaminant characteristics as Zimapán, Mexico could potentially offer the same reclamation methodologies.

In the semi-arid city of Matehuala, state of San Luis Potosí, Mexico there is an area that has been mined for more than 200 years. Matehuala is about 6 hours North of Zimapán, but has similar metal contaminants. Their maximum levels of contamination were 17,384 mg kg^{-1} As, 7,200 mg kg^{-1} Cu, and 3,450 mg kg^{-1} Pb. Rainfall storage ponds contained up to 265 μg L^{-1} As and one particular water source had $>$ 5900 μg L^{-1} (Razo et al., 2004). Matehuala and Zimapán are both located inside the Sierra Madre Oriental and mined for lead and copper.

In Morocco, due to similar arid climatic effects, the lack of vegetation and lack of soil protection from weather and erosion make land management difficult. They attributed their metal contamination spreading to mining wastes and its moving downstream after rainfall (Khalil et al., 2013). Zimapán, Mexico can encounter the same issues because of its mountainous topography and its close proximity to the Toliman River. The bare heaps of tailings are highly vulnerable to erosion and weathering.

Kempton and Atkins (2000) pointed out that the top few centimeters of soil and tailings are dried in arid environments, slowing sulfide oxidation compared to deeper subsurface conditions. Although, that couple centimeter crust would be insignificant considering the size of large storage areas. The diffusion of oxygen into pore spaces is related to moisture content, therefore the lack of water (which otherwise prevents

diffusion) could increase sulfide oxidation rates in arid environments. They also warned that there are delayed effects from AMD in arid environments. As water is collected in areas and repeatedly evaporated and filled, the water and sediment become loaded with contaminates until a threshold is met.

Dust plays a key part in contaminant transport in Zimapán, Mexico mine tailings (Espinosa et al., 2009). Wind speed and relative humidity are variables in determining dust concentrations, aerosol emissions, and transport. In Juárez, Chihuahua, Mexico dust concentrations increased as the humidity increased until reaching a maximum of 25% where dust then decreased with relative humidity. This is due to soil humidity decreasing particle cohesion before saturation (Csavina et al., 2014).

One location in semi-arid Arizona contains a superfund site that has similar Pb mineralogy as Zimapán, Mexico (Hayes et al., 2012) and had both plumbojarosite ($PbFe_6(SO_4)_4$ $(OH)_{12}$) and anglesite ($PbSO_4$), the latter was found to be the more bioaccessible Pb phase. Plumbojaraosite is considered low bioavailability and anglesite is medium, compared to soluble lead acetate. It was observed that Pb accumulated in the clay size fraction, so airborne contamination is a vector for transport and health risks.

Stuben et al. (2001) studied the carbonate host rock historical mining area in Wiesloch, Germany known for their Ag, Pb, and Zn mining. The mining activities in this area have been going on for over two millennia. The tailing heaps are similar to Zimapán because they are bare and need cover to prevent transport of contaminants. In Germany, it was proposed to put available organic-rich municipal sewage sludge on top of the heap for coverage. This could be possible as calcite-saturated solutions have been proven to be viable, over even better than similar dry covers (Smart et al., 2010).

The mine tailings in and around Zimapán, Mexico, were chosen as our study

subject for a number of reasons. First, the Zimapán District is known for its heavy metal contamination from the mining industry, guaranteeing a contaminated sample at every location and eliminating the need to search for adequate research samples. Arsenic was the original contaminant of interest and the region was previously reported to contain such minerals, natural and anthropogenic. Second, the locations were not difficult to be reached from Mexico City, Mexico, as the roads were adequately maintained, although not all were paved. Third, all the tailing sites were still in operation and maintained by a corporation which helped their accessibility.

The geology of Zimapán, Mexico combined with the metal contamination made the location a good candidate for research too. The mining of metals in an arid, limestone environment sounds specific, but can be cross referenced with other sites around the world for comparison to deduce patterns, similarities, and differences. The problem of AMD persists in a wide range of geological, climatic, and environmental settings.

1.6 Zimapán, Mexico

The town of Zimapán in Hidalgo state, Mexico is located about a 3 hour (127 mile) drive north of Mexico City (Figure 1.2).

The municipality encompasses an area of 332.4 square miles and has a population of nearly 40,000 people. The region is arid, average temperature is 19 ^{o}C with cool nights. The rainy season is May through October, although the annual average precipitation is 37 cm. The elevation is 1829 m on average. The one perennial stream is Río Tolimán that flows around Zimapán, and near the mine tailings sampled for this study (INEGI, 2010).

Zimapán, Mexico has been verified to naturally have arsenic in its groundwater, mostly from diffuse sources. Although, in total, the ground water As has been

attributed to water-rock interactions, acid mine drainage (AMD) leaching, and fumes of As penetrating soil. Currently, the region has multiple treatment plants to remove arsenic and various contaminants from drinking water distribution systems (Sracek et al., 2010; Armienta et al., 1997; Armienta and O. Cruz, 1997; Armienta et al., 2016).

Figure 1.2: Location of Zimapán, Mexico.

1.7 Geology and Hydrology of Zimapán, Mexico

A detailed description of the geological features in Zimapán was reported by Simons and Mapes V. (1956). The city is located in the far west of Hidalgo, placing it in the central plateau of Mexico. The rocks range in age from Late Jurassic to Recent. Angular unconformity separates the Cretaceous sedimentary rocks from the overlying Tertiary rocks. The Mesozoic rocks have northwestward trending folds. The fault Daxi thrust brings Lower Cretaceous limestone over tightly folded Upper

Cretaceous shale. The Tertiary rocks show minor folding, tilting, or faulting. The Malacate fault is the most important structure after Early Tertiary (Simons and Mapes V., 1956).

Mined ore is found replacing limestone, mostly chimneys, and less commonly as veins along faults in shaly limestone, fanglomerate, volcanic rocks and monzonite. Pyrometasomatic and mesothermal deposits exist, although mesothermal dominates. Ore was formed by accumulation of El Morro fanglerate and Las Espinas volcanic rock Tertiary formations. Deposits have been oxidized to depths greater than 200 meters and predominately containing plumbojarosite ($PbFe_6^{3+}(SO_4)_4(OH)_{12}$), while silver may be present in argentojarosite ($AgFe_3^{3+}(SO_4)_2(OH)_6$) (Simons and Mapes V., 1956).

1.8 Mining in Zimapán

Mining in Zimapán started the late 1500, and continues today (Simons and Mapes V., 1956; Ongley et al., 2003). The Zimapán mining district is known for its lead, zinc, and silver production. There are four major mine sites in the area: the San Francisco, Lomo de Toro, Los Balcones, and El Monte Mines. An in-depth description of mining procedures and mine design in the Zimapán mining district was published by Garcia and Querol (1991). They describe the extraction of Pb, Zn, Cu, and Ag by sublevel mining and selective surfactant flotation post-mining separation.

The most contaminated area of Zimapán is in the south part of town along the Toliman River, which holds large amounts of old mine tailings. Since the environment is arid, the As is not very mobile, but is still available for weathering and release over long periods of time (Ongley et al., 2007).

1.9 Acid Mine Drainage in the Mining District of Zimapán, Mexico

The mining regions are evident by large piles of tailings found around the state, accumulating near process plants. This research focuses on the new and aged tailings near Zimapán, Mexico, which contain high concentrations of As, Zn, Pb, Cu, Ni, Co, Sr, and pyritic-S. The weathering of mine tailings with heavy metals quickly lead to environmental issues due to their sheer size and the weathering of pyritic material to produce acid mine drainage (AMD). Oxidation of pyrite, FeS_2, produces sulfuric acid which can mobilize heavy metals once stable in solid phases (Johnson and Hallberg, 2005; Akcil and Koldas, 2006). The bedrock in Zimapán, Mexico is rich with calcium carbonate. Ideally, the carbonate minerals should be able to neutralize the acidity, but the AMD problem persists. On the southern city limits of Zimapán, alongside the Toliman River, there are heterogeneous piles of processed tailings from one of several nearby mines. This one area alone has nearly 1 million tons of tailings. A processing plant receives material from multiple surrounding mines, which contributes to the tailing's pile size and heterogeneity. These particular piles are about 60 years old, making them old enough for the geochemical reactions to produce AMD and continuously release heavy metals into the environment. Stagnant AMD on site has a pH <1 and is rich with heavy metals.

1.10 Heavy Metals in Soils in the Zimapán Area

Natural levels of As and metals in Zimapán soils are 10-100 mg/kg As, Cu, Pb, and 100 mg/kg for Zn (Ongley et al., 2003).

Soil samples in and around Zimapán average 52 mg/kg for As and mine tailings contained 14,700 mg/kg of As. Soils away from tailings and at a depth ≤ 100 cm had low or no contamination. Arsenic was found to be mostly in immobile solid phases acting as a long-term arsenic source. The immobilization is accredited to binding with

iron and manganese oxides, organic material, and carbonates in mineral fractions. A large portion of As in soils and tailings are bound to primary or secondary ore minerals, however, As may be released if pH decreases after coming in contact with leachates, processing plant water, or municipal water (Ongley et al., 2007).

Soil can contain Pb in different mineral forms such as galena (PbS), anglesite ($PbSO_4$), cerussite ($PbCO_3$), Pb oxides, Pb phosphates, Pb sulfates, or attached to clays and organic compounds. Relative bioavailability (RBA) can differ between soils with the same amount of contaminant but different mineralogy, consequently affecting their potential as hazards (Casteel et al., 2006).

Plants in the area have also been found to uptake arsenic. Two types of small trees in Zimapán have been tested. Mesquite and huizache twigs and leaves were tested for arsenic content in soils of different contamination levels. Highly contaminated soils (up to 32,000 mg/kg of As) gave twigs of mesquite 82.7 mg/kg and huizache 225 mg/kg of As. The leaves of mesquite had 78.2 mg/kg and huizache leaves had 67.0 mg/kg of As. A less contaminated soil (up to 110 mg/kg of As) gave mesquite twigs 20.8 mg/kg and leaves 27.8 mg/kg of As (Armienta et al., 2008).

1.11 Goals and Objectives

The general objectives of this study were: 1) to characterize nanoparticles and colloids from weathered tailings on the atomic scale and their transformations in a limestone environment and 2) to characterize arsenic speciation in each associated solid phase, as well as the mobilization and transformation of arsenic associated with the mineral phase conversions. Simultaneously, this would involve deducing similarities and patterns, and determining the greatest point of risk and hazards.

The specific objectives of this study are:

1. To characterize mineral and chemical species of natural As-containing phases

in:

   (a) Unoxidized and oxidized tailings.

   (b) River sediments near the tailings.

2. To identify the As and Fe speciation and geochemical processes affected by the carbonate-rich environment.

   (a) Arsenic speciation.

   (b) Identify arsenic containing mineral phases.

The merits of this research aim to expand the understandings of a specific location that incorporates a unique set of traits. This research can advance methodologies used in future experiments and provide an increasingly detailed characterization of the area for improved modeling predictions. Building a strong database for computer modeling better enables a program to predict how to manage a geochemical system that is currently unpredictable.

2. ACID MINE DRAINAGE IN ZIMAPÁN, MEXICO: A CASE STUDY

2.1 Introduction

The Zimapán mining district in the Mexican state of Hidalgo has seen constant mining since the end of the 1500's (Ongley et al., 2003). The mining regions are evident by large piles of tailings found around the state, accumulating near process plants. The tailings near Zimapán, Mexico, contain high concentrations of arsenic, zinc, lead, copper, nickel, cobalt, strontium, and pyritic sulfur. The weathering of mine tailings with heavy metals quickly lead to environmental issues due to their sheer size and the weathering of pyritic material to produce acid mine drainage (AMD). Oxidation of pyrite, FeS_2, produces sulfuric acid which alters a mineral's stability. This process releases and mobilizes the heavy metals that were once stable in solid phases. A common method to neutralize and control acid mine drainage is adding a calcium carbonate variant, or lime (Johnson and Hallberg, 2005; Akcil and Koldas, 2006). It has also been suggested that some Zimapán tailing sites should utilize a carbonate variant to raise the pH to stabilize Fe- and Al-oxides and therefore reduce further leaching of arsenic species (Meendez and Armienta, 2003)

The soil types in the region are regosois and lithosis, similar to Entisols in the USDA taxonomy. On the southern city limits of Zimapán, alongside the Toliman River, there are heterogeneous piles of processed tailings from several nearby mines. This one area alone has nearly 1 million tons of tailings. A processing plant receives material from multiple surrounding mines which contributes to the tailing's pile size and heterogeneity. These particular piles are about 60 years old, which is enough time for the geochemical reactions to produce AMD and continuously release heavy metals into the environment. Stagnant AMD on site has a pH <1 and rich with

heavy metals. The color of stagnant AMD can be a dark red color (Figure 2.1).

Figure 2.1: Pooling of AMD with a deep red hue. This was formed in a low spot near the processing plant used for all the tailings in this study.

Over time, the dissolution and re-precipitation of solid phases during the oxidation and neutralization were directly related to the transformation and translocation of the heavy metals. Colloids are more susceptible to environmental changes and therefore, regulate the chemistry of toxic arsenic and heavy metals in surface water and ground water. Unfortunately, knowledge on these reactive nanoparticles and colloids in the limestone environment and in liming reclamation areas is limited due to the difficulties of characterization with common methods and instruments. The detailed characterization of AMD aids in the development of better waste management practices, risk assessment, and selecting the best remediation methods for contaminated soils.

The mine tailings in Zimapán were away from urban neighborhoods but have multiple suburban neighboring inhabitants. For safety, the potential for human interaction is not eliminated and modes of contaminant transport to higher populated areas is possible. The tailing piles are void of any vegetation, making them susceptible to weathering conditions. Arsenic in the Toliman River sediment was earlier determined to mainly be from wind blown particulate matter (Espinosa et al., 2009).

The mine tailings, streams, and receiving bodies of water around Zimapán offer an excellent site to systematically investigate the geochemical process during the oxidation, transport, and sedimentation of the heavy metals. A variety of information of mineralogy and geochemistry on mine tailing, soils, surface and ground water have been reported by Armienta's group in the last two decades (Armienta and O. Cruz, 1997; Armienta et al., 2001; Ongley et al., 2001; Armienta et al., 2003; Ongley et al., 2003; Romero et al., 2004; Armienta et al., 2007; Ongley et al., 2007; Romero et al., 2007; Armienta and Segovia, 2008; Romero et al., 2008; Armienta et al., 2012). Preliminary investigations on the oxidized tailings have shown complex mineralogy in the weathered tailings and extreme spatial heterogeneity of the materials. High levels of arsenic and heavy metals have been detected in surface water and groundwater far away from the tailings. The Preisser Mine and San Miguel Viejo Mine, South of Zimapán, contain a depot of mine waste with a quantity estimated around a million tonnes of mine tailings, new and old. The oldest tailings are estimated to be 60 years old. The fresh and aged oxidized tailings have shown to effect the transport of contaminants (Armienta et al., 2016).

The objectives of this study were to 1) characterize mineralogical species of natural arsenic-containing phases 2) identify nanoparticles and colloids from tailings and 3) identify and deduce patterns of AMD mineralogy in a limestone environment.

In addition, this project aims to determine the distribution of contaminants,

assess the potential sources of arsenic, evaluate potential to mobilize arsenic and other metals, assess geologic sources of heavy metals and assess similarities of other mines in arid limestone environments.

2.2 Materials and Methods

2.2.1 Tailing Sample Collection

There were several consecutive piles of tailings along the Toliman River. Due to historical and current ore processing at this particular site, the samples collected were categorized by their age and mineralogy, respectively. There were old and highly weathered piles of tailings that showed red, yellow, or brown strata through oxidized mineralogy and seeping AMD, and the opposite, there were more current tailing samples that were processed in the past few years, showing fresh gray color. The majority of samples were tailings, but there were also three river sediments collected (Figures 2.3, 2.2, and Table 2.1).

Four categories of samples were collected in the study. 1) Tailings with minimal oxidation used for pond retention barriers and the top of piles that had fresh tailings recently deposited from the processing plant; 2) Soluble sulfates that have precipitated from the tailings and exhibited bright contrasting white, green, yellow colors; 3) Oxidized low-soluble oxides and arsenate from the tailings, and 4) River sediments from the Toliman River near the tailings and additional sediment from a different river a few miles north of the tailings. The Toliman River sediment samples were taken when the river was about 0.6 meters deep with steadily flowing water.

Samples were encoded by their location and characteristics observed in the field. One example is Zim-PR-1-Top-1:

$$\overbrace{Zim}^{\text{Zimapan}} - \overbrace{PR}^{\text{Tailing Pile}} - \overbrace{1}^{\text{Pile Number}} - \overbrace{Top}^{\text{Sample Name}} - \overbrace{1}^{\text{Sample Number}}$$

Some of the samples were collected in the same area, only a few centimeters away. When samples were taken this close to each other, there was a clear transitional difference in color, solubility, or texture. The sample description and GPS location coordinates can be found in Tables 2.2 and 2.3. The GPS coordinates were taken immediately after bagging samples into Ziplock bags.

Sample	Location	Sample	Location
Fresh Unoxidized Tailings		Oxidized Tailings	
Zim-PR-2-Fresh-1	e	Zim-SMV-1	g
Zim-SMV-2	i	Zim-PR-1-Smiddle-1	b
		Zim-PR-1-Smiddle-2	b
Soluble Sulfates		Zim-PR-1-Smiddle-3	b
Zim-1-Nside-1	d	Zim-PR-1-Top-1	c
Zim-1-Nside-3	d	Zim-PR-2-Red-2	f
Zim-1-Nside-4	d	Zim-PR-2-Yellow-2	f
Zim-SMV-4	h	Zim-PR-2-Gray-2	f
		River Sediment	
		Zim-PR-1-River-1	a
		Zim-SMV-3 (River)	j
		Zim-River-3 (far)	k

Table 2.1: Most of the locations of the samples collected are shown above. Sampling included a variety of mine tailing sites and river sediments from different proximities from the tailings (Figure 2.3).

Figure 2.2: The three samples taken of river sediment were collected here. k = Zim-River-3, 2 = Zim-SMV-3 (San Miguel Viejo Mine), and 1 = Zim-PR-1-River-1 (Preisser Mine).

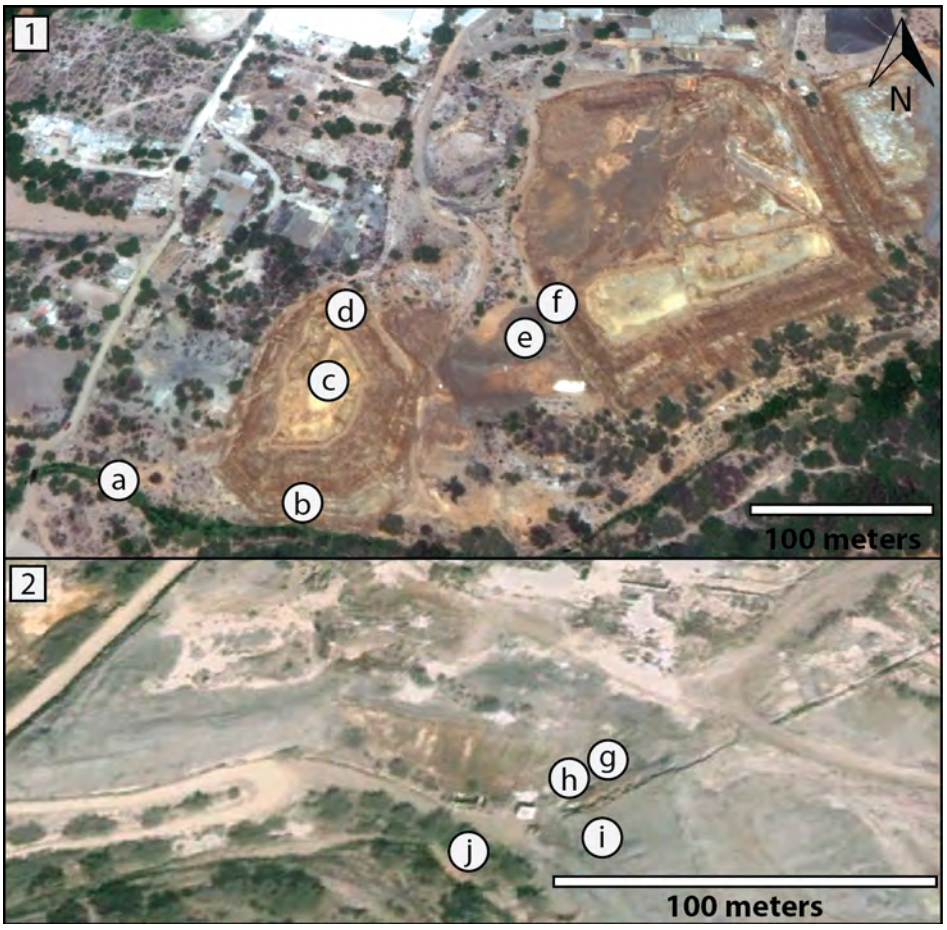

Figure 2.3: Sample locations at the Preisser Mine(1) and the San Miguel Viejo Mine(2).

			GPS Coordinates		Elevation
Sample ID	Mine	Munsell	Latitude	Longitude	Meters
Fresh Unoxidized Tailings					
Zim-PR-2-Fresh-1	Preisser	7.5YR 1/2	N 20° 43′ 35.4”	W 99° 23′ 5.5”	1700
Zim-SMV-2	San Miguel Viejo	N4	N 20° 43′ 37.6”	W 99° 23′ 49.4”	1685
Soluble Sulfates					
Zim-1-Nside-1	Preisser	7.5GY 4/8	N 20° 43′ 36.2”	W 99° 23′ 9.1”	1702
Zim-1-Nside-2	”	”	”		”
Zim-1-Nside-3	”	2.5YR 4/10	”		”
Zim-1-Nside-4	”	N9	”		”
SMV-4	San Miguel Viejo	N9	N 20° 43′ 37.9”	W 99° 23′ 49.7”	1687

Table 2.2: Samples collected at Zimapán, Mexico, and their location coordinates.

			GPS Coordinates		Elevation
Sample ID	Mine	Munsell	Latitude	Longitude	Meters
Oxidized Tailings					
Zim-PR-2-Gray-2	Preisser	N4	N 20° 43′ 35.6”	W 99° 23′ 5.1”	1702
Zim-PR-2-Red-2	”	10R 2/8	N 20° 43′ 35.6”	W 99° 23′ 5.1”	1702
Zim-PR-1-Top-1	”	”	N 20° 43′ 34.8”	W 99° 23′ 9.2”	1697
Zim-PR-1-Smiddle-1	”	”	N 20° 43′ 32.7”	W 99° 23′ 9.6”	1693
Zim-PR-1-Smiddle-2	”	N4	”		”
Zim-PR-1-Smiddle-3	”	10YR 7/10	”		”
Zim-PR-2-Yellow-2	”	2.5Y 8/10	N 20° 43′ 35.6”	W 99° 23′ 5.1”	1702
Zim-SMV-1	San Miguel Viejo	10R 2/8	N 20° 43′ 38”	W 99° 23′ 49.2”	1685
River Sediment					
Zim-PR-1-River-1	Preisser	7.5YR 4/8	N 20° 43′ 33.3”	W 99° 23′ 13.0”	1688
Zim-SMV-3	San Miguel Viejo	”	N 20° 43′ 37.1”	W 99° 23′ 50.3”	1681
Zim-River-3		”	N 20° 46′ 40.3”	W 99° 25′ 45.6”	1685

Table 2.3: Additional samples collected at Zimapán, Mexico, and their location coordinates.

2.2.2 Treatments and Analysis of Samples

Size fractionation was performed on most samples, except the soluble sulfates. Carbonate minerals in the fresh tailings (Zim-PR-2-Fresh-1) and river sediment (Zim-SMV-3) were removed by pH 5 sodium acetate. The samples were dispersed in a dilute pH 10 Na_2CO_3 solution and passed through a #270 sieve to sperate the sand fraction from the silt and clay fractions. The samples were fractionated into sand (> 50 μm), silt (2 - 50 μm), and clay (< 2 μm) fractions (Guggenheim and Martin, 1995). Automated separation of silt and clay fractions were accomplished by using a custom-built size fractionator described by Deng and Arvide (2011). The fractionator was then automated with an Arduino microcontroller. Methods for size fractionation can be found in the Texas A&M University Soil Mineralogy lab manual (Deng et al., 2012). The pH was determined by using a bulk sample to water ratio of 1:5.

The mineral composition of the bulk sample and the sand, silt, clay fractions of each sample were analyzed on a Bruker D8 Advance x-ray diffractometer (XRD) using Cu Kα radiation, 35 kV, 45 mA, 3 seconds dwell time at each step, 0.05^o step size, and Sol-X energy-dispersive detector. The XRD operated with the same instrumental parameters for the bulk, sand, silt fractions and were scanned from 2^o to 70^o 2θ. The clay fractions were scanned from 2^o to 32^o 2θ. The powder samples were mounted on deep plastic sample holder. The clay fraction suspensions were dried as thin films on glass or quartz slides.

The clay fraction of most samples underwent treatments to assist XRD data interpretation. Once obtained, a portion of the clay fractions were separately saturated with Mg^{2+} (0.5M $MgCl_2$) and K^+ (1M KCl) solutions. After three washes of solution and one of DI water, a few drops were dried onto XRD slides for analysis. After analysis, the Mg^{2+} saturated clay slide is coated with glycerol with an aerosol

spray-can applicator, then air dried. In addition, the K^+ saturated slide was heated to 330 ^{o}C and 550 ^{o}C one hour, cooled to room temperature, and then scanned on the XRD (Deng et al., 2012).

The chemical composition of selected samples was determined at the Mineral Lab (Golden, Colorado, USA) using x-ray fluorescence (XRF). The XRF spectrometer consists of a Phillips simultaneous, wavelength dispersive unit equipped with 26 fixed detectors, 2 scanning detectors, and a Rh end-window tube (www.theminerallab.com).

Transmission electron microscopy (TEM) analysis was performed on a FEI TECNAI G2 F20 ST FE-TEM. Scanning electron microscopy (SEM) FEI QUANTA 600 FE-SEM. The TEM and SEM analyses were conducted at the Texas A&M University Microscopy and Imaging Center.

Fourier transform infrared (FTIR) analysis was conducted on a PerkinElmer Spectrum 100. FTIR patterns were recorded using an attenuated total reflectance (ATR) accessory with a total of 32 scans for each sample and a resolution of 2 cm^{-1}.

2.3 Results

Samples were categorized based on their mineralogy, color, and sampling location (Table 2.4). Categorization is helpful to see trends in chemical and physical characteristics. Table 2.4 shows the general mineralogy for all the samples collected.

Sample ID	pH	Color	Mineral Phases
Fresh Unoxidized Tailings			
Zim-PR-2-Fresh-1	7.2	Black	Quartz, gypsum, pyrite, sphalerite, calcite, pyrrhotite
Zim-SMV-2	2.4	Gray	Quartz, gypsum, calcite
Soluble Sulfates			
Zim-1-Nside-1	2.9	Green	Quartz, gypsum, melanterite
Zim-1-Nside-3	2.9	Orange	Quartz, gypsum, boyleite, rozenite
Zim-1-Nside-4	3.5	White	Quartz, gypsum, boyleite, rozenite
Zim-SMV-4	5.3	White	Gypsum, pyrite, boyleite, rozenite
Oxidized Tailings			
Zim-SMV-1	5.0	Red	Quartz, gypsum
Zim-PR-1-Smiddle-1	4.8	Red	Quartz, gypsum, goethite, pyrite
Zim-PR-1-Smiddle-2	7.0	Gray	Quartz, gypsum, pyrite, scorodite
Zim-PR-1-Smiddle-3	2.2	Yellow	Gypsum, copiapite
Zim-PR-2-Yellow-2	2.4	Yellow	Quartz, gypsum, jarosite, sanidine
Zim-PR-2-Red-2	2.7	Red	Quartz, gypsum, jarosite, mica
Zim-PR-2-Gray-2	2.4	Gray	Quartz, gypsum, jarosite, scorodite, pyrite, wollastonite
Zim-PR-1-Top-1	3.0	Red	Quartz, gypsum, jarosite, goethite, smectite, chlorite, biotite, hornblende, vermiculite
River Sediment			
Zim-PR-1-River-1	7.1	Tan	Quartz, jarosite, calcite, pryite, anorthite, alunite, ilmenite, smectite, kaolinite, biotite, muscovite
Zim-SMV-3 (River)	7.6	Tan	Quartz, calcite, alunite, ilmenite, hornblende, montmorillonite, augite kaolinite, anorthite, muscovite
Zim-River-3 (far)	8.0	Tan	Quartz, calcite, alunite, ilmenite, muscovite, chlorite, anorthite, kaolinite, montmorillonite

Table 2.4: Major minerals and pH identified in mine tailings and river sediment.

2.3.1 Major Elemental Compositions of Tailing Samples

The XRF analysis (Tables 2.5 and 2.6) suggested that the sample with the highest amount of arsenic was Zim-PR-2-Gray-2 with 110,000 mg/kg. The sample with the least amount of arsenic was sample Zim-River-3 with <50 mg/kg, an extremely low concentration in comparison to the other two river samples that contained 2,000 mg/kg and 15,000 mg/kg of arsenic in samples Zim-SMV-3 and Zim-PR-River-1, respectively. The river sediment, Zim-SMV-3, almost exclusively contained the lowest level of heavy metals. The Zim-PR-2-Yellow-2 sample had the highest levels of lead with 18,000 mg/kg. The samples Zim-PR-2-Red-2 and Zim-PR-2-Fresh-1 had the highest amount of Zn with 26,000 mg/kg and the latter, 23,000 mg/kg. The fresh tailings of sample Zim-PR-2-Fresh-1 had 25,000 mg/kg of As, 23,000 mg/kg of Zn, 10,000 mg/kg of Pb. The tailings had 13.0 weight percent of sulfur. The Pb favored oxidized samples which contained oxides that it could absorb to or incorporate in to. Lead was below 670 mg/kg in all soluble sulfate samples collected. Lead and As showed less mobility than Cu and Zn.

All the samples had less than 200 mg/kg Sr, except for the river samples which had 360 to 576 mg/kg Sr. This was lower than over metals, but high for this trace element. This concentration can be contributed to the region's low annual rain fall and high evaporation rate (Skougstad and Horr, 1963). There was 7,345 mg/kg Co found in sample Zim-PR-1-Smiddle-3, although, no other sample showed more than 329 mg/kg Co.

The categories of unoxidized tailings, soluble sulfates, oxidized tailings, and river sediments had some elemental differences and similarities too. The greatest amount of As was in the oxidized samples, even the lowest amount (5,193 mg/kg As) was greater than the highest concentration of the soluble sulfates and river sediments.

This suggested As retention or precipitation on the oxidized phases due to iron oxide affiliation. The lowest amount of As was in the river sediment, which also had the lowest amount of Fe content. All the samples had a considerable amount of Fe, except for the river sediments and one soluble sulfate (SMV-4). Sulfur was in the relatively fresh, primary, and secondary mineral phases in almost all categories, except for the river sediment. Sulfur can play many roles as sulfides and sulfates once liberated from the sulfur-rich pyritic material. The highest amount of Al present was found in the river sediments, highest being 9.79% Al. Sample Zim-PR-2-Fresh-1 had a significant amount, 2.3% Al, but all the other oxidized and soluble sulfate samples had $< 1\%$ Al. Samples that had minimal oxidation had the highest amount of Al. Samples that were oxidized produced acidic conditions that can make Al more soluble. The majority of samples had a range from 1.08 - 22.6% Ca. Similarly, K and Na were found in low concentrations, but the highest concentrations were in the river sediments, up to 2.01% K and 1.0% Na, correlating with the additional silicate minerals present. The highest amounts of P were found in the soluble sulfates, up to 6.66% P, and half the samples in the oxidized category showed a significant amount of P (where other half was $< 0.1\%$ P). Low pH conditions, as in the oxidized samples, would readily dissolve apatite species and release P. The lack of P minerals suggests that P persisted as amorphous species. All the samples throughout were low with Cl and Ti. The anion Cl^- forms very soluble components which could lead its minimum discovery. The metal Ti^{4+} can be stable but naturally occurring at low concentrations when an elemental component. The metals Pb, Cu, and As concentrated in the oxidized phases due to incorporation with secondary sulfates, while the unoxidized samples had similar but generally less quantities. The unoxidized samples showed to have high levels of Zn and As, although less than the oxidized samples, overall. All the soluble sulfates had very high amounts of Zn, in addition to significant amounts of

As, and Cu. The river sediments near tailings had high amounts of Zn, As, and lesser so Pb and Cu, which were all greatly diminished in the river sediment collected far from tailings piles.

	% (wt)												
Sample ID	Na_2O	MgO	Al_2O_3	SiO_2	P_2O_5	S	Cl	K_2O	CaO	TiO_2	MnO_2	Fe_2O_3	BaO
Fresh Unoxidized Tailings													
Zim-PR-2-Fresh-1	0.30	1.30	2.30	19.00	<0.10	13.0	<0.10	0.90	14.0	0.1	0.20	27.0	<0.10
Zim-SMV-2		-	0.25	1.29	1.56	5.66	0.07	1.25	13.95	0.07	0.21	15.8	0.02
Soluble Sulfates													
Zim-1-Nside-1		0.99	0.28	0.44	2.58	6.4	0.07	0.07	0.09	-	0.05	28.5	-
Zim-1-Nside-3		1.70	0.27	0.48	3.39	8.1	0.06	0.07	0.20	-	0.18	27.1	-
Zim-1-Nside-4		1.19	0.25	0.46	3.50	7.9	0.31	0.09	0.34	-	0.40	22.1	-
SMV-4		1.12	0.17	0.71	6.66	17.7	0.41	0.36	3.52	0.03	1.32	3.4	0.05
Oxidized Tailings													
Zim-PR-2-Yellow-2	<0.10	0.20	2.30	20.0	0.10	10.0	<0.10	4.80	3.30	0.3	<0.10	26.0	0.20
Zim-PR-2-Red-2	<0.10	0.40	1.10	9.20	<0.10	14.0	<0.10	0.80	16.00	<0.1	0.10	28.0	<0.10
Zim-PR-2-Gray-2	<0.10	1.30	0.20	6.60	0.10	16.0	<0.10	0.20	8.60	<0.1	<0.10	28.0	<0.10
Zim-PR-1-Top-1	<0.05	3.55	3.10	20.60	0.17	9.0	<0.02	1.73	15.80	0.20	0.14	18.9	0.020
Zim-SMV-1		1.30	0.25	0.75	2.23	5.3	-	0.27	4.82	0.06	0.04	29.9	0.010
Zim-PR-1-Smiddle-1		-	0.23	0.59	1.57	7.9	0.10	0.07	6.87	-	0.11	27.3	-
Zim-PR-1-Smiddle-2		-	0.24	1.00	2.34	20.1	0.10	0.05	3.36	0.04	-	36.7	0.02
Zim-PR-1-Smiddle-3		2.55	0.34	0.53	-	3.0	0.45	0.08	1.08	-	0.05	15.2	-
River Sediment													
Zim-PR-1-River-1	0.89	1.55	7.73	38.4	0.36	3.2	<0.02	1.22	14.7	0.72	0.14	13.8	0.07
Zim-SMV-3	0.89	1.79	9.25	44.5	1.08	0.4	<0.02	1.60	11.4	0.72	0.13	11.7	0.08
Zim-River-3	1.00	2.68	9.79	37.9	0.18	0.1	<0.02	2.01	22.6	0.65	0.09	5.5	0.06

Table 2.5: XRF results in weight percent for samples from Zimapán, Mexico. - = below detection limits.

	mg/kg											
Sample ID	Cr	Co	Ni	Cu	Zn	As	Sn	Pb	Sr	Zr	Rb	Y
Fresh Unoxidized Tailings												
Zim-PR-2-Fresh-1	<100	<100	<100	593	23,000	25,000	<500	4,930	<200	<100	<50	<100
Zim-SMV-2	118	-	81	1,421	21,330	28,131	119	2,872	118	73	120	16
Soluble Sulfates												
Zim-1-Nside-1	100	-	-	5,173	30,878	1,569	-	21	-	-	-	4
Zim-1-Nside-3	105	-	-	1,224	58,690	4,407	-	157	-	-	6	22
Zim-1-Nside-4	137	-	63	367	99,982	1,509	-	464	1	-	9	44
SMV-4	202	329	731	6,854	465,104	4,544	59	670	52	-	13	47
Oxidized Tailings												
Zim-PR-2-Yellow-2	<100	<100	<100	334	8,950	7,830	<500	18,000	<200	<100	151	<100
Zim-PR-2-Red-2	<100	<100	<100	830	26,000	26,000	<500	5,820	<200	<100	<100	<100
Zim-PR-2-Gray-2	<100	<100	<100	530	10,000	110,000	<500	10,000	<200	<100	<50	<100
Zim-PR-1-Top-1	<50	<50	<50	665	3,450	6,040	219	7,470	94	56	122	<50
Zim-SMV-1	136	-	-	778	5,193	62,258	99	2,043	52	22	57	10
Zim-PR-1-Smiddle-1	118	-	-	1,596	42,720	11,894	62	5,338	41	-	25	13
Zim-PR-1-Smiddle-2	50	-	-	241	1,285	5,528	94	7,278	28	-	21	-
Zim-PR-1-Smiddle-3	-	7,345	24	926	10,254	6,377	48	62	140	189	6	87
River Sediment												
Zim-PR-1-River-1	83	<50	<50	396	2,900	3,380	158	1,690	333	123	<50	<50
Zim-SMV-3	66	<50	<50	525	4,880	2,020	155	892	360	152	57	<50
Zim-River-3	81	<50	<50	<50	614	<50	58	327	576	131	72	<50

Table 2.6: XRF results in mg/kg for samples from Zimapán, Mexico

2.3.2 Minerals in Oxidized Tailings

Large amounts of gypsum ($CaSO_4 \cdot 2\,H_2O$) were observed in most samples due to the low pH of runoff in this limestone environment. The mineralogical identification showed predominantly jarosite ($KFe(SO_4)(OH)_6$) and scorodite ($FeAsO_4 \cdot 2\,H_2O$) present in multiple samples.

The oldest tailings collected at sampling locations were 60 years old. These tailings have been aged long enough to oxidize and contain secondary minerals such as copiapite ($FeFe_4(SO_4)_6(OH)_2 \cdot 20\,H_2O$), gypsum ($CaSO_4 \cdot 2\,H_2O$), and jarosite ($KFe(SO_4)(OH)_6$) as identified by XRD (Figure 2.5), but still retain unoxidized iron sulfides such as pyrite (FeS_2) and sphalerite (ZnS). The pH of all the samples collected were lowest in this category. The average tailing pH is about 2.5, but the runoff can be more acidic with a pH lower than 1 (Table 2.4).

2.3.2.1 Yellow Oxidized Samples

The two oxidized tailings, Zim-PR-1-Smiddle-3 and Zim-PR-2-Yellow-2 (Figure 2.4), shared a similar yellow appearance but had different mineralogy. The samples Zim-PR-2-Yellow-2 is dominated by jarosite ($KFe(SO_4)(OH)_6$), where Zim-PR-1-Smiddle-3 is dominated by copiapite ($Fe^{2+}{Fe_4}^{3+}(SO_4)_6(OH)_2 \cdot 20\,H_2O$). Both samples contained jarosite, gypsum, and pyrite. Sample Zim-PR-1-Smiddle-3 had large amounts of copiapite, and lesser amounts of gypsum and quartz (SiO_2). The XRD analysis suggested that the jarosite is the only mineral identified in the silt and clay fractions (Figures 2.5 and 2.6) of sample Zim-PR-2-Yellow. Whereas, the feldspar sanidine ($K(AlSi_3O_8)$) is concentrated in the sand fraction in this sample.

Figure 2.4: This is the East pile of tailings at the Preisser Mine. There were three samples collected here: (a)Zim-PR-2-Red-2, (b)Zim-PR-2-Yellow-2, and (c)Zim-PR-2-Gray-2.

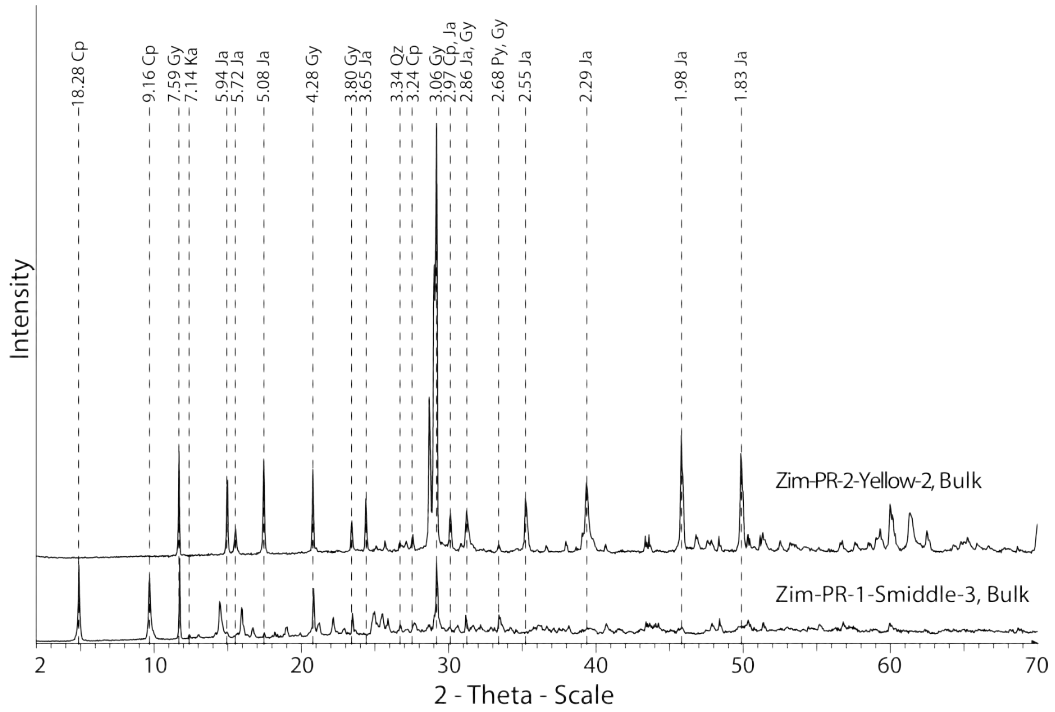

Figure 2.5: Two samples similar by their yellow color and also contain jarosite. Ja = Jarosite, Cp = Copiapite, Py = Pyrite, Ka = Kaolinite, Gy = Gypsum, Qz = Quartz.

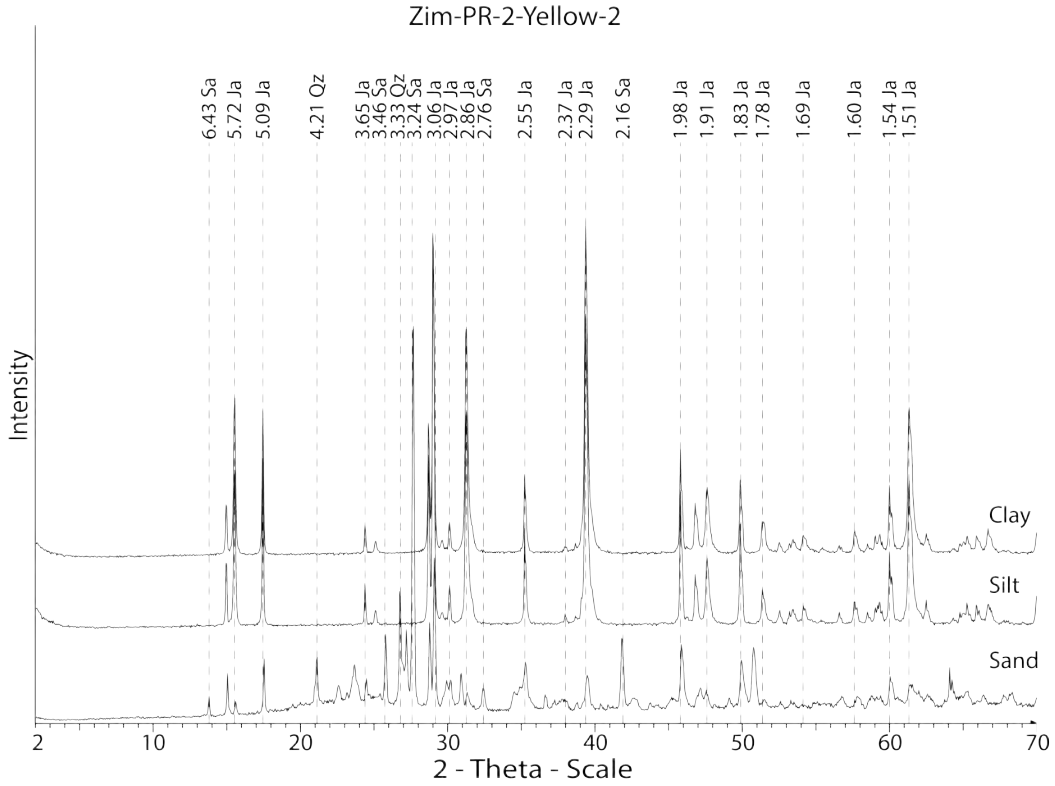

Figure 2.6: XRD patterns of the sand, silt, and clay fractions of Zim-PR-2-Yellow-2. Ja = Jarosite, Sa = Sanidine.

The EDS analysis suggested that jarosite ($KFe(SO_4)(OH)_6$) in the Zim-PR-2-Yellow-2 contained minor amounts of lead, and possibly As (Figure 2.7). The EDS also suggested the K:S ratio is lower than the 1:1 ratio of an ideal jarosite.

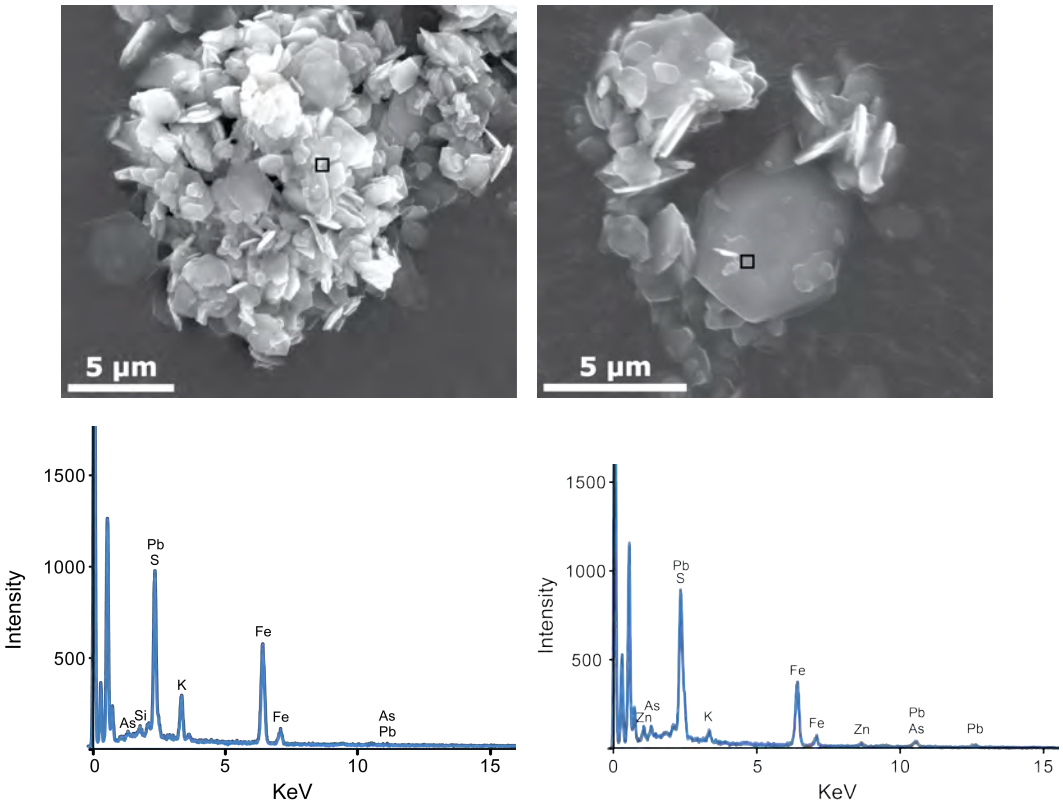

Figure 2.7: Two aggregates of jarosite and their EDS spectra from the sample Zim-PR-2-Yellow-2, silt size fraction. There is a low indication of Pb and as the signal for K decreases, Pb increases, although disproportionately.

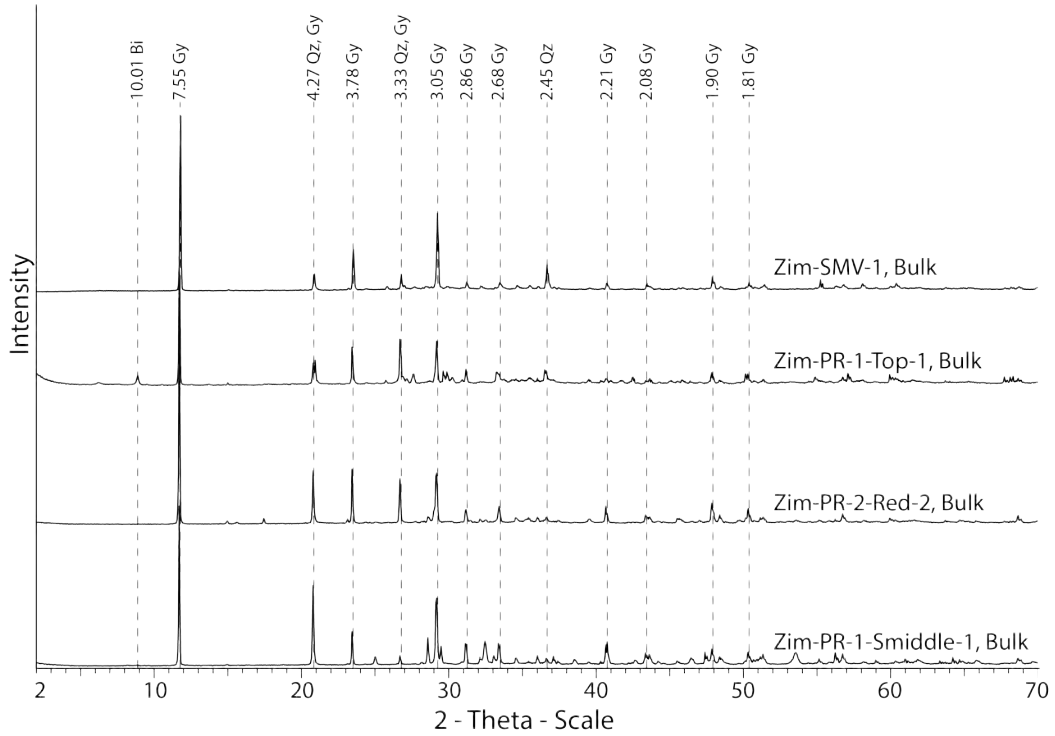

Figure 2.8: Four untreated bulk samples that all share the same shade of red. Bi = Biotite, Gy = Gypsum, Qz = Quartz.

2.3.2.2 Red Oxidized Samples

There were four red, oxidized samples: Zim-PR-1-Top-1 (Figure 2.9), Zim-Smiddle-1, Zim-PR-2-Red-2 (Figure 2.4), and Zim-SMV-1. The XRD patterns of the bulk samples suggest they were cemented by gypsum (Figure 2.8). The XRD patterns of different fractions of Zim-PR-2-Red-2 (Figure 2.10), Zim-PR-1-Top-1 (Figures 2.11 and 2.14), and Zim-PR-1-Smiddle-1 (Figure 2.12) indicated that the samples contained jarosite ($KFe(SO_4)(OH)_6$), pyrite ($Fe^{2+}S_2$), gypsum ($CaSO_4 \cdot 2\,H_2O$), quartz (SiO_2), sphalerite ($(Zn,Fe^{2+})S$), augite ($(Na,Ca)(Mg,Fe^{2+},Al,Fe^{3+},Ti)[(Si,Al)_2O_6]$), micas (biotite $K(Mg,Fe^{2+})_3(AlSi_3O_{10})(OH)_2$), chlorite ($(Mg,Fe)_3(Si,Al)_4O_{10}[(OH)_2 \cdot (Mg,Fe)_3(OH)_6]$), hornblende

$(Ca_2[(Fe^{2+},Mg)_4Al](Si_7Al)O_{22}(OH)_2)$, and goethite (FeO(OH)). The iron oxide goethite XRD peaks are broad, indicating low crystallinity of the iron oxides in the samples.

The clay fraction of Zim-PR-1-Top-1 contained vermiculite, smectite, mica (biotite and muscovite) (Figure 2.14).

Figure 2.9: This is on the top of the Preisser Mine tailings, where sample (a)Zim-PR-1-Top-1 was collected.

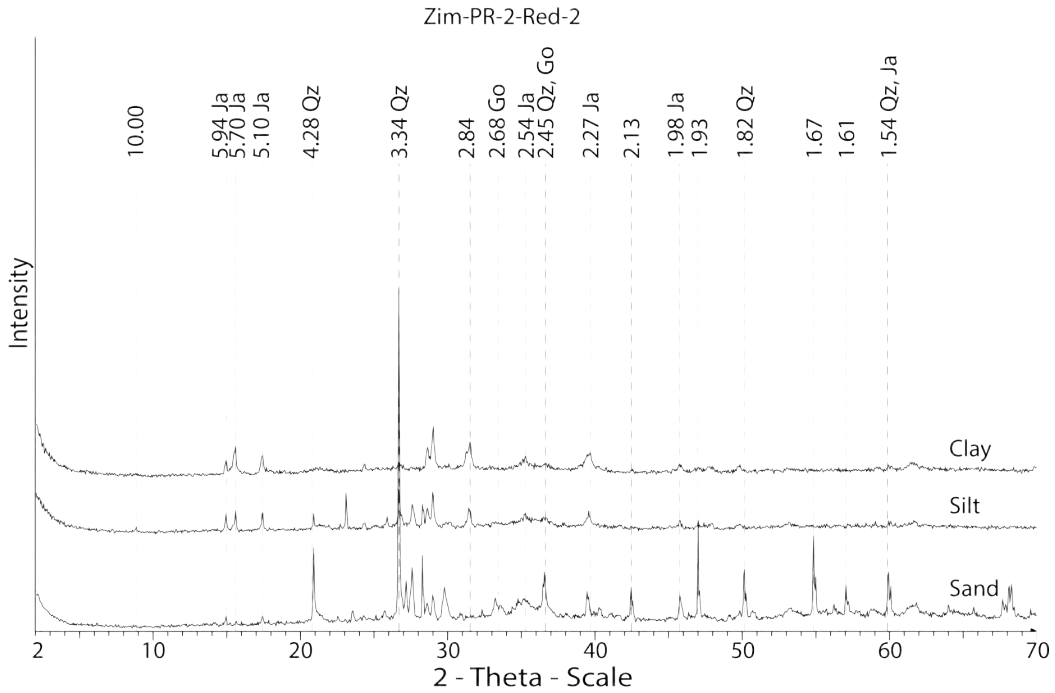

Figure 2.10: XRD patterns of the silt, sand, and clay factions for sample Zim-PR-2-Red-2. Ja = Jarosite, Go = Goethite Qz = Quartz.

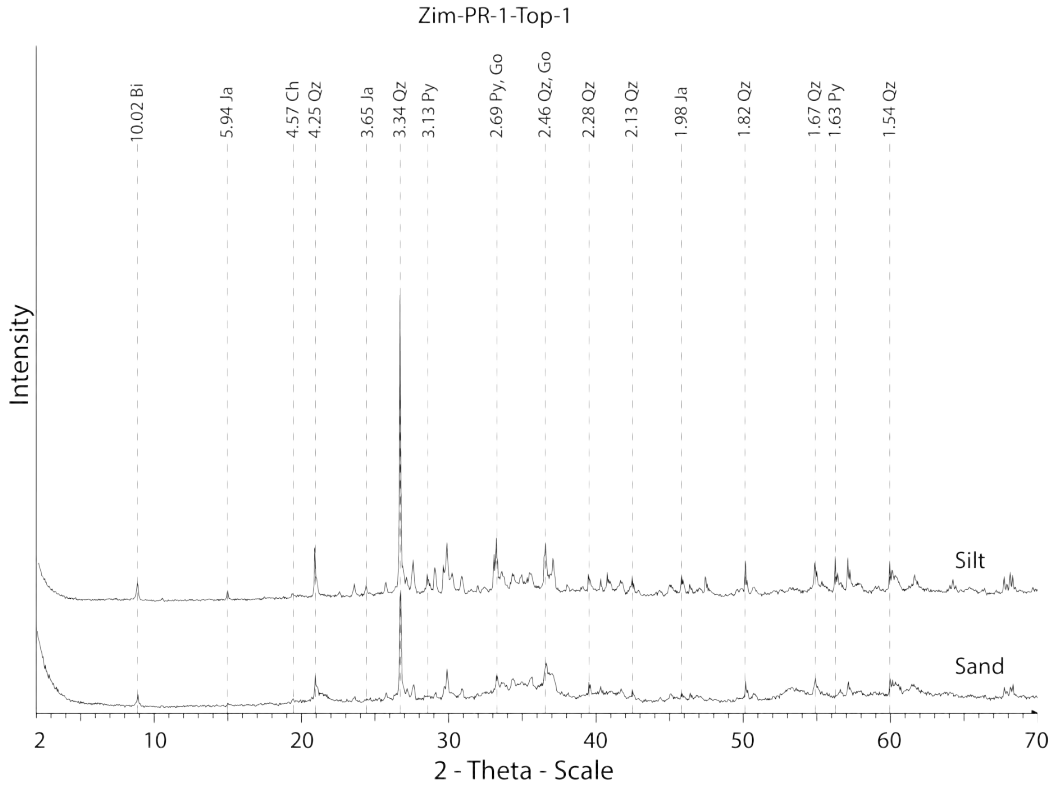

Figure 2.11: XRD patterns of the silt, sand, and clay factions for sample Zim-PR-1-Top-1. Ch = Chlorite, Ja = Jarosite, Py = Pyrite, Bi = Biotite, Go = Goethite, Qz = Quartz.

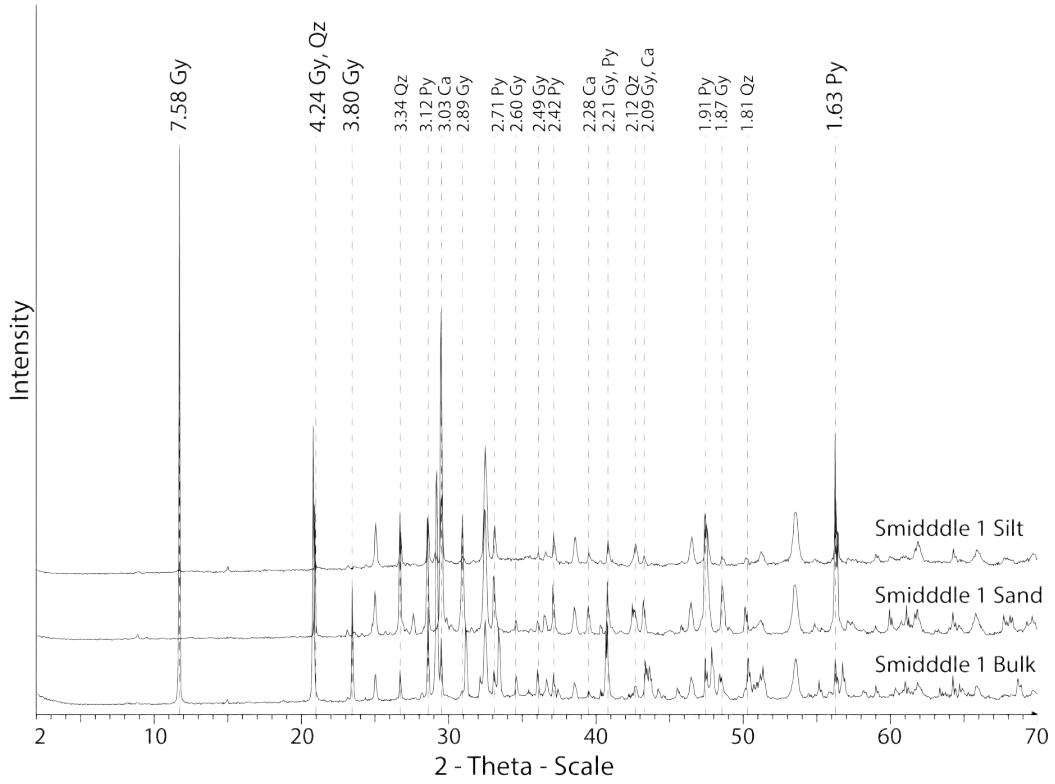

Figure 2.12: XRD patterns of the silt, sand, and clay factions for sample Zim-PR-1-Smiddle-1. Py = Pyrite, Gy = Gypsum, Ca = Calcite, Qz = Quartz.

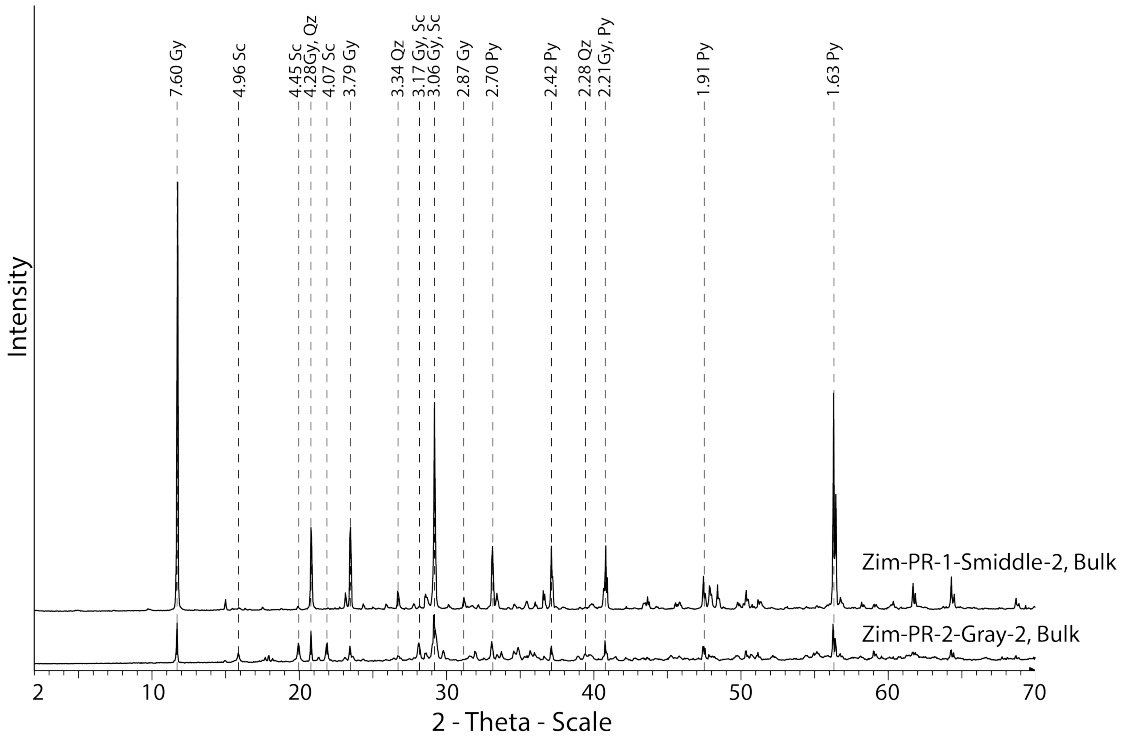

Figure 2.13: Three untreated bulk samples that all similar by their color gray. Sc = Scorodite, Py = Pyrite, Gy = Gypsum, Qz = Quartz.

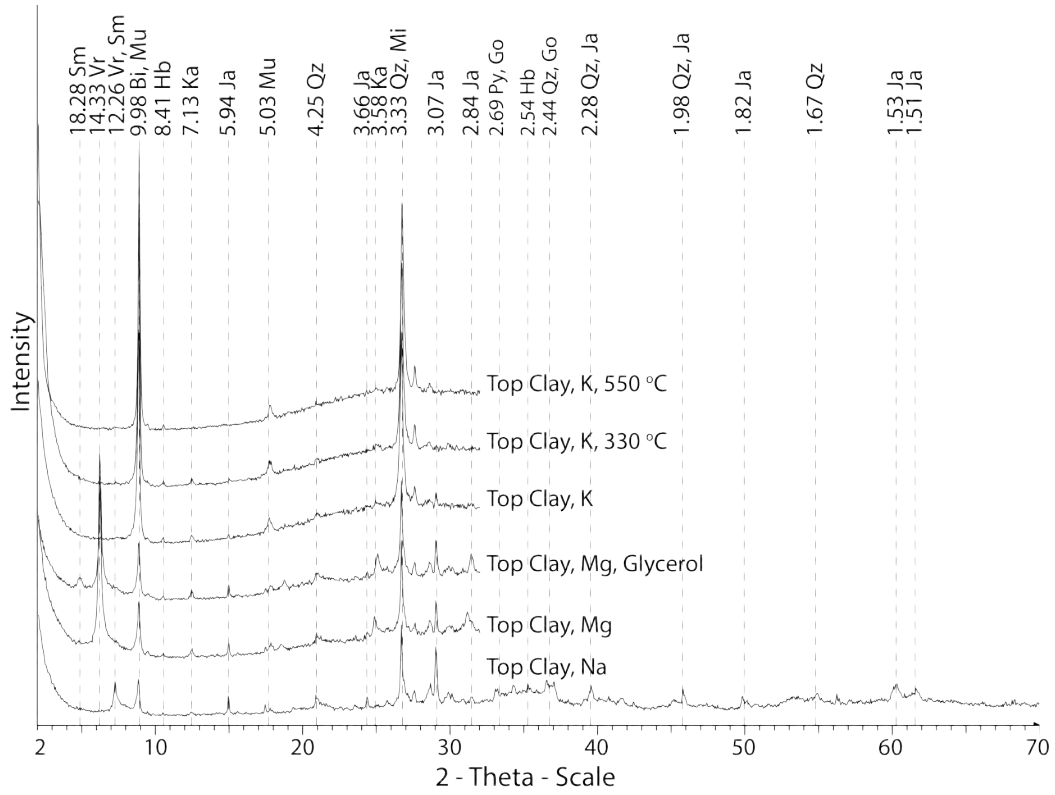

Figure 2.14: XRD patterns for sample Zim-PR-1-Top-1 clay size fraction treated by heat, cation saturation, and/or glycerol. Sm = Smectite, Vr = Vermiculite, Ja = Jarosite, Py = Pyrite, Hb = Hornblende, Mi = Micas, Mu = Muscovite, Bi = Biotite, Qz = Quartz.

SEM analysis of Zim-PR-1-Top-1 observed arsenopyrite. The EDS spectra indicated incorporation of Cu, As, and Pb in the sulfide minerals(Figure 2.15).

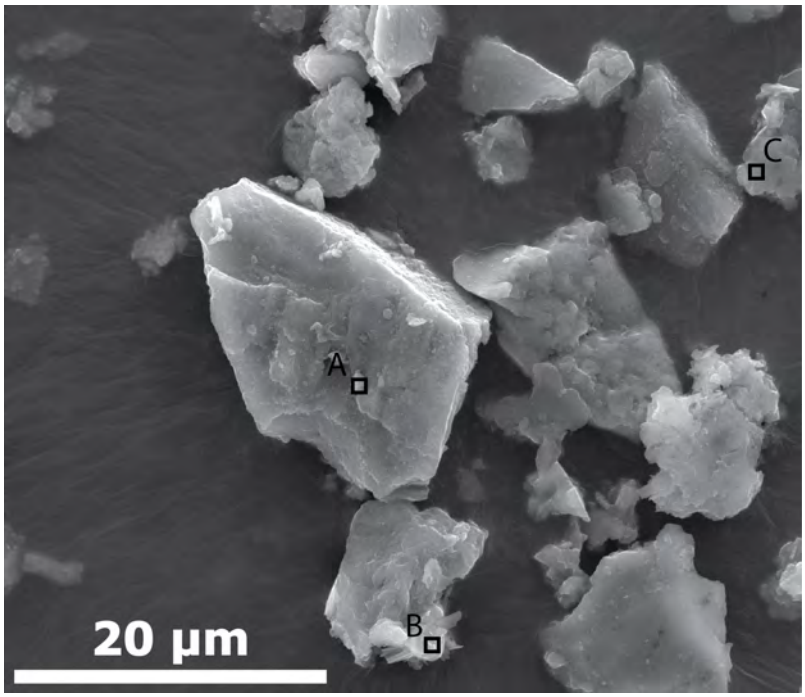

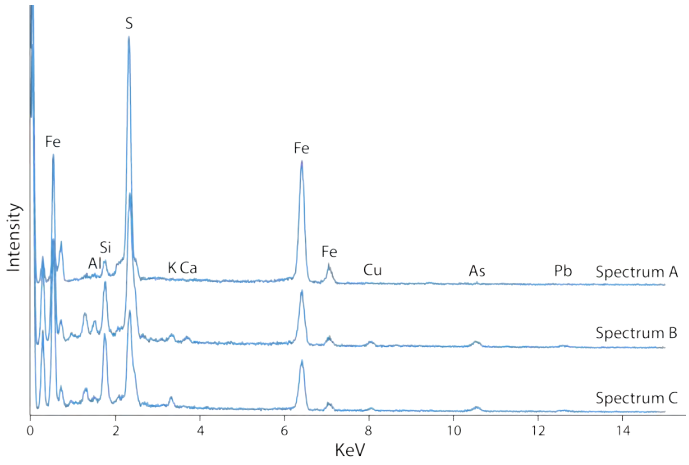

Figure 2.15: SEM image from sample Zim-PR-1-Top-1. Spectrum A identifies pyrite, spectrum B and C are jarosite with Cu, As, and Pb.

2.3.2.3 Gray Oxidized Samples

There were two oxidized samples that were similar in gray color: Zim-PR-2-Gray-2 (Figure 2.4) and Zim-PR-1-Smiddle-2. These samples had scorodite ($Fe^{3+}As^{5+}O_4 \cdot 2\,H_2O$), jarosite ($KFe(SO_4)(OH)_6$), sphalerite ($(Zn,Fe^{2+})S$), pyrite ($Fe^{2+}S_2$), gypsum ($CaSO_4 \cdot 2\,H_2O$), and quartz ($SiO_2$). The sample Zim-PR-2-Gray-2 contained highest amount of arsenic that was associated with scorodite, which was confirmed with XRD (Figures 2.16 and 2.17), SEM (Figures 2.18, 2.19,and 2.20), and TEM (Figure 2.21).

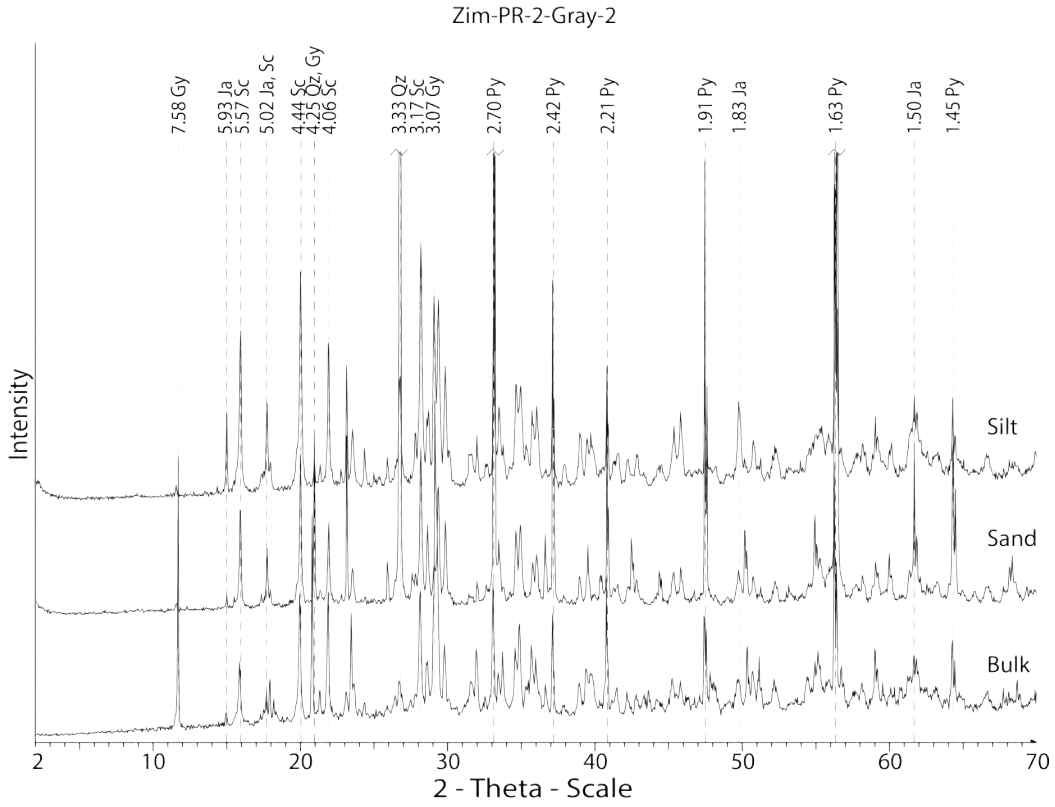

Figure 2.16: XRD patterns of the silt, sand, and bulk factions for sample Zim-PR-2-Gray-2. Sc = Scorodite, Ja = Jarosite, Py = Pyrite, Gy = Gypsum, Qz = Quartz.

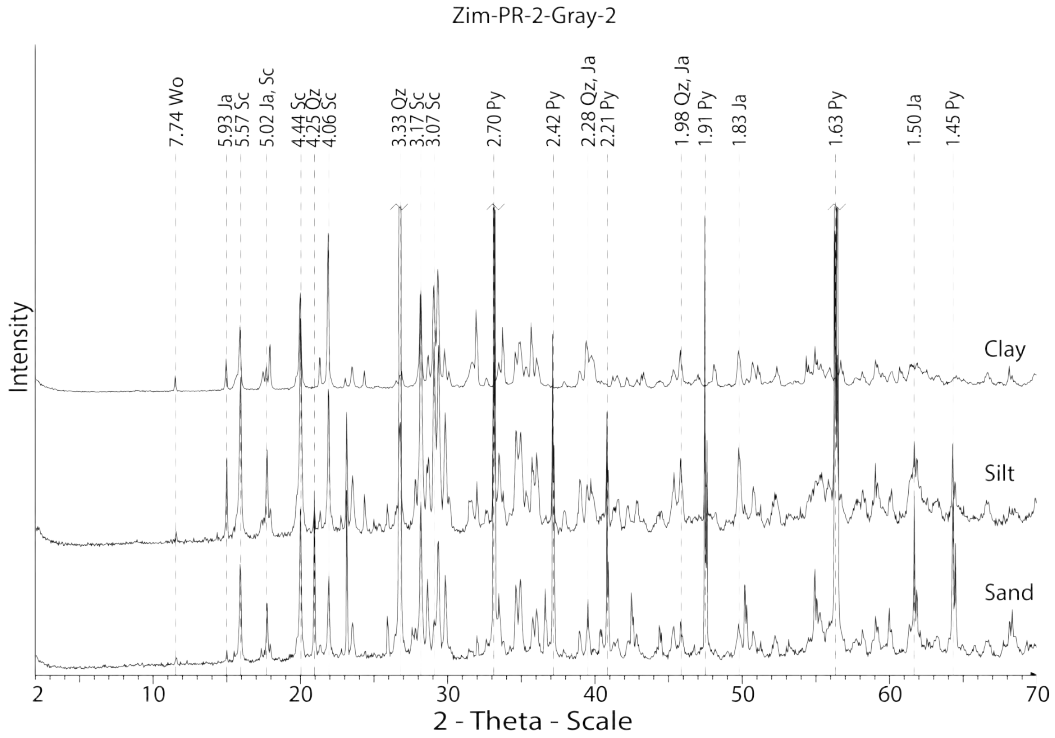

Figure 2.17: XRD patterns of the silt, sand, and clay factions for sample Zim-PR-2-Gray-2. Sc = Scorodite, Ja = Jarosite, Py = Pyrite, Qz = Quartz.

SEM analysis revealed a submicron sized iron-arsenic rich coating on the sample Zim-PR-2-Gray-2 (Figure 2.18), they were likely scorodite. Relatively pure scorodite was identified in the silt fraction (Figure 2.18) and in the clay fraction (Figures 2.17 and 2.19) of this specimen. The euhedral cubic morphology of scorodite indicated it formed as a highly crystalline phase in the tailings.

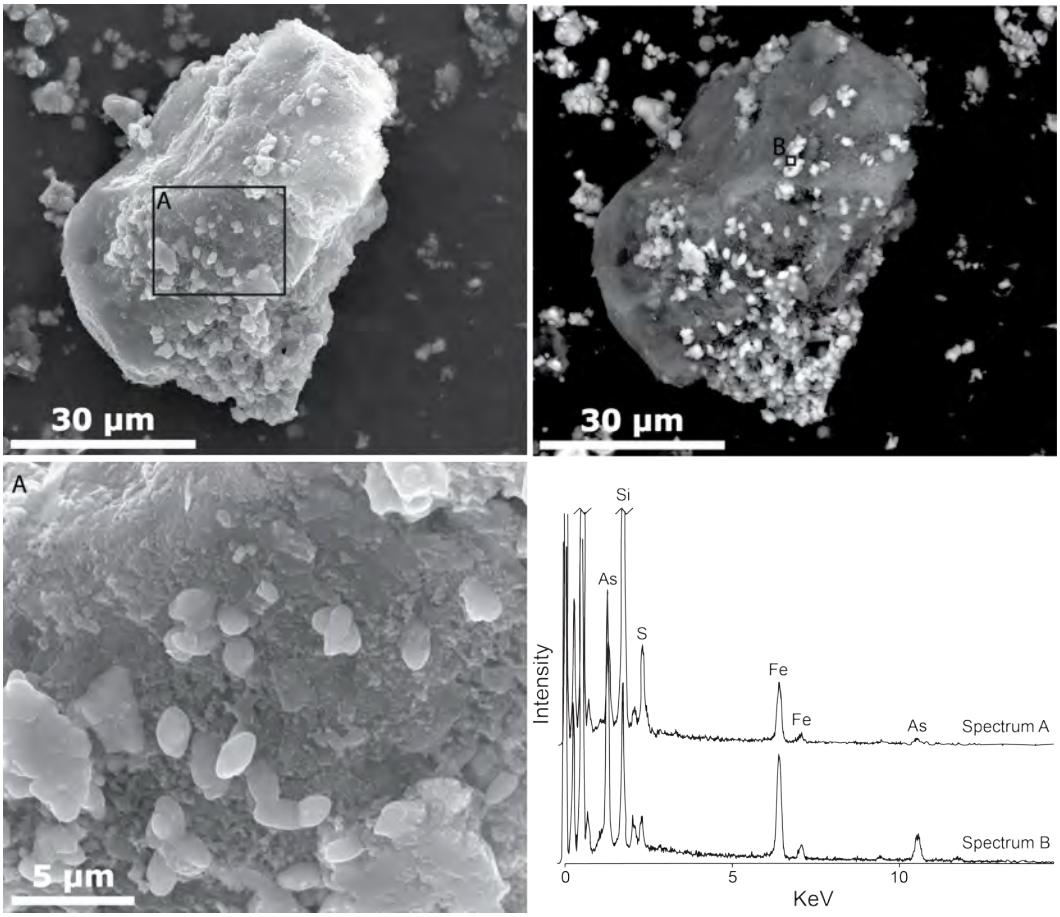

Figure 2.18: A large particle with an arsenic rich coating in the silt size fraction of the sample Zim-PR-2-Gray-2. Spectrum A examines the major particle, while spectrum B is focused on a coating particle.

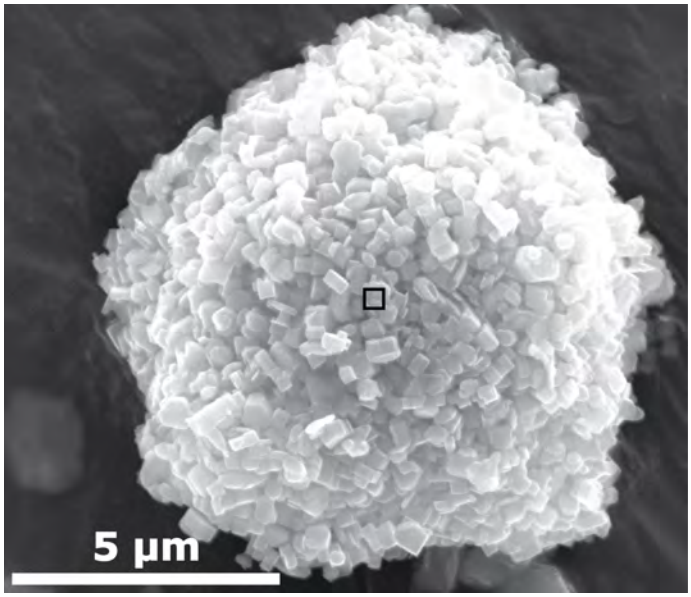

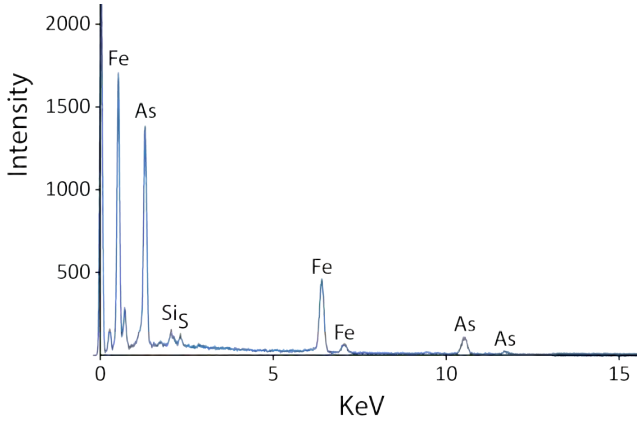

Figure 2.19: SEM image from sample Zim-PR-2-Gray-2 silt fraction with a large aggregate of scorodite and its EDS spectrum.

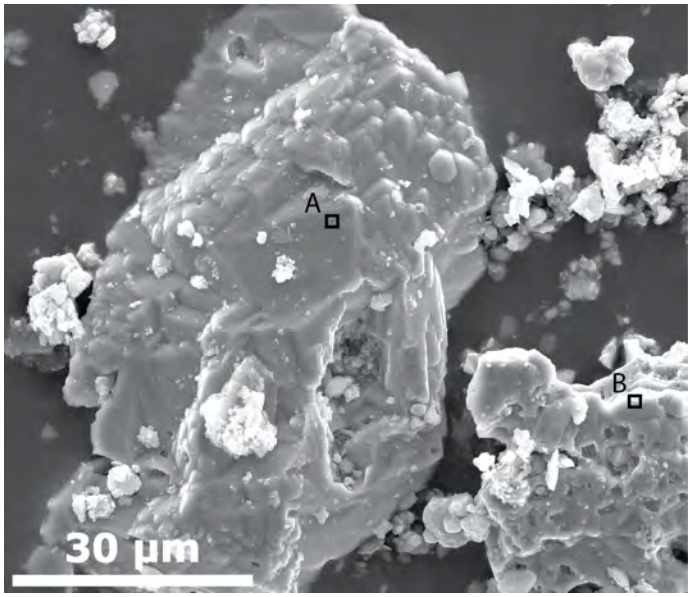

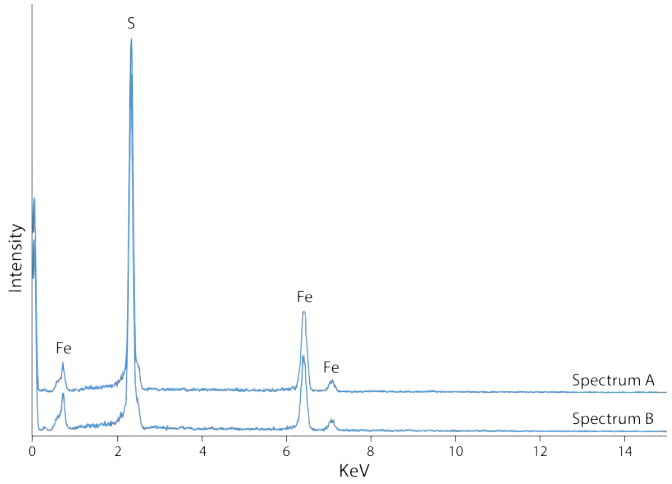

Figure 2.20: SEM image from sample Zim-PR-2-Gray-2 with two weathered particles of pyrite.

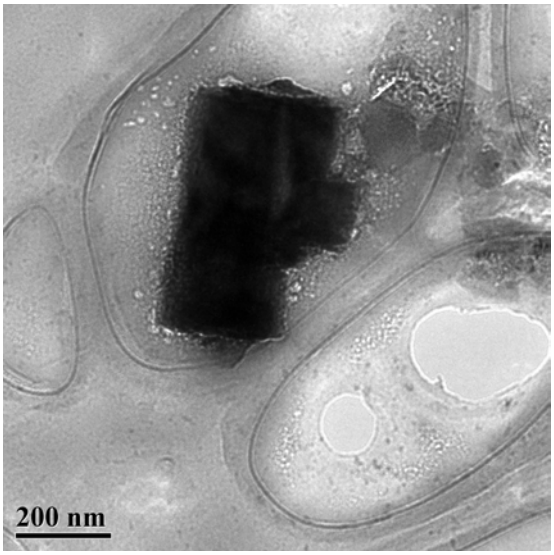

(a) TEM

(b) Diffraction

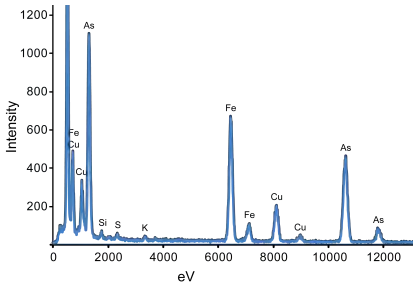

(c) EDS spectra

Figure 2.21: TEM analysis of the silt fraction of the sample Zim-PR-2-Gray-2 where (a) is the particle examined, (b) the selected area electron diffraction (SAED) pattern shows a semi-crystalline particle, and (c) the EDS spectra indicated a strong presence of arsenic.

2.3.3 Unoxidized Samples

The Zim-PR-2-Fresh-1 sample was collected from a barrier wall used to control water runoff at the Preisser Mine (Figure 2.22). The newest tailings deposited at the

site that were collected during sampling contained the highest amount of primary minerals such as feldspars($(K,Na,Ca)AlSi_3O_8$), pyrite (FeS_2), pyrrhotite (FeS), and sphalerite ((Zn,Fe)S) (Figure 2.23). However, there were still iron oxides and ferric sulfate minerals present (Figure 2.24).

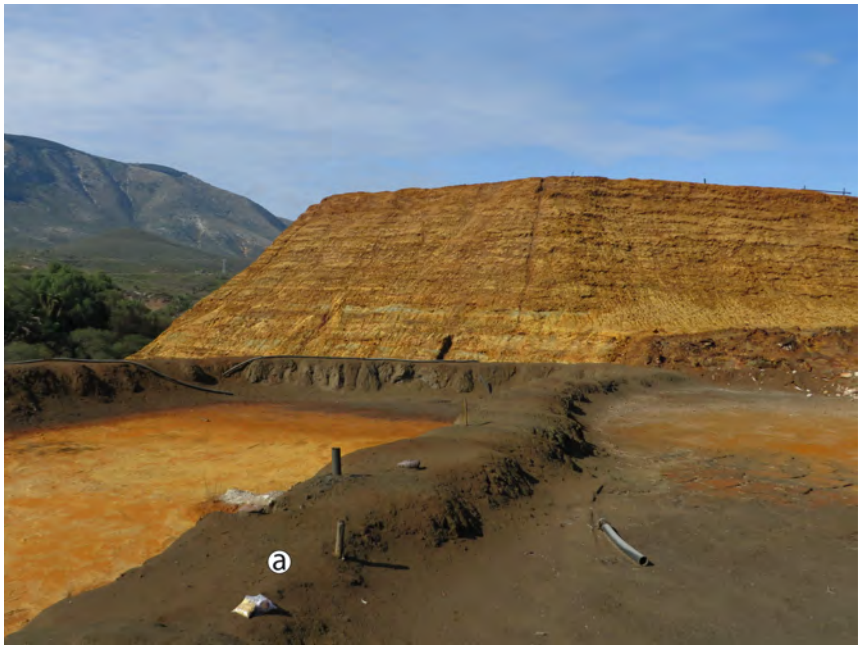

Figure 2.22: The Preisser Mine used fresh tailings to build barrier walls for retention ponds and to control runoff. This is where sample (a)Zim-PR-2-Fresh-1 was collected. The bottom of the damp pond can be seen to accelerate oxidation of the sediment.

The sample Zim-PR-2-Fresh-1 was size fractionated and also had a magnetic phase removed from the bulk fraction, then each underwent XRD analysis separately to reveal it was dominated by pyrrhotite (Figure 2.23). The SEM analysis observed the incorpation of Zn in iron oxides (Figure 2.24).

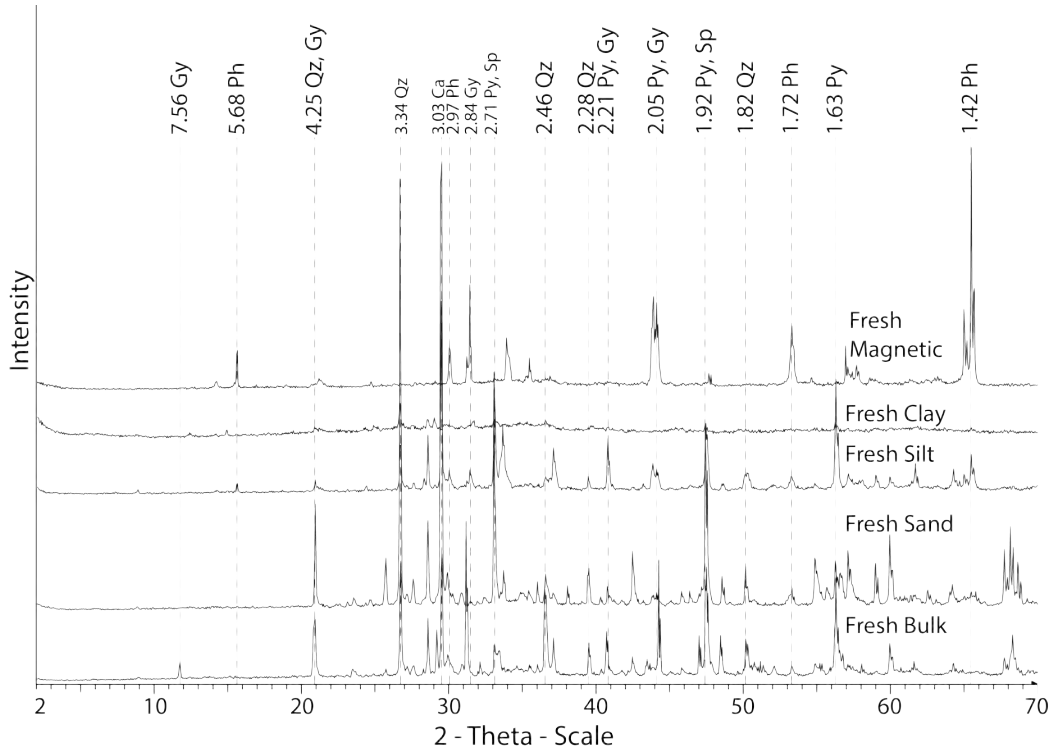

Figure 2.23: XRD patterns of the silt, sand, clay, and magnetic factions for sample Zim-PR-2-Fresh-1. Ph = Pyrrhotite, Ca = Calcite, Py = Pyrite, Sp = Sphalerite, Gy = Gypsum, Qz = Quartz.

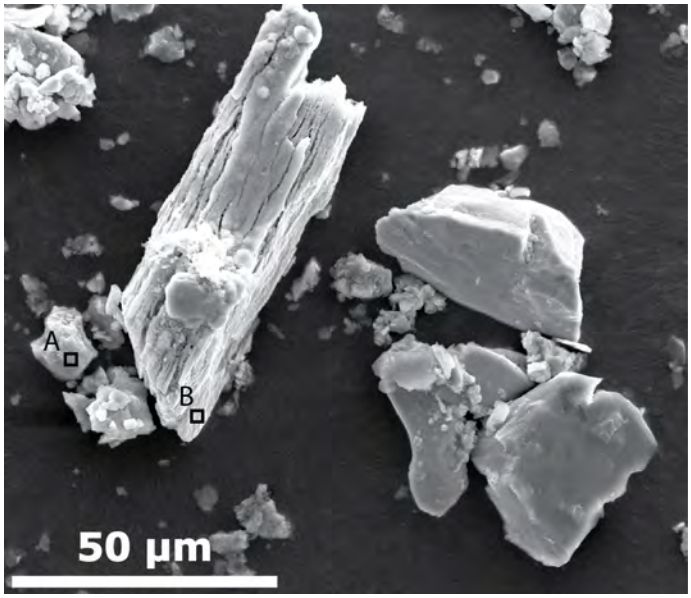

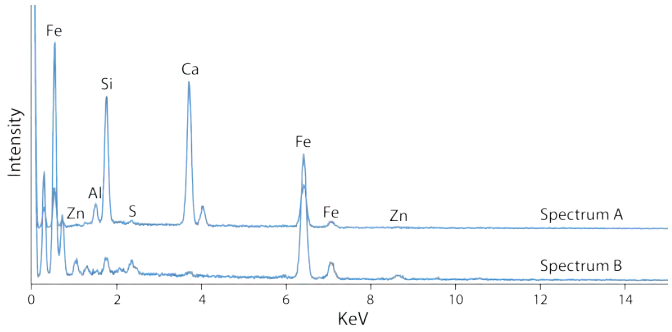

Figure 2.24: SEM image from sample Zim-PR-2-Fresh-1. Spectrum A and B identifies two pyroxenes, one incorporating Zn.

The sample Zim-SMV-2 came from a different mine site, San Miguel Viejo Mine (Figure 2.3). This sample was gray in color and exhibited few signs of oxidation (Figure 2.25). Gypsum and quartz dominated the pattern, although, no other fractions were separated.

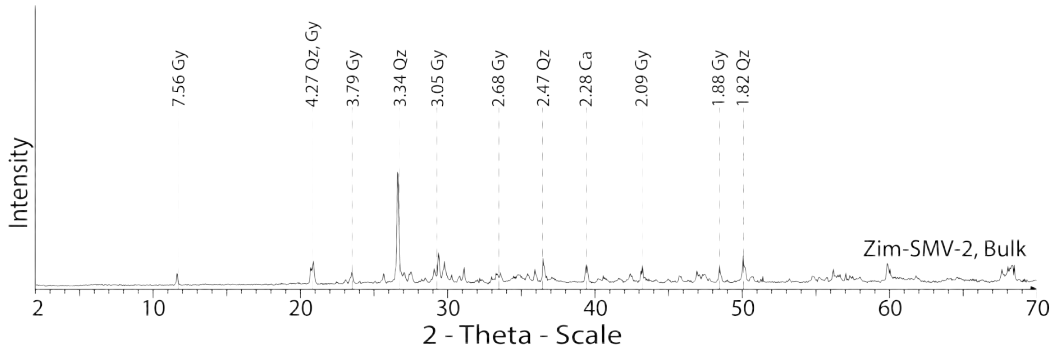

Figure 2.25: XRD pattern of the bulk fraction of sample SMV-2. Gy = Gypsum, Qz = Quartz, Ca = Calcite.

2.3.4 Minerals and Heavy Metals in a Soluble Sulfate Area

The soluble sulfates were easily spotted on the side of tailing heaps because of their bright white, orange, and green colors (Figures 2.27 and 2.26). The minerals found were melanterite ($Fe^{2+}SO_4 \cdot 7\,H_2O$), boyleite ($(Zn,Mg)SO_4 \cdot 4\,H_2O$), and rozenite($Fe^{2+}SO_4 \cdot 4\,H_2O$). Boyleite was collected as a white powder in sporadic, isolated areas on tailing heaps. The samples labeled as SMV-4 and Zim-1-Nside-4, coming from different mine tailing piles, contained high amounts of boyleite.

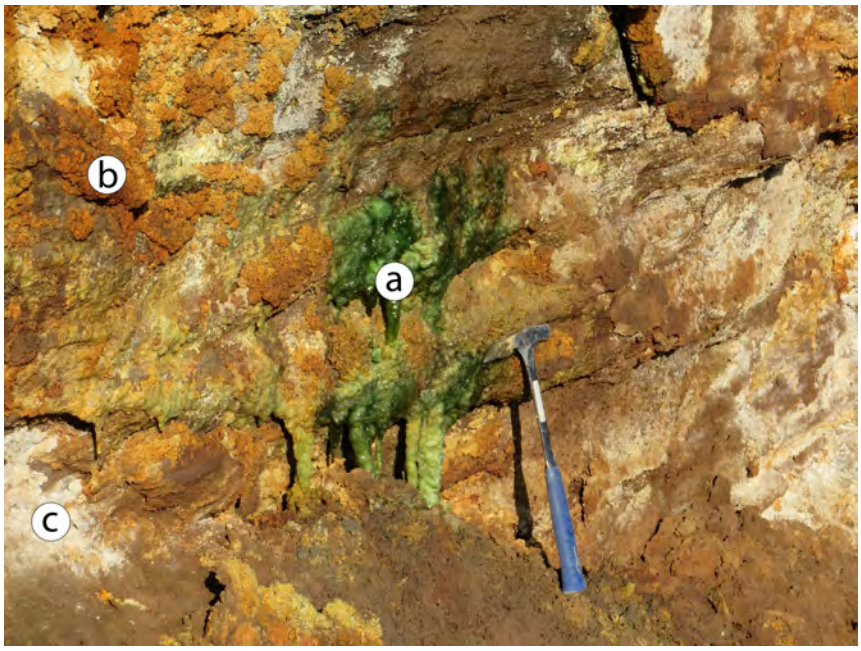

Figure 2.26: Soluble sulfates precipitate on the Preisser Mine. Three samples were collected here: a=Zim-1-Nside-1, b=Zim-1-Nside-3, and c=Zim-1-Nside-4.

2.3.4.1 White Soluble Sulfate Samples

The white samples, Zim-1-Nside-4 and SMV-4, had an abundance of boyleite ($(Zn,Mg)SO_4 \cdot 4\,H_2O$), and lesser so gypsum, pyrite, and quartz (SiO_2) (Figure 2.28). The XRF results (Table 2.5) indicated that the largest discrepancy between the two was that SMV-4 had 3.43% Fe from boyleite and Zim-1-Nside-4 had 22.11% Fe from rozenite. Conversely, SMV-4 had more S at 17.68% and Zim-1-Nside-4 minimally had 7.91% S. This can be attributed to the different quantities of sulfates present. They are from two different tailing pile locations and presumably have different ages. There was evidance of boyleite during SEM analysis (Figures 2.29 and 2.30). The high Fe content in the Zim-1-Nside 4 was due to the presence rosennite (FeSO44H2o), which is an isocrystal of boyleite. The EDS spectrum A in (Figure 2.30) indicated arsenopyrite was sampled in the soluble sulfate.

Figure 2.27: Soluble sulfates precipitated on the side of a tailing pile at San Miguel Viejo Mine. This is where sample (a)SMV-4 was collected.

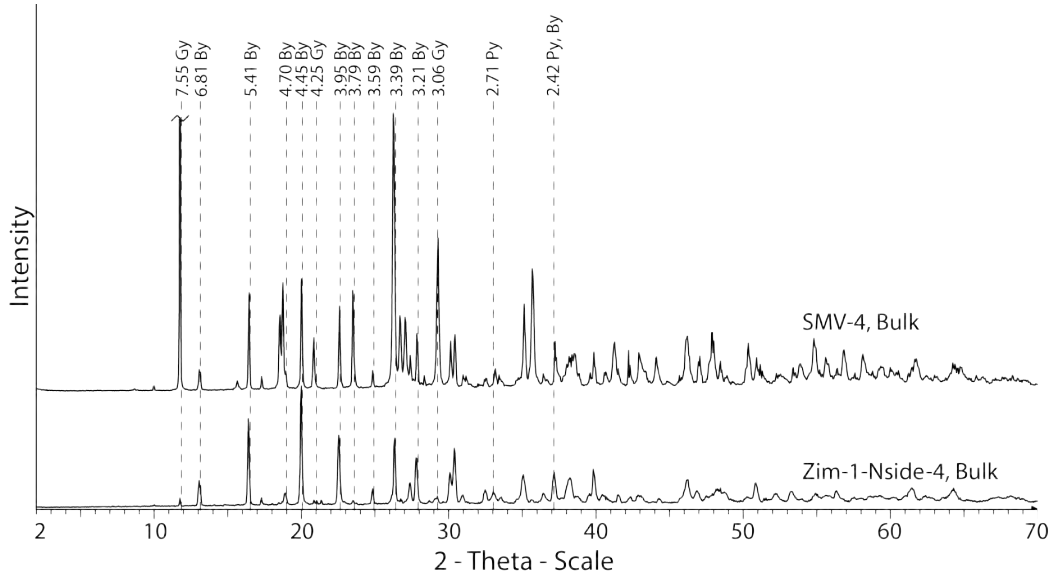

Figure 2.28: XRD patterns of two white samples that contained soluble sulfates. By = Boyleite, Py = Pyrite, and Gy = Gypsum.

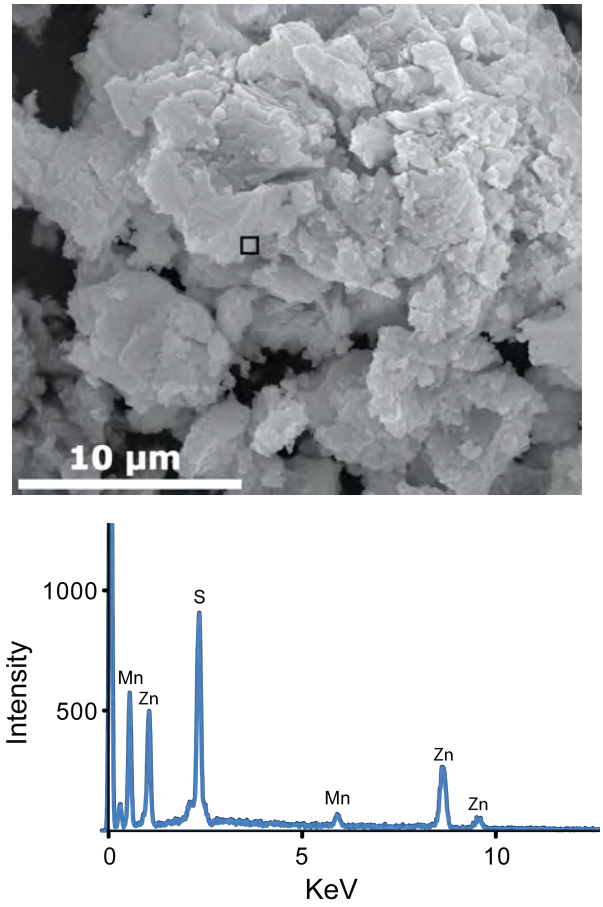

Figure 2.29: The sample SMV-4 was a white soluble sulfate. Here the sulfate boyleite, containing both Zn and Mn.

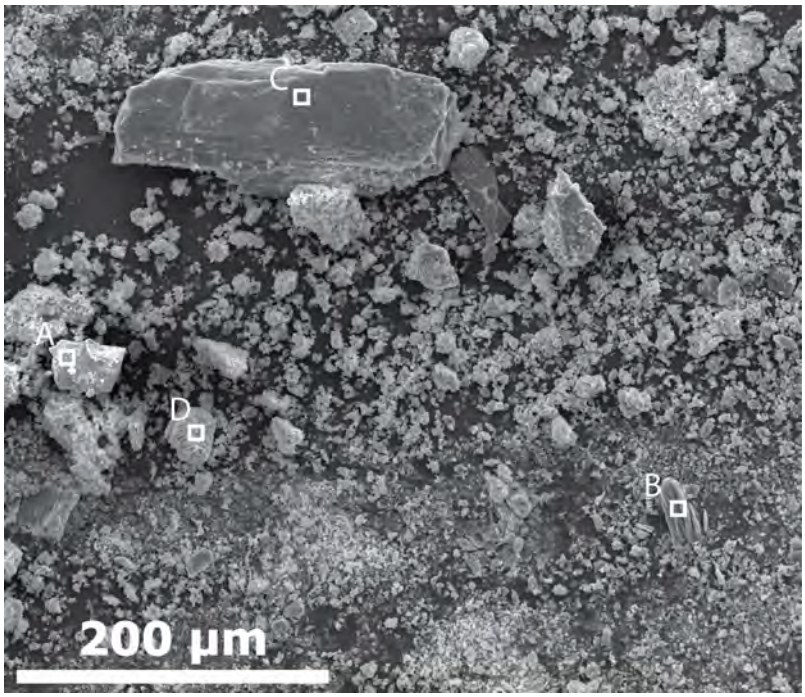

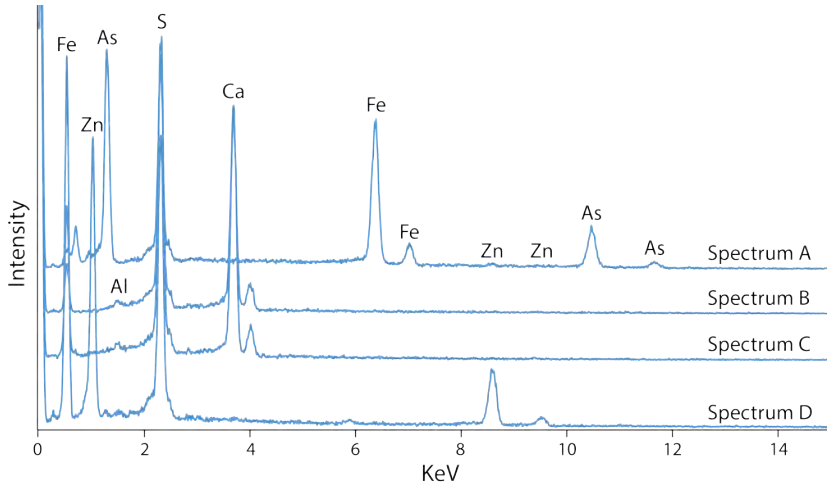

Figure 2.30: SEM image from sample Zim-SMV-4. Particle A is an arsenopyrite, particle B and C are gypsum, and particle D is boyleite.

2.3.4.2 Green and Orange Soluble Sulfate Samples

The samples Zim-1-Nside-1, Zim-1-Nside-3, and Zim-1-Nside-4 were collected in the same vicinity of one another on the side of the same tailing pile, but each noticeably differed by its color. They contained rozenite ($Fe^{2+}SO_4 \cdot 4\,H_2O$), boyleite ($(Zn,Mg)SO_4 \cdot 4\,H_2O$), pyrite, gypsum, and quartz. They all had nearly 3% P, 7% S, and $>$ 20% Fe as determined by XRF. This was consistent with the XRD that confirmed they are ferrous sulfates, such as melanterite and rozenite. In addition, they did contain a significant amount of other metals that could adsorb to iron complexes, such as Cu, As, and Pb. There was also copious amounts of Zn, which could be found in soluble boyleite ($(Zn,Mg)SO_4 \cdot 4\,H_2O$) or gunningite ($ZnSO_4 \cdot H_2O$). In the soluble sulfates, there was 30,878 to 465,104 mg/kg Zn per sample.

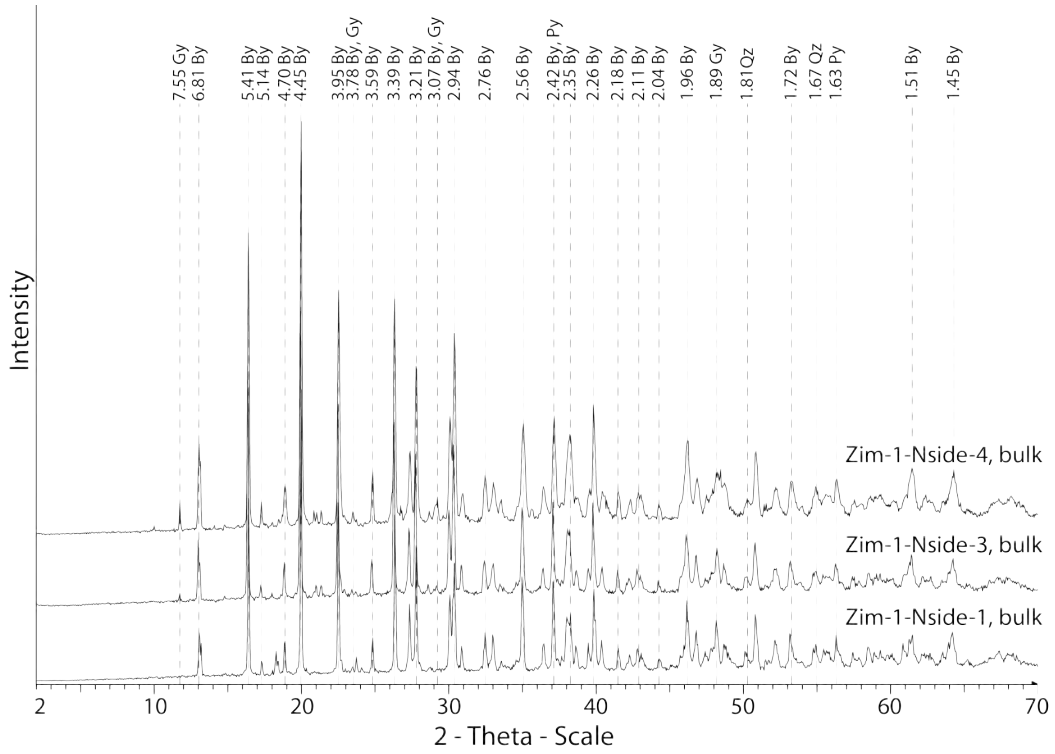

Figure 2.31: Samples Zim-1-Nside-1, Zim-1-Nside-3, and Zim-1-Nside-4 bulk fractions. By = Boyleite, Py = Pyrite, Gy = Gypsum, Qz = Quartz.

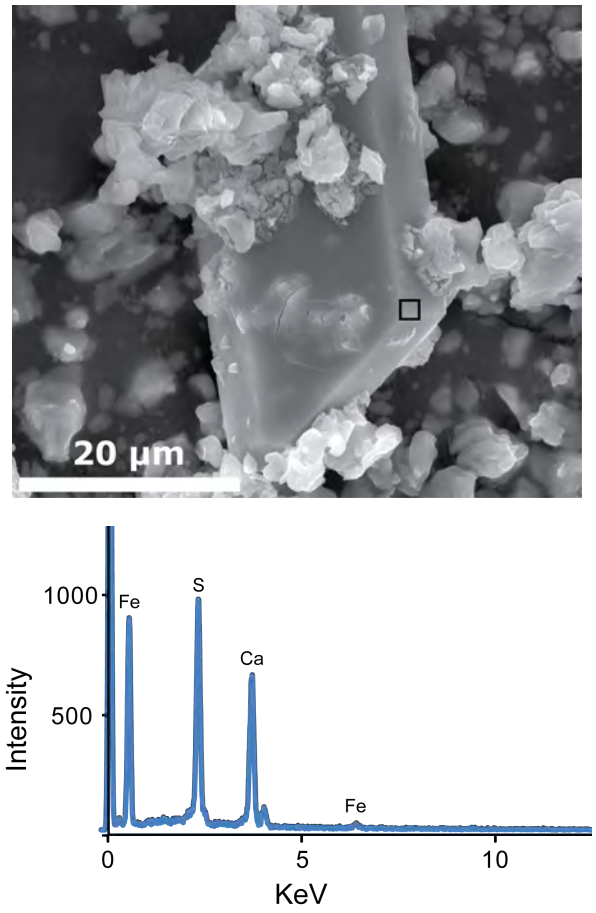

Figure 2.32: This particle of gypsum is from the green, water soluble sample, Zim-1-Nside-1. The sample had high amounts of hydrated iron sulfates.

2.3.4.3 River Sediment Not Affected By Tailings

The Toliman River runs only a few meters away from tailing sites of the San Mieguel Viejo and Pressier Mines, making it a potential transport pathway for AMD. Sample Zim-River-3 was the only sample not collected near any mine waste; it was about 4.83 Km (3 miles) northwest of city limits (Figure 2.33). Lead was found in its highest concentrations near the tailings and significantly less in samples collected distant from the tailings. Of all the samples collected around Zimapán, Zim-River-3 had the highest amount of Al and Si present, indicating a common silicate mineral

dominated sediments with little or no heavy metal contamination from the tailings.

Figure 2.33: River sediment was collected a few miles north of Zimapán and tailings deposit areas. Sample (a)Zim-River-3 was collected here.

Sample Zim-River-3 contained clay minerals montmorillonite, chlorite, and kaolinite, and also muscovite, anorthite, calcite, and quartz (Figures 2.34 and 2.35).

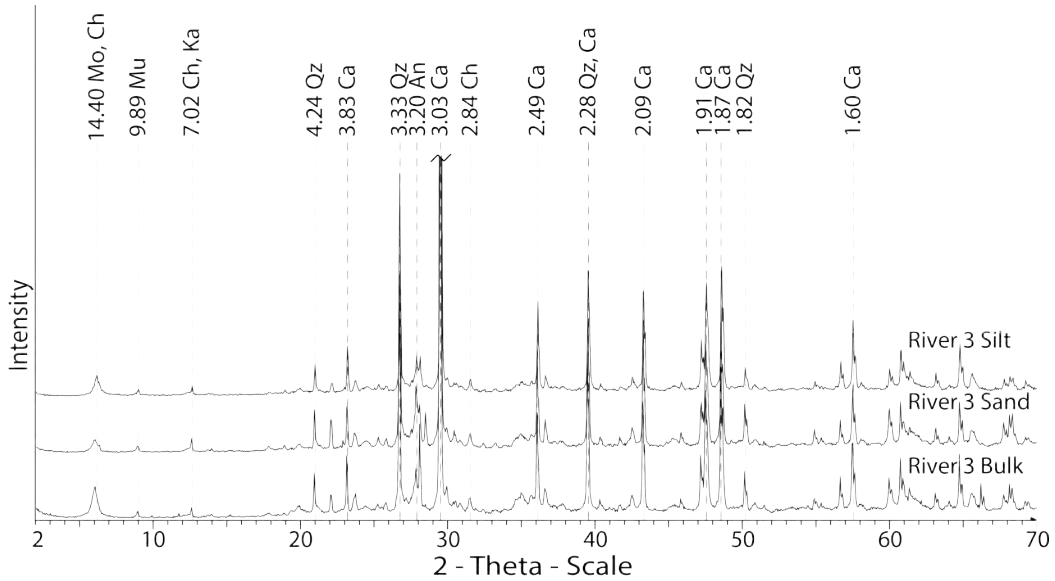

Figure 2.34: XRD patterns of the silt, sand, and clay factions for sample Zim-River-3. Mo = Montmorillonite, Ch = Chlorite, Mu = Muscovite, Ka = Kaolinite, An = Anorthite, Ca = Calcite, Qz = Quartz.

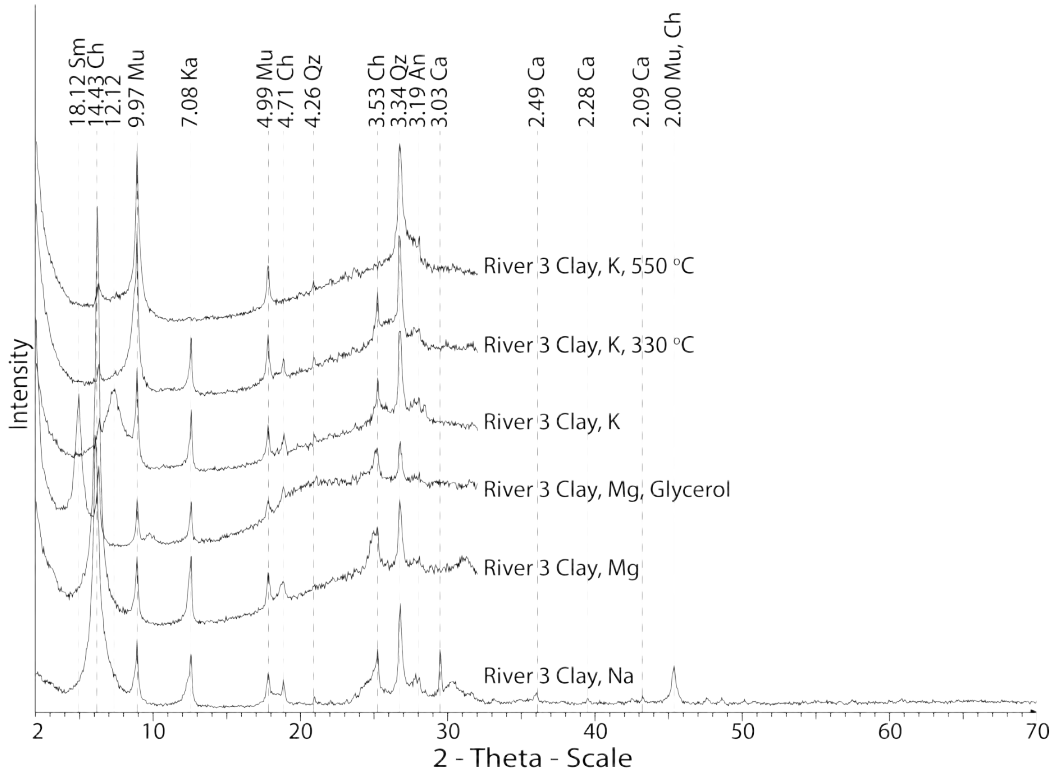

Figure 2.35: XRD patterns for sample Zim-River-3 clay size fraction treated by heat, cation saturation, and/or glycerol. Sm = Smectite, Ch = Chlorite, Mu = Muscovite, Ka = Kaolinite, An = Anorthite, Ca = Calcite, Qz = Quartz.

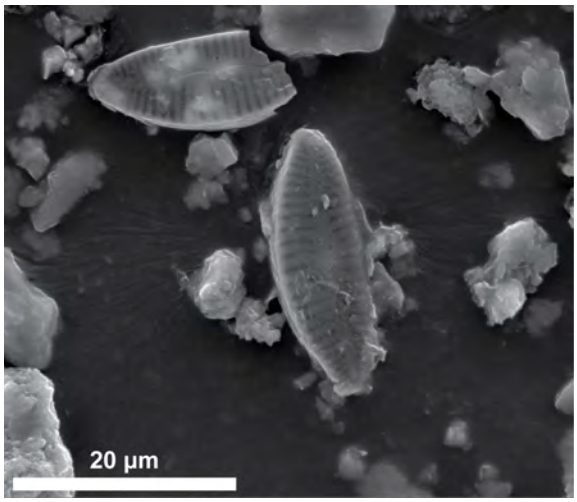

Figure 2.36: Diatom fragments in a SEM image of river sediment, in sample Zim-River-3 silt size fraction.

The SEM images of the river samples also contained diatoms, aquatic micro algae (Figure 2.36) (Hildebrand and J.L. Lerch, 2015).

The FTIR bands were mainly due to smectite (montmorillonite), kaolinite ($Al_2Si_2O_5(OH)_4$), calcite ($CaCO_3$), jarosite ($KFe^{3+}(SO_4)(OH)_6$), and quartz (SiO_2). Quartz is shown by a doublet at about 780 cm^{-1} and 796 cm^{-1}. Jarosite has peaks between 996 cm^{-1} and 1204 cm^{-1}, and at 3364 cm^{-1}. Peaks at approximately 2400 cm^{-1} and 618 cm^{-1} are from CO_2, while peaks at 1636 cm^{-1} are from H_2O. Crystalline calcite has peaks near 1400, 870 and 710 cm^{-1}; likewise, if the 710 cm^{-1} peak is not present it is noncrystalline calcium carbonate. Smectite is near 3620 cm^{-1} and kaolinite peak are roughly at 3695 cm^{-1} (Figure 2.37).

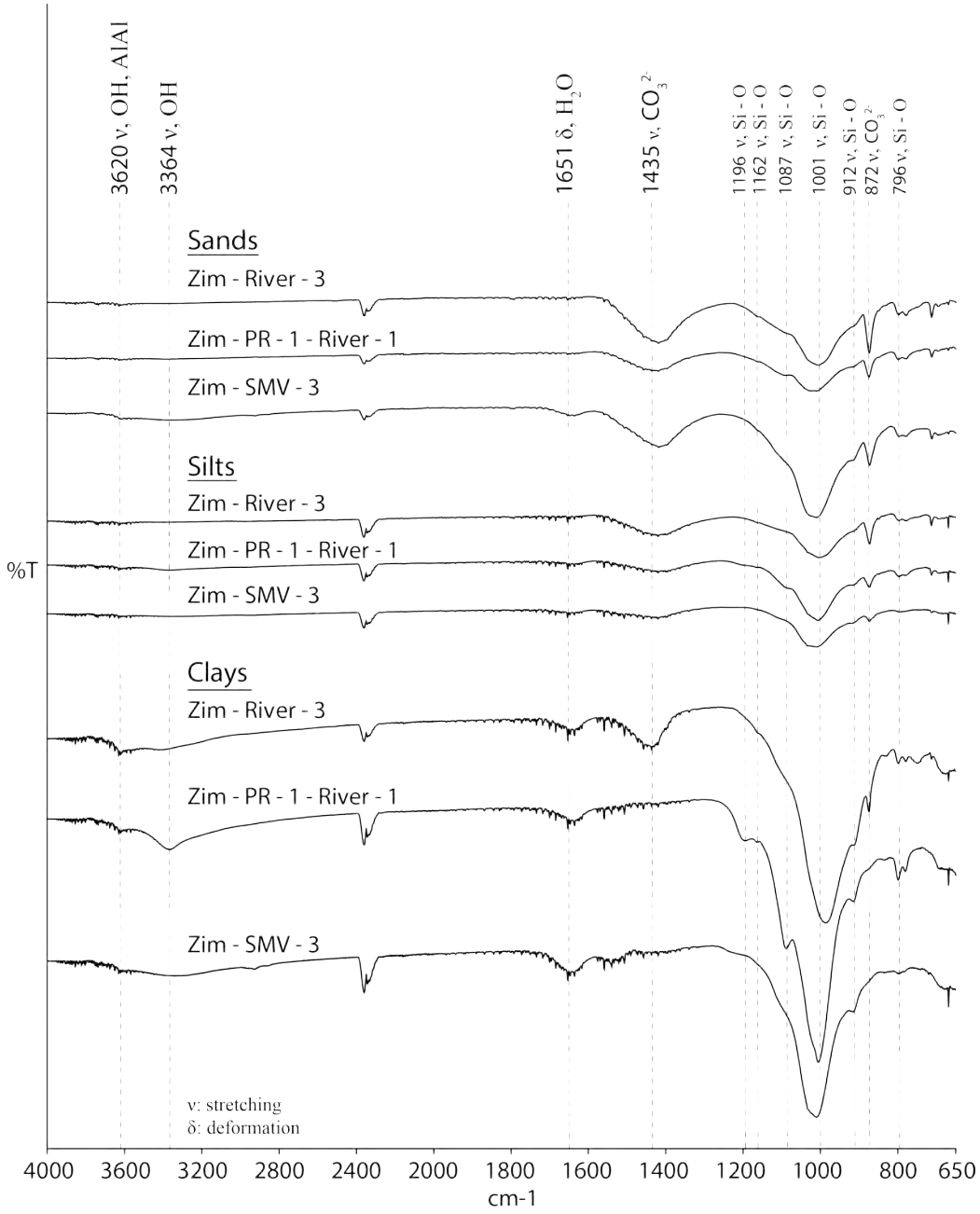

Figure 2.37: FTIR-ATR of all river sediment samples' size fractions: sand, silt, and clay.

2.3.5 River Sediment Near Mine Tailings

The largest differences in the mineralogy of the river samples were seen in the clay fraction (Figures 2.39, 2.38, and 2.33). The two samples of sediments collected near tailing areas contained smectite, kaolinite ($Al_2Si_2O_5(OH)_4$), calcite ($CaCO_3$), and quartz (SiO_2). There were also differences in heavy metal concentrations when examined with XRF (Tables 2.5 and 2.6). The bulk fraction of river sediment XRD pattern gave the first indication of a high abundance of clay minerals and carbonates (Figure 2.40). The SEM analysis of silt fractions of all river samples showed diatoms were present (Figures 2.46 and 2.36).

The river sediment and Zim-PR-2-Fresh-1 tailings had pH closest to neutral while the other weathered tailings were highly acidic. The river sediments were similar in mineralogy as they contained quartz, calcite, and albite. They river sediments always had the highest amount of clay minerals such as smectite, kaolinite, and vermiculite.

Figure 2.38: Location of river sediment sample (a)Zim-PR-River-1, about 100m downstream of the Preisser Mine tailings.

Figure 2.39: This is the point of collection for river sediment sample (a)Zim-SMV-3. This is next to the San Miguel Viejo Mine tailings.

Another river sediment from the Toliman River was collected next to the Pressier Mine tailings (Figure 2.38). Sample Zim-PR-River-1 was downstream about 50 meters from tailing piles. Sample Zim-PR-1-River-1 contained the clay minerals smectite, and kaolinite ($Al_2Si_2O_5(OH)_4$), but also jarosite and quartz (Figures 2.41 and 2.42).

The sample Zim-SMV-3 is a river sediment sample that was collected downstream of an adjacent row of tailing piles (Figures 2.43 and 2.44). Iron calcium silicate clay minerals absorbed with Zn were observed in silt faction EDS analysis (Figure 2.45). The XRD pattern for sample Zim-SMV-3 indicated the clay fraction was dominated by poorly crystalline montmorillonite with minor amounts of kaolinite, and quartz (Figure 2.44).

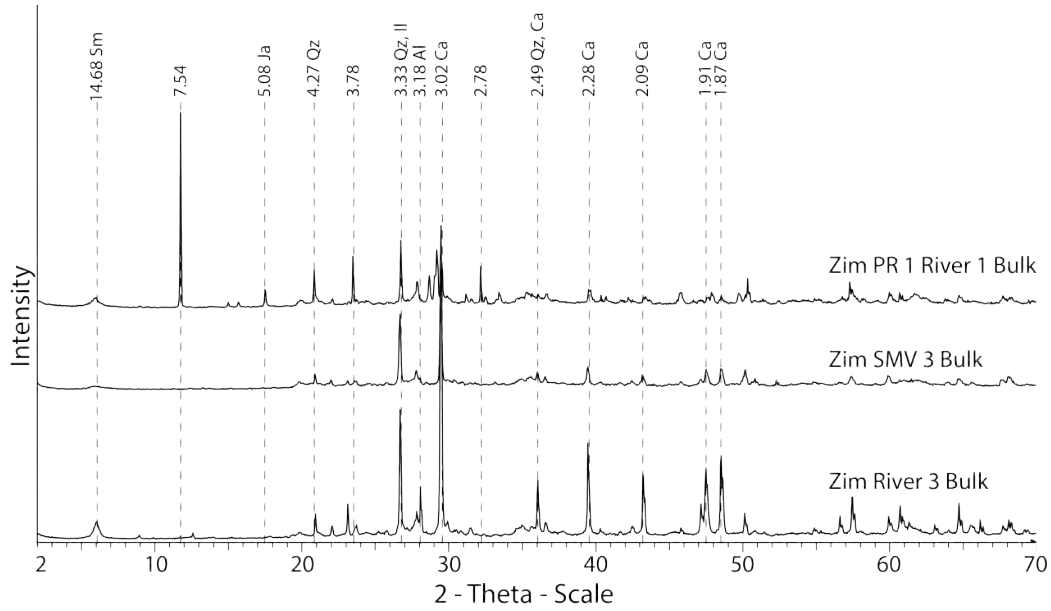

Figure 2.40: The bulk samples of all three river sediments collected. Sm = Smectite, Al = Alunite, Il = Ilmenite, Ja = Jaorsite, Ca = Calcite, Qz = Quartz.

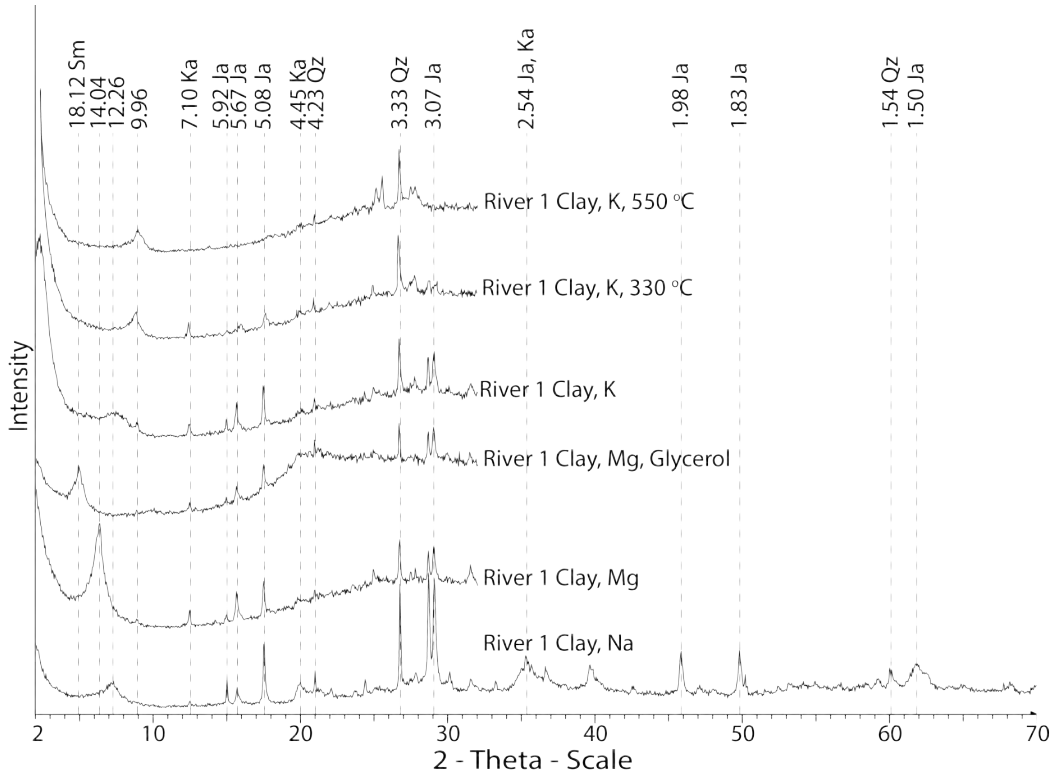

Figure 2.41: XRD patterns for sample Zim-PR-1-River-1 clay size fraction treated by heat, cation saturation, and/or glycerol. Sm = Smectite, Ka = Kaolinite, Ja = Jaorsite, Qz = Quartz.

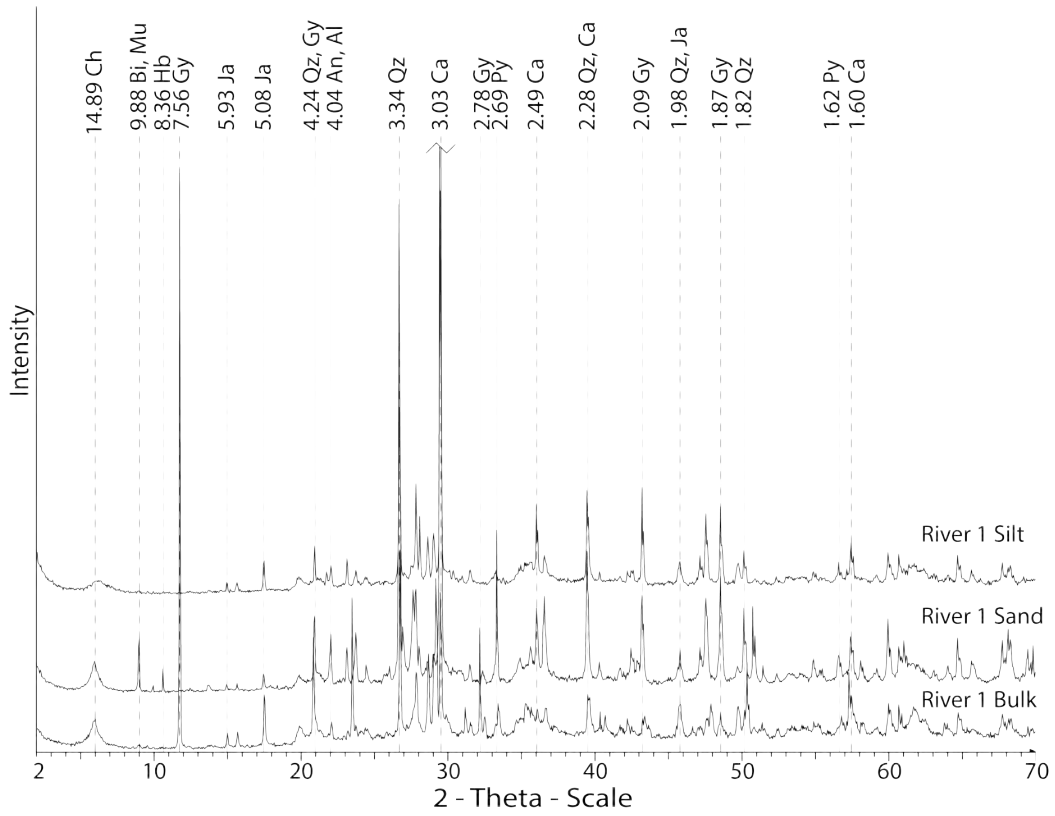

Figure 2.42: XRD patterns of the silt, sand, and clay factions for sample Zim-PR-1-River-1. Ch = Chlorite, Mu = Muscovite, Bi = Biotite, Hb = Hornblende, An = Anorthite, Al = Alunite, Py = Pyrite, Gy = Gypsum, Ja = Jarosite, Ca = Calcite, Qz = Quartz.

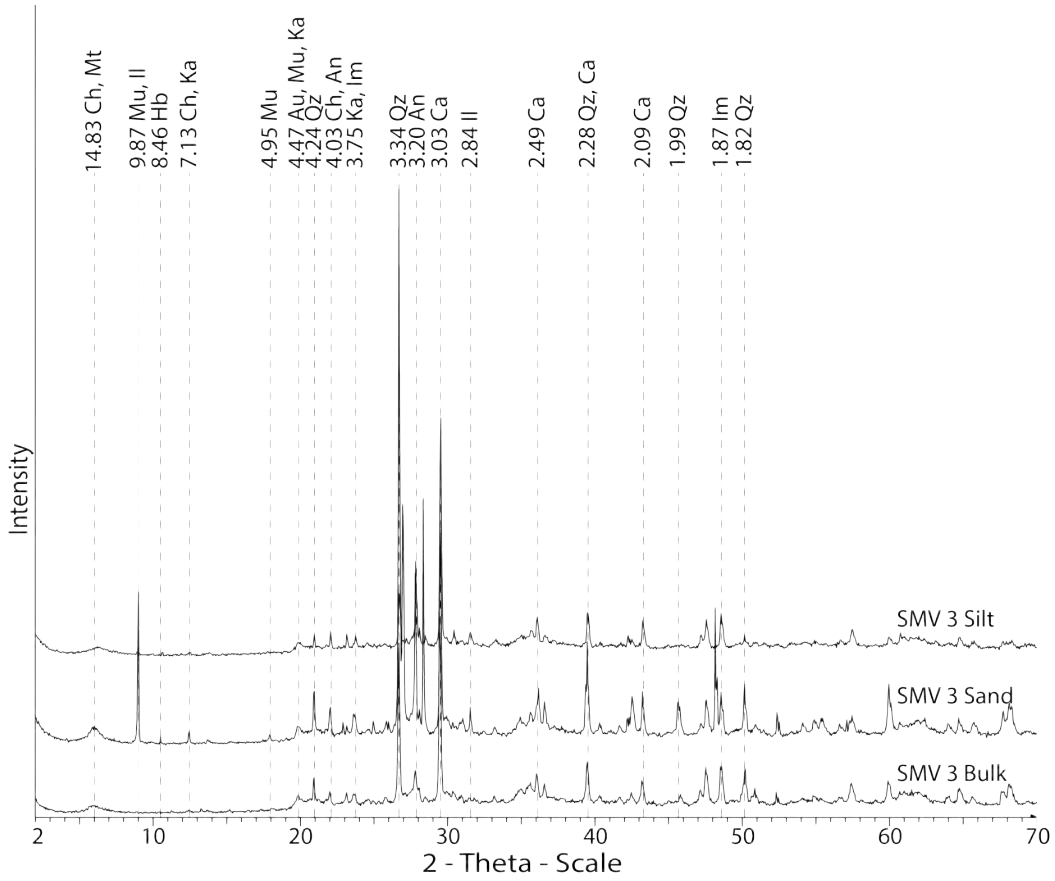

Figure 2.43: XRD patterns of the silt, sand, and bulk factions for sample Zim-SMV-3. Mt = Montmorillonite, Mu = Muscovite, Il = Illite, Ch = Chlorite, An = Anorthite, Ca = Calcite, Ka = Kaolinite, Au = Augite, Im = Ilmenite, Hb = Hornblende, Qz = Quartz.

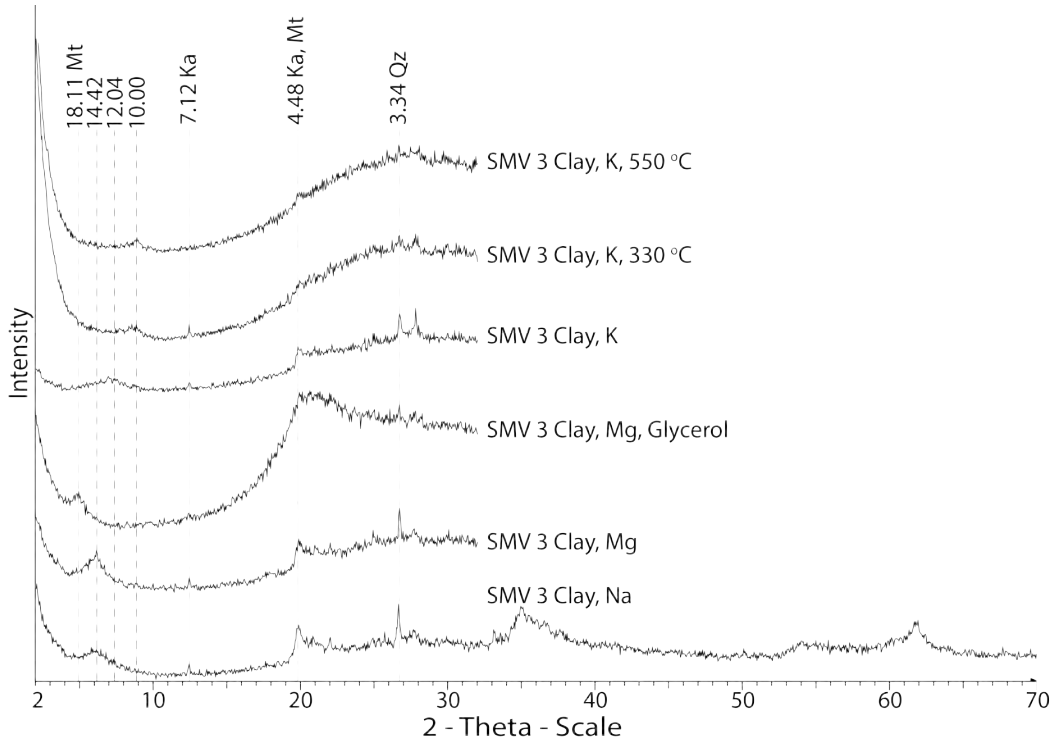

Figure 2.44: XRD patterns for sample Zim-SMV-3 clay size fraction treated by heat, cation saturation, and/or glycerol. Mt = Montmorillonite, Ka = Kaolinite, Qz = Quartz.

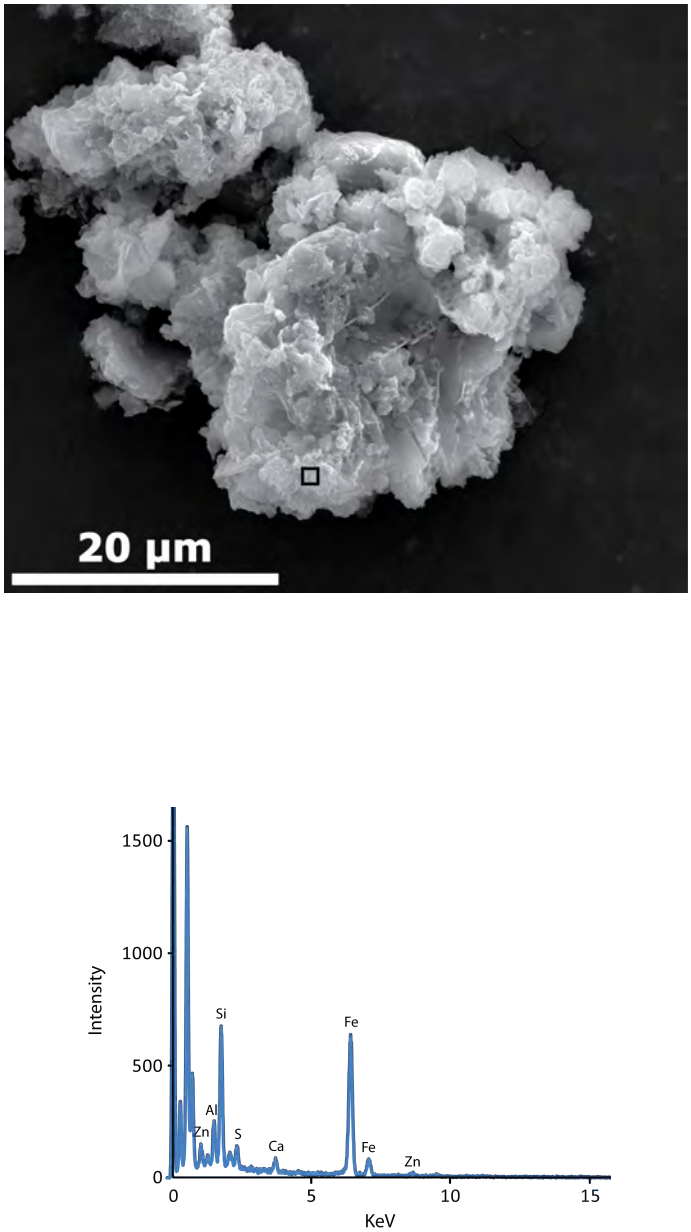

Figure 2.45: Particle in sample Zim-SMV-3 silt fraction with it's EDS spectrum. This river particle is an aggregate of several clay minerals and iron oxides.

Figure 2.46: A diatom in river sediment sample Zim-SMV-3 silt size fraction.

2.4 Discussion

The possible geochemical pathways were deduced from the mineral composition that remained in each sample. Primary sulfides, such as pyrite and pyrrhotite, in mined ore were eventually oxidized and transformed into an iron oxide derivative or formed a sulfate complex. Hydrated minerals, such as melanterite ($Fe^{2+}SO_4 \cdot 7\,H_2O$), rozenite, copiapite, and boyleite ($(Zn,Mg)SO_4 \cdot 4\,H_2O$), phases were sporadic because of the random leaching to an arid environment. Equations 2.1-2.3 show how the oxidation of the primary sulfides pyrite and pyrrhotite can contribute to acidic conditions.

$$\underset{\text{Pyrite}}{FeS_2} + 3.5\,O_2 + H_2O \longrightarrow Fe^{2+} + 2\,{SO_4}^{2-} + 2\,H^+ \tag{2.1}$$

$$\underset{\text{Pyrrhotite}}{Fe_7S_8} + 15.5\,O_2 + H_2O \longrightarrow 7\,Fe^{2+} + 8\,{SO_4}^{2-} + 2\,H^+ \tag{2.2}$$

$$\underset{\text{Pyrrhotite}}{Fe_7S_8} + 6\,H^+ + 1.5\,O_2 \longrightarrow 4\,\underset{\text{Pyrite}}{FeS_2} + 3\,Fe^{2+} + 3\,H_2O \tag{2.3}$$

Ferrous iron from primary minerals was a source of iron for soluble sulfates and copiapite. Once ferrous iron is oxidized by either biotic and/or abiotic pathways, it will become an iron oxide or sulfate complex. The new compounds, such as goethite, and jarosite are more stable than the phases which they were formed from. Ferric (oxy)hydroxides readily absorbed heavy metals until acidic conditions disrupted their stability. The older tailings with more oxidized iron oxides would then be able to retain metal contaminants better than fresh tailings. The absorption of metals were dependent on many factors that are difficult to control, such as temperature and moisture, but their exposure could be limited by a carbonate covering. The natural limestone in the subsurface environment reacts with the sulfuric acid produced by the oxidation of sulfides to neutralize some acidity and precipitate gypsum, but does not end leaching of low pH waters.

The river sediment samples and the fresh tailings had the highest amount of clay minerals and the most neutral pH of all the samples collected. The river sediments did not show chemical influence from acidic affluent runoff. The pH can be controlled due to constant dilution, continuous contact with carbonate environments, and interactions with clay minerals that can consume acidic conditions.

$$\underset{\text{Kaolinite}}{Al_2Si_2O_5(OH)_4} + 6\,H^+ \longrightarrow H_2O + 2\,H_4SiO_4 + 2\,Al^{3+} \tag{2.4}$$

$$\underset{\text{Muscovite}}{KAl_3Si_3O_{10}(OH)_2} + 10\,H^+ \longrightarrow 3\,Al^{3+} + 3\,H_4SiO_4 + K^+ \tag{2.5}$$

The arid environment in the region allows for soluble sulfates to be stable for a reasonable amount of time until the next episode of precipitation to dissolve formations on the exterior of tailing piles. Ferrous soluble sulfates can be a temporary sink for mobile metals.

$$Fe^{2+} + {SO_4}^{2-} + 7\,H_2O \longrightarrow \underset{\text{Melanterite}}{Fe^{2+}(SO_4)\cdot 7\,H_2O} \tag{2.6}$$

$$\underset{\text{Melanterite}}{Fe^{2+}(SO_4)\cdot 7\,H_2O} \longrightarrow \underset{\text{Rozenite}}{Fe^{2+}(SO_4)\cdot 4\,H_2O} + 3\,H_2O \tag{2.7}$$

There are many variations that a mineralogical pathway could follow, but scorodite ($Fe^{3+}As^{5+}O_4\cdot 2\,H_2O$) can form from solution then lead to hematite ($\alpha{-}Fe_2^{3+}O_3$) and then lepidocrite ($\gamma{-}Fe^{3+}OOH$) or ferrihydrite ($Fe^{3+}OOH\cdot 0.5\,H_2O$).

$$\underset{\text{Scorodite}}{Fe^{3+}As^{5+}O_4\cdot 2\,H_2O} + OH^- \longrightarrow \underset{\text{Ferrihydrite}}{FeOOH\cdot 0.5\,H_2O} + H_2As^{3+}{O_4}^- + 0.5\,H_2O \tag{2.8}$$

A more complete study could include core samples from the tailing piles, below the tailings, and around the tailings to get a better understanding of the distance that AMD can leach before it is neutralized and by what means necessary. From this research we can see that the acidity of tailings does not greatly affect the river water pH, but the sediment showed contributions of minerals from the tailings. A greater sample size of river samples would also help solidify mineral findings from

this research. In addition, there are more areas containing water that can be evaluated for different studies. Different minerals would be suspected to have varying mobility characteristics, specifically at the nearby river. The solubility of a mineral is a characteristic used to determine its mobility and bioavailability. For example, scorodite (log K_{sp} -25.74) is fairly insoluble compared to the arsenide, arsenolite (Table 2.7)(Harvey et al., 2006). Future studies could include isotopic labeling of mineral species to track their mobility distance and pathway, whether it be air, soil, or water. Complex pathways for iron oxides alone would make the identification of pathways difficult and predictions almost impossible due to seasonal weather variance.

$$\mathrm{Fe^{3+}} + 3\,\mathrm{H_2O} \longrightarrow \underset{\text{Ferrihydrite}}{\mathrm{Fe^{3+}(OH)_3}} + 3\,\mathrm{H^+} \tag{2.9}$$

$$\mathrm{Fe^{3+}} + 2\,\mathrm{H_2O} \longrightarrow \underset{\text{Goethite}}{\alpha\text{–}\mathrm{Fe^{3+}OOH}} + 3\,\mathrm{H^+} \tag{2.10}$$

$$2\,\underset{\text{Goethite}}{\alpha\text{–}\mathrm{Fe^{3+}OOH}} \longrightarrow \underset{\text{Hematite}}{\alpha\text{–}\mathrm{Fe_2O_3}} + \mathrm{H_2O} \tag{2.11}$$

$$3\,\underset{\text{Hematite}}{\alpha\text{–}\mathrm{Fe_2{}^{3+}O_3}} + \mathrm{H_2} \longrightarrow 2\,\underset{\text{Magnetite}}{\mathrm{Fe_3O_4}} + \mathrm{H_2O} \tag{2.12}$$

$$\underset{\text{Hematite}}{\alpha\text{–}\mathrm{Fe_2O_3}} + \mathrm{H_2O} \longrightarrow 2\,\underset{\text{Lepidocrocite}}{\gamma\text{–}\mathrm{FeOOH}} \tag{2.13}$$

Heavy metals such as Zn, Cu, Pb, and As were mobilized or immobilized after oxidation, crystallization of sulfates, and formations of iron oxides. The XRF data gives a good outline of which metals are in which category of samples (Tables 2.5 and 2.6). The oxidized samples with iron oxides were able to retain Pb, Zn, As, but least of the four Cu. Copper and Zn were found in higher levels in the soluble sulfates, indicating their ability to be mobile. Unlike As and Pb that were found less in the soluble phases versus the oxidized samples. Some samples showed excessively low or high values metals in their category, demonstrating the heterogeneity of the tailing piles. Iron oxides and sulfates were able to adsorb As and Pb after oxidation and reduce their mobility for a semi-permanent duration of time. Crystallization of dehydrated soluble sulfates will only sequester Zn and Cu until the next weather event, then releasing all at once.

Mineral	Formula	Solubility	Temp.	pH	Source
Arsenolite	As_2O_3	11.1 g/L	22 ^{o}C		1
		2.05 g/100 mL	25 ^{o}C		2
Siderite	$FeCO_3$	0.000062 g/100 mL	20 ^{o}C		2
Scorodite	$FeAsO_4 \cdot 2\,H_2O$	0.33-5.89 mg/L	22 ^{o}C	5.01-6.99	1
		0.11-463 mg/L	23 ^{o}C	0.97-7.92	1
		1.8-10.3 mg/L	25 ^{o}C	5.53-6.36	1
Halite	NaCl	36.0 g/100 mL	25 ^{o}C		2
Gypsum	$CaSO_4 \cdot 2\,H_2O$	0.205 g/100 mL	20 ^{o}C		2
Calcite	$CaCO_3$	0.00066 g/100 mL	20 ^{o}C		2
Arsenic(V) oxide	As_2O_5	65.8 g/100 mL	20 ^{o}C		2
Arsenic(V) oxide	As_2O_5	65.8 g/100 mL	20 ^{o}C		2
Melanterite	$FeSO_4 \cdot 7\,H_2O$	29.5 g/100 mL	25 ^{o}C		2
		22.98 g/100 mL	25 ^{o}C		3
		54.58 g/100 mL	56.6 ^{o}C		3
Rozenite	$FeSO_4 \cdot 4\,H_2O$	35.48-55.02 g/100 mL	60 ^{o}C		3
Lead(II) chloride	$PbCl_2$	1.08 g/100 mL	25 ^{o}C		2
Sphalerite	ZnS	125 g/100 mL	25 ^{o}C		2

Table 2.7: The solubility of minerals present in Zimapán, Mexico, geological system or similar for comparison. Solubility is directly correlated with bioavailability and transport of contaminants. 1. Drahota and Filippi (2009) 2. CRC (2007) 3. Cameron (1929)

The secondary sulfates formed in the Zimapán mining district were similar to sites in the United States. The abundance of pyrite and pyrrhotite in the Eastern US can oxidize to form iron oxides and precipitate soluble sulfates, such processes were shown by Hammarstrom et al. (2005). This study can be used for a multinational AMD reference and help advocate for better mining and remediation practices.

Mineral phase identification of similar samples in the area by Armienta et al. (2012) showed they had similar and different phases identified. Some of their samples had tetrahedrite-tennantite ($Cu_6[Cu_4(Fe,Zn)_2]As_4S_{13}$), anglesite ($PbSO_4$), and wollastonite ($CaSiO_3$), but none were identified in this study. Similar to this study, Armienta et al. (2012) reported arsenopyrite, pyrrhotite, biotite, calcite, galena, goethite, gypsum, quartz, jarosite, diopside, and plumbojarosite. Their model also showed the potential to have Ni and Cu (bi)carbonate species present. It was possible these kinds of species existed off-site, in limestone-rich area close enough to receive AMD, although no samples were collected off-site. Finally, a portion of metals reported and their mobility were Cd, Zn, Cu, Ni, As > Pb, Fe > Cr. There was an abundance of iron oxides and their association with heavy metals helped limit their mobility. Plumbojarosite and scorodite were both found abundantly. The piles of tailings usually had great heterogeneity, but some locations had near pure mineralogy.

In this area, modeling by Armienta et al. (2001) found the dissolution of scorodite and oxidation of arsenopyrite to be the reason behind natural arsenic contamination. The current study and Armienta et al. (2008) both concur that arsenic availability is dependent on pH and soil texture.

The mine tailings and river sediment of the Toliman River, South of Zimapán, Mexico are good study sites and models for anthropogenic environmental impacts, land management, risk assessment, contaminant transport, bioavailability, aged geo-

chemistry, harsh environment mineralogy, and insight for reclamation prerequisites. The heaps of tailings contained an abundance of stable secondary minerals that contain heavy metals, but still pose a risk due to the large surface area of bare, uncovered tailings. In addition, there are still considerable amounts of unoxidized material capable of producing more AMD. There were enough contaminants in the tailings to leach for years to come. The land will probably not be remediated until mining operations are completely halted, or until its not economically feasible to extract additional metals from once-processed tailings, and/or there is no more room to add more tailings on existing properties.

Acid mine drainage may likely always be a burden in Zimapán, Mexico, but it can better limited and prepared for today. Knowing what contaminants are present if beneficial towards the battle against AMD. Since mining will not cease in the near future, treating of the tailings is an unlikely solution. The next option may be proper land management to contain, control, and limit AMD. Systematic sampling of soil and water for contaminants that would affect human health would also help local residents. Prompt response and communication to local people the existence of contamination and its risk is also important for human health.

2.5 Conclusions

The unoxidized samples had the largest amounts of primary minerals such as pyrite, sphalerite, pyrrhotite. Pyrrhotite also exhibited mild magnetism. Secondary minerals were present such as jarosite and goethite. There were also lepidolite, magnetite, orthoclase, gypsum, and quartz. The sample that underwent the least amount of oxidation had a pH of 7.2, similar to the river sediments collected. There was a moderate amount of Ca around 14 percent, and high amounts of Zn, As, and Pb.

There were sporadic soluble sulfates located around the tailings piles where AMD evaporated. The major components were melanterite, rozenite, and boyleite. In addition, trace amounts of pyrite, gypsum, and quartz. These are the most vulnerable to weathering due to their solubility, but will persist due to the tailing's reservoir of unoxidized sulfides. Re-hydrated, the average pH of soluble sulfates was 3.65. The high amount of Zn was found in the soluble sulfates, from 30,878 mg/kg to 465,104 mg/kg of Zn.

The oxidized tailings had the largest amount of jarosite, copiapite, and scorodite. There was also galena, sanidine, smithsonite, sphalerite, augite, pyrite, gypsum, and quartz. The average pH of samples in this category was 3.54.

The river sediment samples contained the highest amount of clay size minerals such as smectite and vermiculite. There was jarosite, kaolinite, illite, albite, calcite, anorthite, and quartz in the river sediment adjacent to the oxidized tailings. The average pH of the river samples was 7.5, while the sample farthest from tailings was 8.0. All the river sediments had around 9 percent Al, while the majority of others had less than 1 percent Al. Sediments near the tailings had noticeably more Cu, Zn, As, Zn, and Pb than the sediment that was not near any tailings. There was also about 5 percent less Fe in the sediment away from tailings, but more Mg, Sr, and K. The heavy metals within tailing runoff does reach nearby running water sources.

The largest amount of arsenic incorporated minerals was found after oxidation. The average pH of the oxidized samples was 3.54. The oxidized sample Zim-PR-2-Gray-2 had the most at 110,000 mg/kg As, a nearly pure scorodite phase. The highest amount of Pb in the oxidized sample, Zim-PR-2-Yellow-2, had 18,000 mg/kg Pb, indicated the incorporation of Pb by jarosite. The majority of these oxidized samples had over 20 percent Fe, but varying amounts of S of 3.02 - 20.06 percent. Nearly all samples contained high concentrations of Cu, Zn, As, and Pb. The unoxidized

samples did not have the highest levels of As, Pb, or Zn, but they did not have low or safe levels either. The highest concentration of Cu was found in soluble sulfates, notably, sample SMV-4, which contained 6,854 mg/kg Cu. The soluble sulfates also contained the highest concentrations of Zn. Sample SMV-4 had the highest amount of Zn at 465,104 mg/kg.

There was evidence of iron oxide formation and metal incorporation in colloids seen during SEM and TEM analysis. Goethite and scorodite were identified to form at a small scale with progressively better crystalline structures.

Pyrite was still present in the samples, even in the oxidized tailings, indicating it was protected by iron oxides from further oxidation. It is also a continuous supply for acidity that favors arsenic mobility. Yet the potential to mobilize arsenic is present but curbed by the presence of iron oxides and sulfates, notably jarosite. The strong point source of contaminants coming from mine tailings is reason enough for environmental concern.

3. ARSENIC SPECIATION AND GEOCHEMICAL PROCESSES AFFECTED BY CARBONATES IN ZIMAPÁN, MEXICO

3.1 Introduction

Zimapán, Mexico is a small town located in Western Hidalgo state with a mining heritage that goes back hundreds of years and still continues today. The semi-arid mining region is known for its Cu, Zn, and Pb mining. Both urban and countryside landscapes have been affected by the mining industry. Large tailing piles can be found in and out of the city limits of Zimapán.

The long history of mining in Hidalgo offers researchers a chance to compare minimal and highly weathered tailing mineralogy. The processed tailings were previously reported to be highly contaminated with heavy metals such as As, Pb, Cu, and Zn. Also, the region has natural and anthropogenic sources of arsenic found in water supplies.

The observed pathways of metals for absorption, release, and re-incorporation during crystallization can help define better parameters and explanations for molecular modeling and contaminant transport. This region is unique because of its semi-arid climate in a carbonate-rich geological environment. In addition, these heterogeneous iron- and arsenic-rich tailings samples made them good candidates for sub-micron microscopy and synchrotron micro-probe research. There is a lack of synchrotron generated data from tailing mineralogy in this geochemical environment.

Minerals in the Zimapán system that can be grouped together based off their genesis 1) quartz, 2) pyrite, arsenopyrite, 3) pyrrhotite, chalcopyrite, 4) certain carbonates, sphalerite, galena, and 5) other carbonates (Augustithis, 1995). Paragenesis of minerals from different hydrothermal deposits were categorized into groups and

ordered earliest to latest listed left to right. In general, the order follows the free energies of formation of the oxides and sulfides of the metal. The greater the free energy, the earlier the formation. 1) Magnetite, ilmenite, haematite, 2) pyrrhotite, arsenopyrite, pyrite, nickel arsenides, 3) chalcopyrite, sphalerite, 4) galena, lead sulfosalts (Augustithis, 1995).

The oxidation zone of mines can be thin but vary greatly in mineralogy with the creation of secondary minerals, such as, but not limited to: goethite, scorodite, azurite, malachite, halotrichite, copiapite, arsenosiderite, olivenite, chalcophyllite, and tyrolite (Augustithis, 1995).

3.2 Geochemical Processes Controlling Distribution and Fate of As in Zimapán, Mexico

The mine tailings in the Zimapán region are located in and around the populace, putting the residents' health at risk. Tailings in the Zimapán region are near water sources and possess the potential of being a means of transport for contaminants. Ranjan et al. (2012) found that the area's water contained organic species monomethylarsonous acid (MMA), dimethylarsinous acid (DMA), and trimethylarsine (TMA), and inorganic species of As(III) as AsO_3^{-3}, and As(V) as AsO_4^{-3}. The methylated species were found in greater concentrations in pore-space water of sediment rather than in free water. In free water, As(V) was the majority with minimal MMA. However, in the pore-space of sediment water As(III) held the majority and had all the methylated forms: MMA, DMA, and TMA . This was attributed to free water having aerobic conditions so As(V) was more stable, or because of As(V) having a strong affinity to microbial activity or other constituents in water. The lack of methylated species indicated the lack of microbial activity under aerobic conditions. However, in sediment pore-space water, anaerobic conditions persist and so

does microbial activity, which is favorable for As(V) to As(III) transformations. As depth increases, anaerobic conditions increase, microbial activity increase, and as such, reduction of As(V) into As(III) increase. But As(V) is also more absorbed to iron oxides which are insoluble, also showing As(III) absorbs less to iron oxides than As(V) (Ranjan et al., 2012).

As(V) bound to Fe- and Al-oxides, is always a risk to release arsenic because of their susceptibility to pH changes. As(V) reduction occurs before the Fe(III) reduction, so the Fe(III) reduction did not enhance As release (Zhang et al., 2012), but the release of As(III) was increased when Al-oxides (i.e. gibbsite) were incorporated.

The most common way to neutralize mine waste with AMD is to add limestone or other carbonate compounds. Even though acidity is battled with carbonates, the pH can only rise so high if using only carbonates. Calcite has a maximum neutralizing pH of 6.4 due to pH buffering by CO_2 during AMD neutralization (Zvimba et al., 2012). The pH can increase further with the addition of different alkaline mineral species. Also, during immobilization reactions, calcite is a proton sink. The rate of the reaction is related to the surface area of the calcite. Ferrous salts favor forming lepidocrocite and goethite, and ferric salts favor ferrihydrite. Generally, the faster the process, the less crystalline the product is. The rates of dissolution for iron oxides are: ferrihydrite > lepidocrocite $\geq$ magnetite > hematite > goethite. For calcite with $Fe(ClO_4)_2$, the rate of reaction decreased with higher partial pressure of CO_2 and decreasing partial pressure of O_2. The reduced rate of reaction is attributed to the reduced rate of oxidation of Fe^{2+} at greater P_{CO_2}.

Due to how the tailing piles in Zimapán are created, their age is slightly ambiguous. Although piles are estimated to be up to 60 years old, not all are deposited after a single processing. The piles of tailings were added to over time, gradually obtaining more waste. After processing, the waste is diluted into a slurry and pumped onto

a pile for its final destination. In addition, the ores from multiple mines are sent to the processing plant, which add even more ambiguity to their initial geological source and any correlations of adjacent solid phases in the tailings. Because of this, the ages of the minerals can vary within each pile and the mineral's origin cannot be determined.

Arsenic chemical species are sensitive to redox conditions allowing them to occur in several different valence forms (e.g., -1, 0, +3, +5). These different species can occur as crystal structural ions, be adsorbed on surfaces, or be incorporated into cages of framework minerals, such as schwertmannite. Synchrotron bulk and micro-scale X-ray absorption spectroscopy are unique tools that can be used to determine the chemical state and local atomic coordination of low-concentration elements in such poorly crystalline systems.

The objectives of this study were to 1) identify mineral phases containing As in mine tailings, 2) characterize As speciation in each associated solid phase using a synchrotron light source, and 3) identify the geochemical processes affected by the carbonate-rich environment.

3.3 Materials and Methods

The six samples used for this study were labeled 4M, 4L, 4D, 4K, 4E, and 8E (Table 3.1) were collected at the San Francisco Mine about 12 kilometers north of Zimapán, Mexico in Hidalgo state (Figures 3.1 and 3.2). Samples were collected and initially analyzed by McClure (2012). The samples 4M and 4L were red and showed the greatest signs of oxidation. Samples 4D, 4K, and 4E were gray and showed the least amount of oxidation. The final sample 8E, was a soluble yellow precipitate collected downstream of AMD released from the tailings.

Sample ID	Mine	Description	GPS Coordinates	
			Latitude	Longitude
Oxidized Tailings				
4M	San Francisco Mine	Red	N 20° 49.303′	W 99° 22.378′
4L	San Francisco Mine	Red	N 20° 49.303′	W 99° 22.378′
Unoxidized Tailings				
4E	San Francisco Mine	Grey	N 20° 49′ 16.56”	W 99° 22′ 28.56”
4D	San Francisco Mine	Grey	N 20° 49′ 17.46”	W 99° 22′ 26.76”
4K	San Francisco Mine	Grey	N 20° 49′ 13.98”	W 99° 22′ 32.76”
Soluble				
8E	San Francisco Mine	Yellow	N 20° 49.601′	W 99° 22.421′

Table 3.1: List of samples collected and analyzed from Zimapán, Mexico, and their location coordinates.

Figure 3.1: The location of San Francisco Mine tailings are not far north of Zimapán city limits.

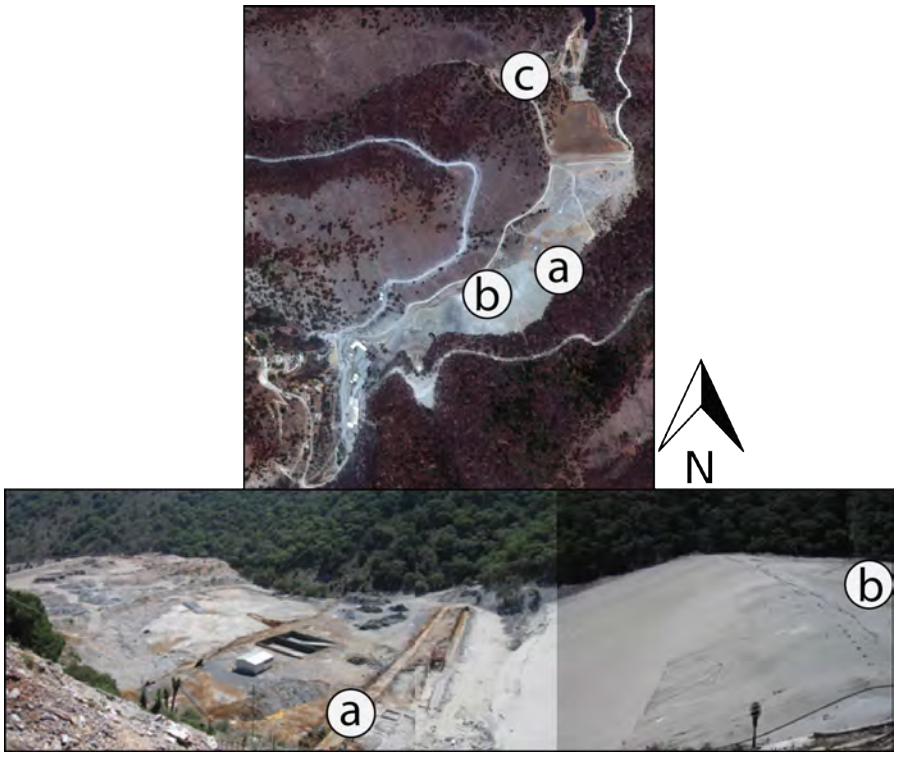

Figure 3.2: The original location of the four samples used in this study from San Franciso is shown above. a = 4M, 4L; b = 4E, 4D, 4K; and c = 8E.

Bulk and micro-beam X-ray absorption spectroscopy (XAS) including X-ray absorption near edge structure (XANES) and Extended X-ray absorption fine structure (EXAFS) analyses were conducted at the Advanced Photon Source (APS) through the General User Proposal program. The APS facility was utilized for three days. During this time, sample treatments and mounting protocols were established. A selected set of samples underwent XAS analysis at Argonne National Laboratory in Chicago, Illinois using their APS, and some of the same sample also were examined by XAS at the National Synchrotron Radiation Research Center, Taiwan.

The As-containing particles were located with micro-X-ray fluorescence mapping to determine the site of interest for XANES micro-probe. The valence state of As

was then determined by XANES. The standard used for As(V) at the Chicago APS facility was disodium hydrogen arsenateheptahydrate ($Na_2HAsO_4 \cdot 7H_2O$) and was obtained from Sigma Aldrich. Additional standards were scanned at the in Taiwan at the National Synchrotron Radiation Research Center. In Taiwan, the As(V) and As(III) standards were sodium arsenate and sodium arsenite that was diluted to 1,000 ppm As with cellulose. Scorodite and arsenopyrite were also diluted with cellulose. The XANES experiments in Taiwan used a Lytle detector with a 6 micron germanium filter and a set of Soller slit in fluorescent mode. The energy was calibrated to the L3 edge of Au at 11,919 eV. Linear combination with least-square fitting (LC-LSF) determined the abundance of As species present in samples that underwent XAS analysis. Values can slightly differ as they change every time the calculation is ran in Athena software.

To reveal the different chemical environment of the adsorbed/incorporated As in the various host minerals or amorphous phase, the silt fraction of sample 4L underwent selective dissolution by pH 3 ammonium oxalate in darkness and DCB treatments to remove oxides and jarosite. Ferric iron was reduced by sodium dithionite to ferrous iron, allowing oxidized material in the solution to become more soluble. Sodium citrate complexes with Fe, acting as a chelate to promote dissolution of iron oxides.

The mineral composition of the bulk sample and the sand, silt, clay fractions of each sample were analyzed on a Bruker D8 Advance X-ray diffractometer (XRD) using Cu Kα radiation, 35 kV, 45 mA, 5 seconds dwell time at each step, 0.05^o step size, and Sol-X energy-dispersive detector. The powder samples were front-loaded into plastic sample holders and the clay fraction suspensions were dried as thin films on a glass or zero-background quartz slide. Most samples were scanned from 2^o to 70^o 2θ, except the clay fractions, which were scanned from 2^o to 33^o 2θ.

The clay fraction of most samples underwent saturation treatments to assist identification of clay minerals. A portion of the clay fractions were separately saturated with Mg^{2+} (0.5M $MgCl_2$) and K^+ (1M KCl) solutions. After three washes of solution and one of DI water, a few drops were dried onto XRD slides for analysis. After analysis, the Mg^{2+} saturated clay slide was solvated with glycerol with an aerosol spray-can applicator, then air dried. In addition, the K^+ saturated slide was heated to 330 ^{o}C and 550 ^{o}C for XRD analysis at each temperature increment (Deng et al., 2012).

The chemical composition of selected samples were conducted at the Mineral Lab using x-ray fluorescence (XRF). The XRF spectrometer consisted of a Phillips simultaneous, wavelength dispersive unit equipped with 26 fixed detectors, 2 scanning detectors, and a Rh end-window tube.

Transmission electron microscopy (TEM) analysis was performed on a FEI TECNAI G2 F20 ST FE-TEM. Scanning electron microscopy (SEM) FEI QUANTA 600 FE-SEM. The TEM and SEM analyses were conducted at the Texas A&M University Microscopy and Imaging Center. Unless where noted, additional electron microscopy analysis was conducted by Dr. Toshihiro Kogure in Japan.

Fourier transform infrared (FTIR) analysis was conducted on a PerkinElmer Spectrum 100. FTIR patterns were recorded using an attenuated total reflectance (ATR) accessory with a total of 32 scans for each sample and a resolution of 2 cm^{-1}.

3.4 Results

3.4.1 Mineralogical Determination

Mineralogical phases were determined and separated into three categories based off their degree of weathering to help analysis and comparison with one another. The samples were separated into oxidized, unoxidized, and soluble tailings. Each

underwent numerous XRD and FTIR analysis to determine mineralogical phases present.

3.4.1.1 Oxidized samples: 4M and 4L

Initial processes included the identification of mineral phases present in mine tailings (McClure, 2012). The two samples 4M and 4L were reddish-yellow with pH 3.5 and pH 4.2 respectively, indicating oxidation has occurred to some degree.

The X-ray diffraction patterns of the unfractionated samples showed the presence of gypsum (Figures 3.3 and 3.4). The sand and silt fractions of both oxidized samples were dominated by quartz, feldspar, and jarosite. The sharp peak at 2.71 Å peak in sample 4L was attributed to pyrite, indicating the presence of unoxidized pyrite. The same peak for pyrite was not present in sample 4M.

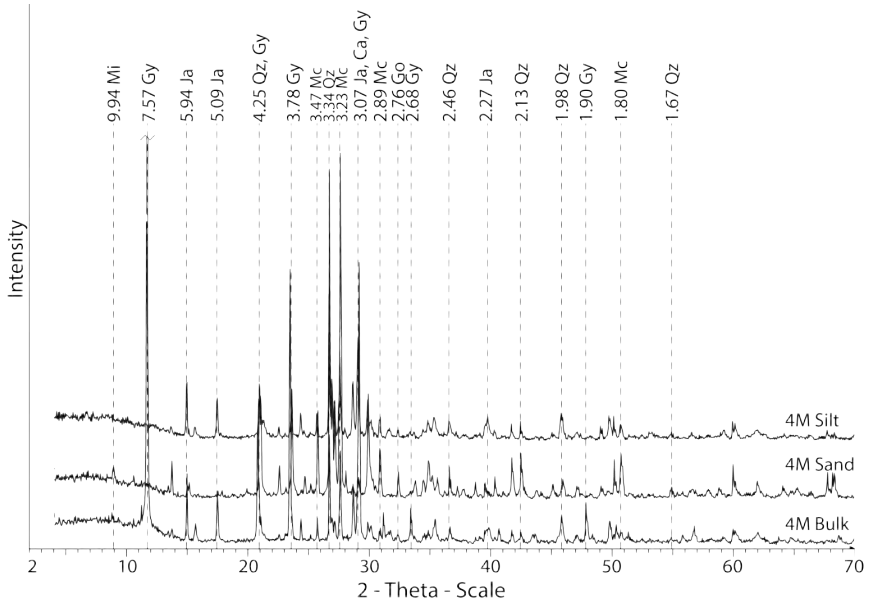

Figure 3.3: Sample 4M size fractions: silt, sand, and bulk. Mi = Mica, Go = Goethite, Mc = Microcline, Gy = Gypsum, Ja = Jaorsite, Ca = Calcite, Qz = Quartz.

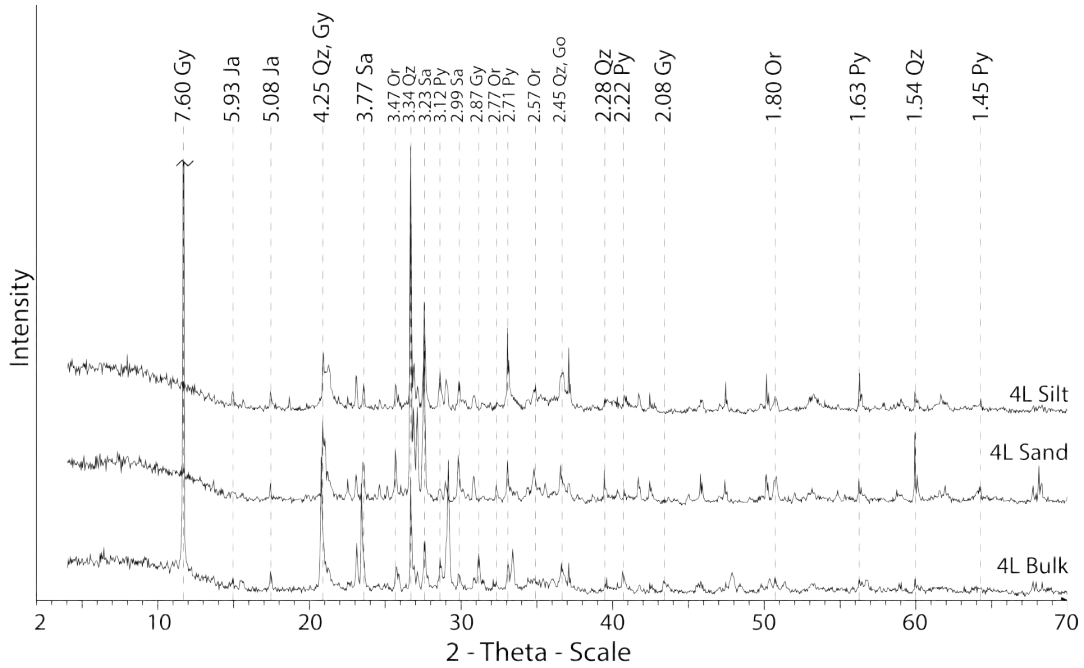

Figure 3.4: Sample 4L size fractions: silt, sand, and bulk. Gy = Gypsum, Or = Orthoclase, Py = Pyrite, Sa = Sanidine, Go = Goethite, Ja = Jarosite, Qz = Quartz.

The samples 4M and 4L silt fractions both underwent SEM and TEM analysis (Figures 3.5, 3.6, and 3.7). Electron microscopy gave further evidence of 4M containing jarosite, quartz, diopside, mica, and iron oxides. The EDS chemical analysis showed the presence of As in some iron oxide particles and also in jarosite. Weak peaks due to Zn were also observed in other iron oxide particles (Figure 3.5).

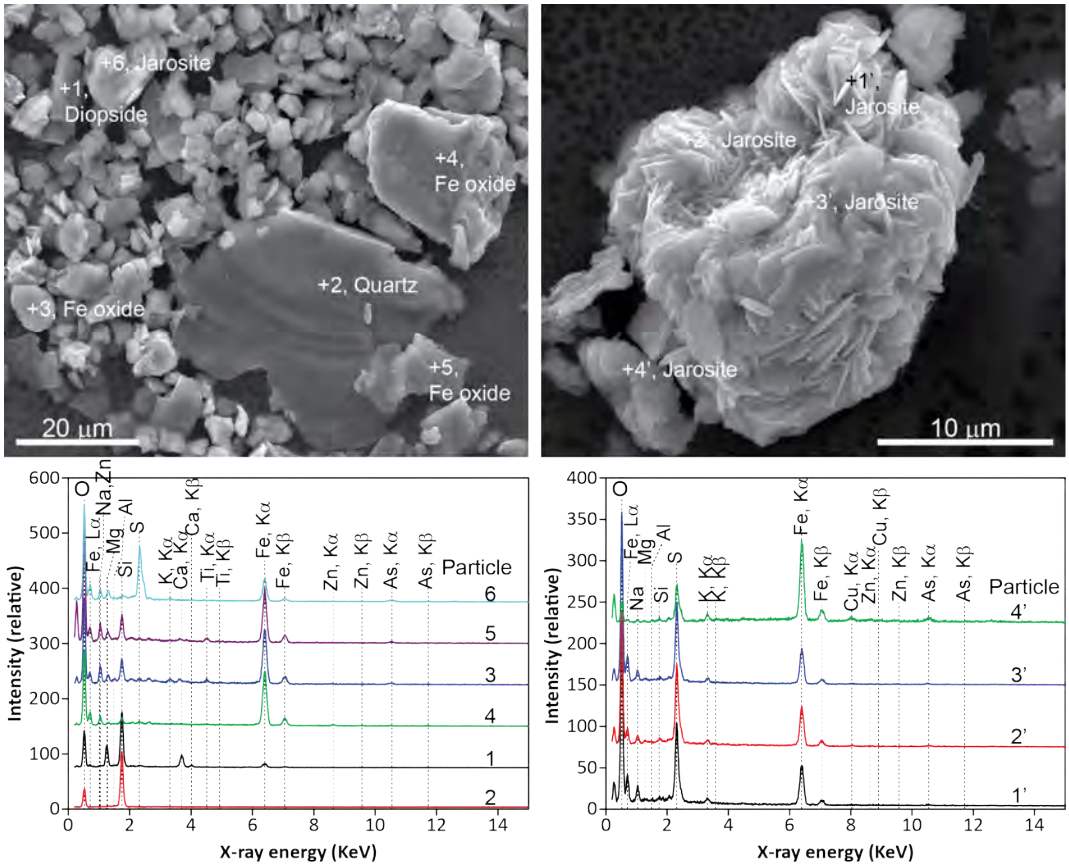

Figure 3.5: SEM of particles from sample 4M. There was evidence of jarosite, quartz, diopside, and iron oxides.

Biotite particles were observed in the TEM images of the silt fraction of sample 4M. As indicated by the EDS spectra, As was observed in the jarosite particles. Particles 2 and 4 contained abundant Pb, but less K were identified as plumbojarosite (Figure 3.6); in particle 3, As and Zn were evident in an amorphous iron oxide.

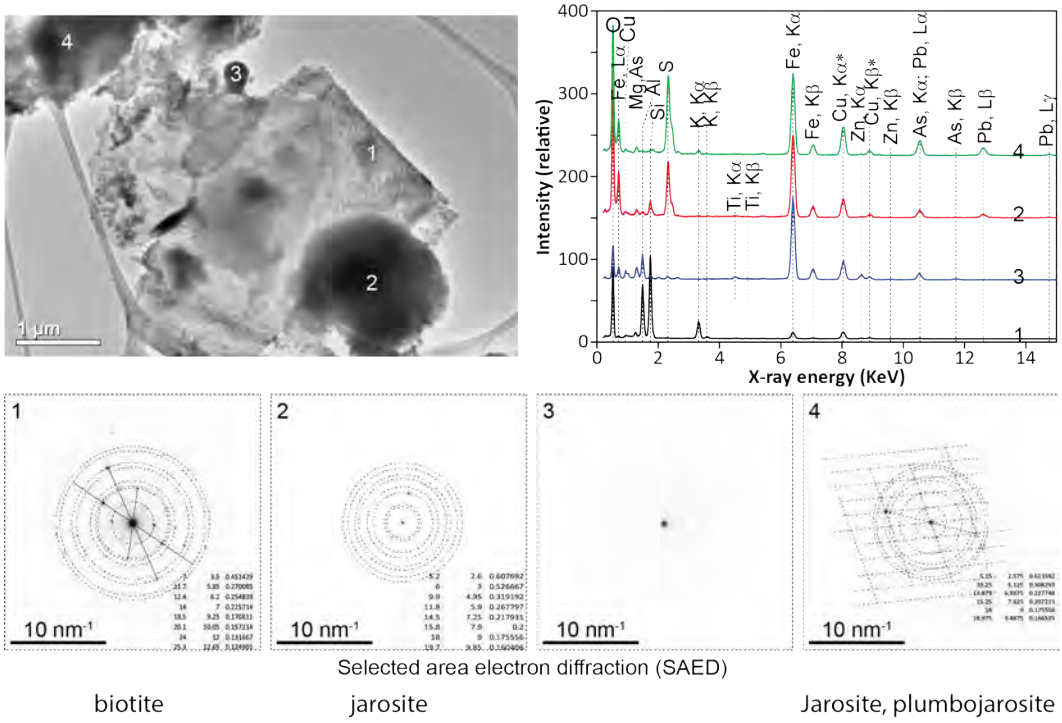

Figure 3.6: TEM of sample 4M containing a mica, jarosite, and plumbojarosite.

The SEM analysis of sample 4L confirmed that pyrite and chalcopyrite remained in this highly oxidized sample. An aggregate of jarosite particles showed traces of of As, Cu, or Zn compared to a typical jarosite, the jarosite aggregates in 4L had much less K, as indicated by the EDS spectra (Figure 3.7).

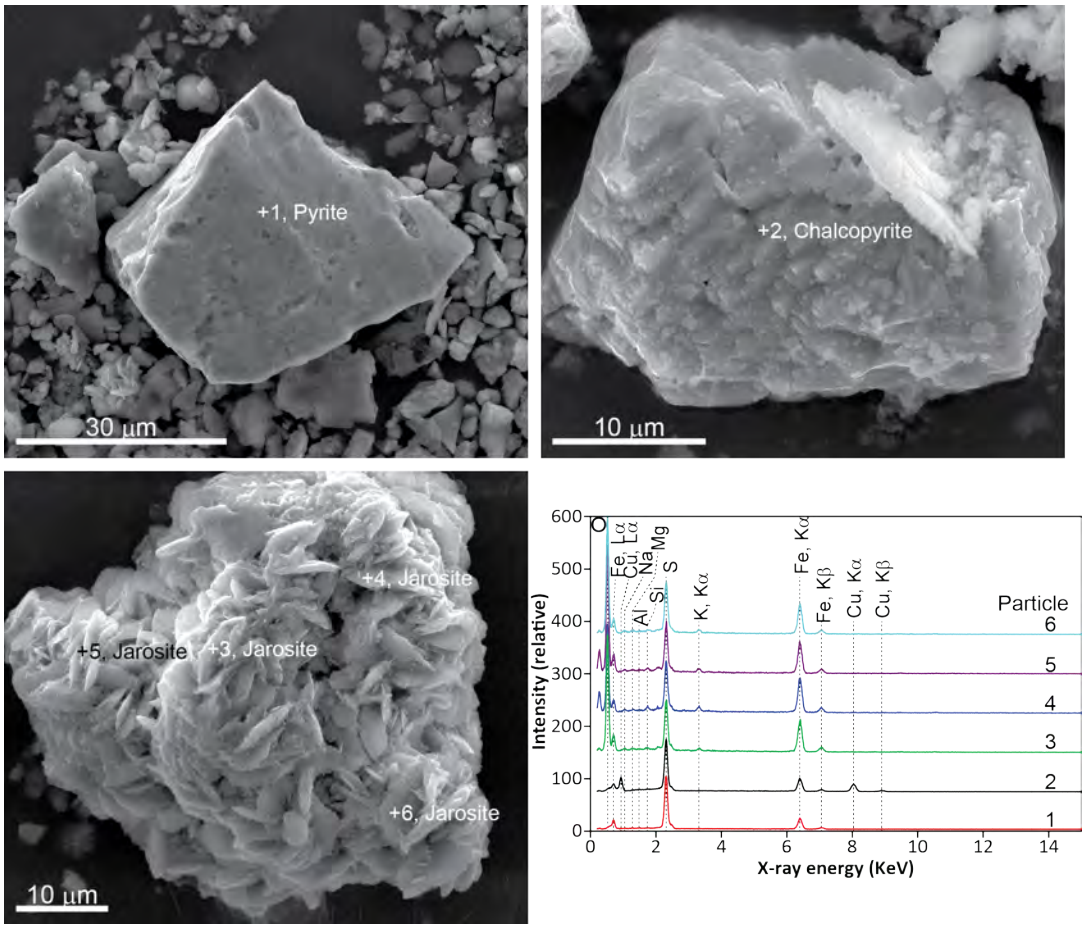

Figure 3.7: SEM analysis of three particles from sample 4L. The particles consisted of pyrite, chalcopyrite, and jarosite.

Jarosite was the dominant mineral in both clay fractions of samples 4M and 4L (Figure 3.8). The broad peak at 4.18 Å was attributed to goethite. Mica was confirmed by the presence of the 10.03 and 3.33 Å peaks. Sample 4L had a sharp peak at 3.85 Å that was identified as elemental sulphur. No smectite, vermiculite, or kaolinite were observed in the clay fractions of 4M or 4L. Lepidocrocite and elemental sulfur were identified in 4L (Figure 3.9).

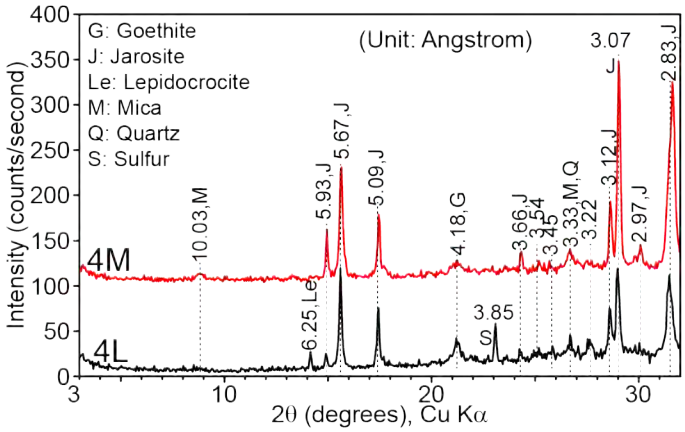

Figure 3.8: XRD of clay fractions of samples 4M and 4L. Both had an abundance of jarosite, goethite, mica, and quartz.

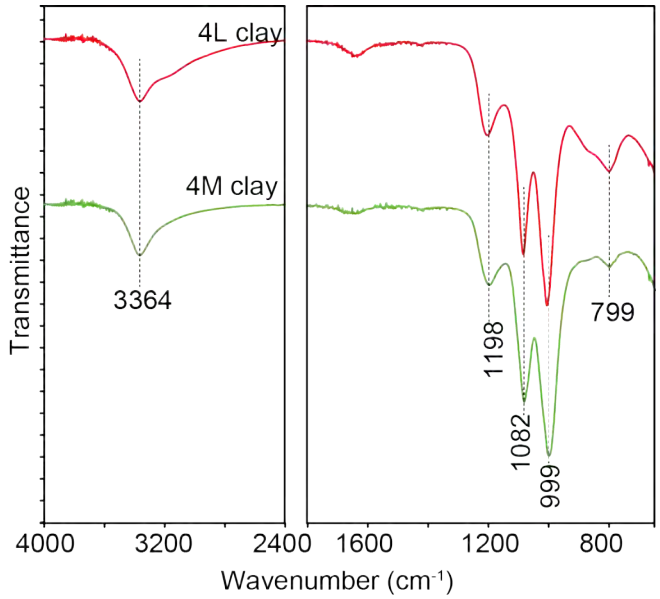

Figure 3.9: FTIR of clay fractions of samples 4M and 4L. The spectra has peaks for jarosite at 3364 cm $^{-1}$ (-OH) and 1198 - 799 cm $^{-1}$ (-SO_4).

The FTIR spectra (Figure 3.9) indicated that the -OH bands occurred at 3364 cm $^{-1}$ which is lower than the 3384 cm $^{-1}$ of a k -jarosite, but close the to the 3367 cm $^{-1}$ of Na- or 3353 cm $^{-1}$ of H_3O^+ - jarosite.

The infrared band positions suggested that the jaorsite in the oxidized tailing sample's solid solutions of K, Na^+, H_3O^+, and possibly Pb^{2+}.

The TEM analysis of the clay fraction of samples 4M and 4L revealed poorly crystalline iron oxides containing Cu and As (Figure 3.10).

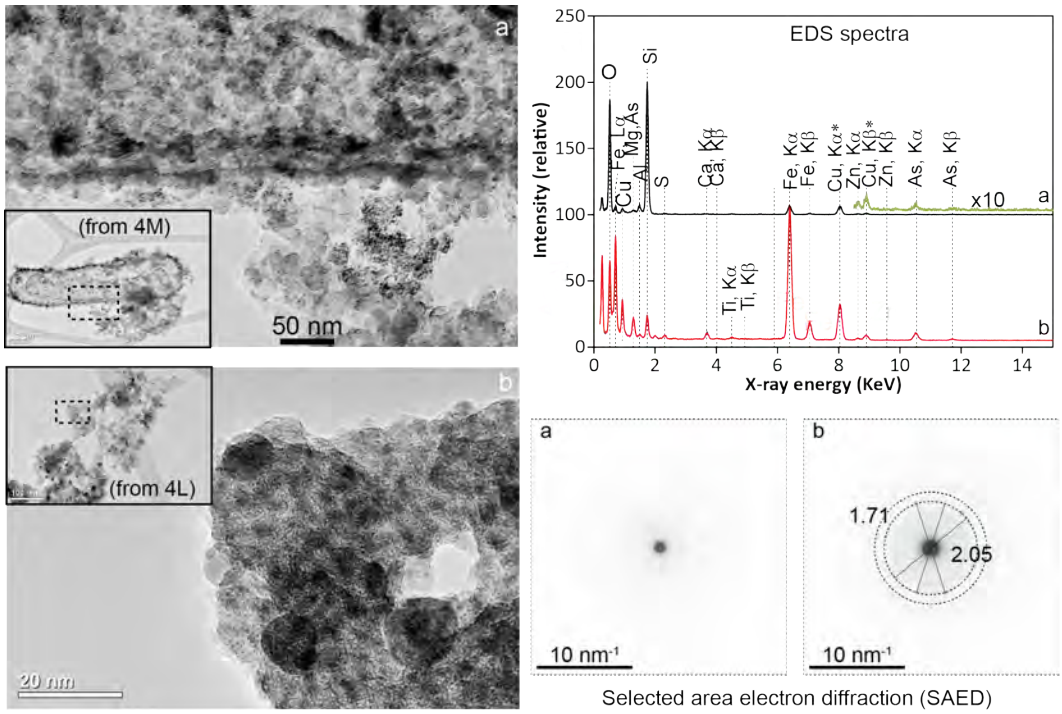

Figure 3.10: TEM of nanoparticles from samples 4M and 4L. Both samples contained iron oxides containing Cu and As. Particle (a) is amorphous silica and particle (b) is poorly crystalline iron oxides.

In the TEM images of sample 4L, an aggregate showed the presence of iron oxides and jarosite with As. A high resolution TEM image of the aggregate showed the presence of fringes of 0.5 nm that corresponded to the (020) reflection for goethite (Figure 3.11).

Nanometer sized amorphous silica and poorly crystalline iron oxides formed in the oxidized tailings. High concentrations of As was associated with Fe oxides. Trace As and Zn were associated with amorphous silica. The Fe oxides were either amorphous or hematite. The hematite was likely formed due to electron beam heating during the analysis. A goethite and jarosite aggregate was analyzed with high-resolution TEM. Arsenic can be formed on both particles. The goethite showed fringes in a few

nanometer domains, indicating their low crystallinity. With time under the electron beam they converted to hematite.

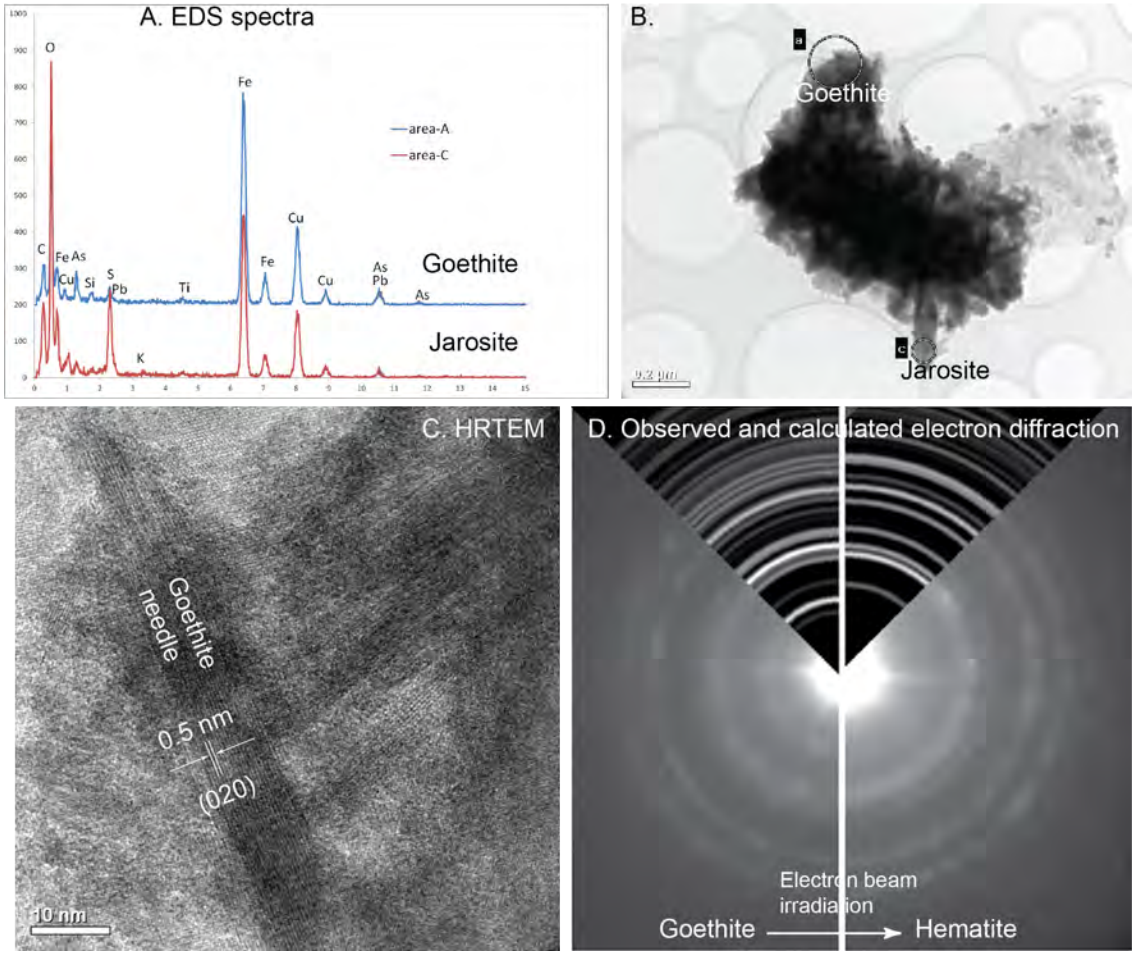

Figure 3.11: TEM analysis of two particles from sample 4L. There was evidence of goethite and jarosite.

The clay fractions of both oxidized samples 4M and 4L underwent saturation and heat treatments to better elucidate trace mineral phases during XRD analysis (Figures 3.12 and 3.13). The xrd patterns were not affected by the mg and mg-glycerol solvation treatments due to the lack of expandable clay minerals. Heating the

clay fraction and 330 ^{o}C significantly reduced the intensity of the jarosite peaks and the peaks disappear at 550 ^{o}C (Figures 3.12 and 3.13). The goethite and lepidocrocite peaks disappeared upon heating and a new peak at 2.71 Å peak was observed in the 550 ^{o}C pattern due to the formation of hematite.

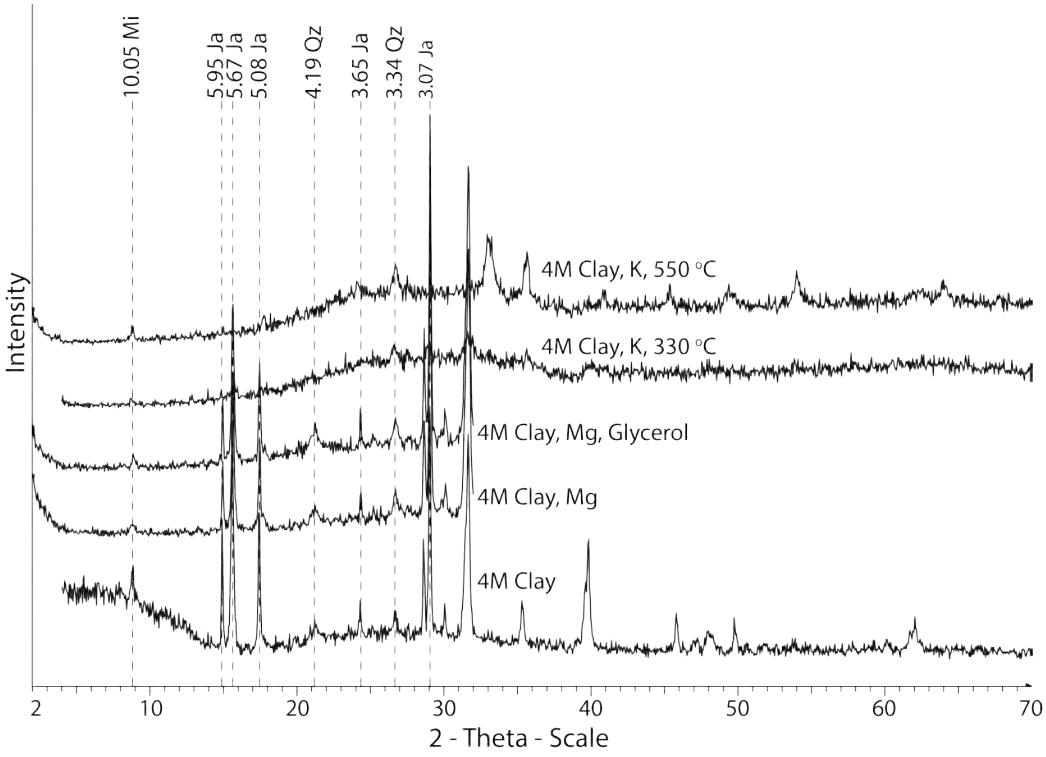

Figure 3.12: Sample 4M clay treatments by heat, cation saturation, and/or glycerol. Mi = Mica, Ja = Jarosite, Qz = Quartz.

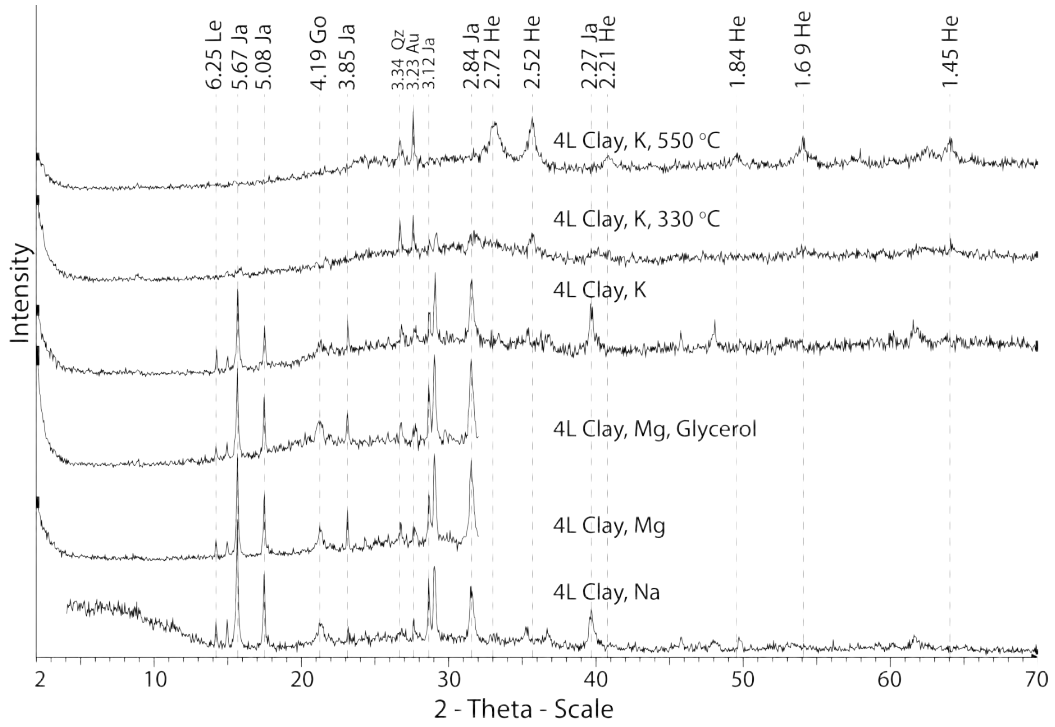

Figure 3.13: Sample 4L clay treatments by heat, cation saturation, and/or glycerol. Ja = Jarosite, Go = Goethite, Au = Augite, Le = Lepidocrocite, He = Hematite, Qz = Quartz.

Next, the clay and silt size fractions were used for a selective dissolution pH 3 ammonium oxalate and DCB treatments of iron for additional characterization with XRD (Figures 3.14, and 3.15, **??**, 3.16, and 3.17) and XAS analysis.

After sample 4M silt had Fe removed, XRD shown resistance from mica, jarosite, microcline, augite, and quarts. Sample 4L after treatments still contained jarosite, sanidine, pyrite and quartz. In both samples after DCB treatment, jarosite peaks were removed or greatly reduced while galena was formed. The mineralogy was similar in the clay fractions with treatments, as well as the absence of jarosite and formation of galena in the DCB treatments. Formation of galena during DCB treatments suggest that the Pb was incorporated in jarosite, then released by the DCB treatment.

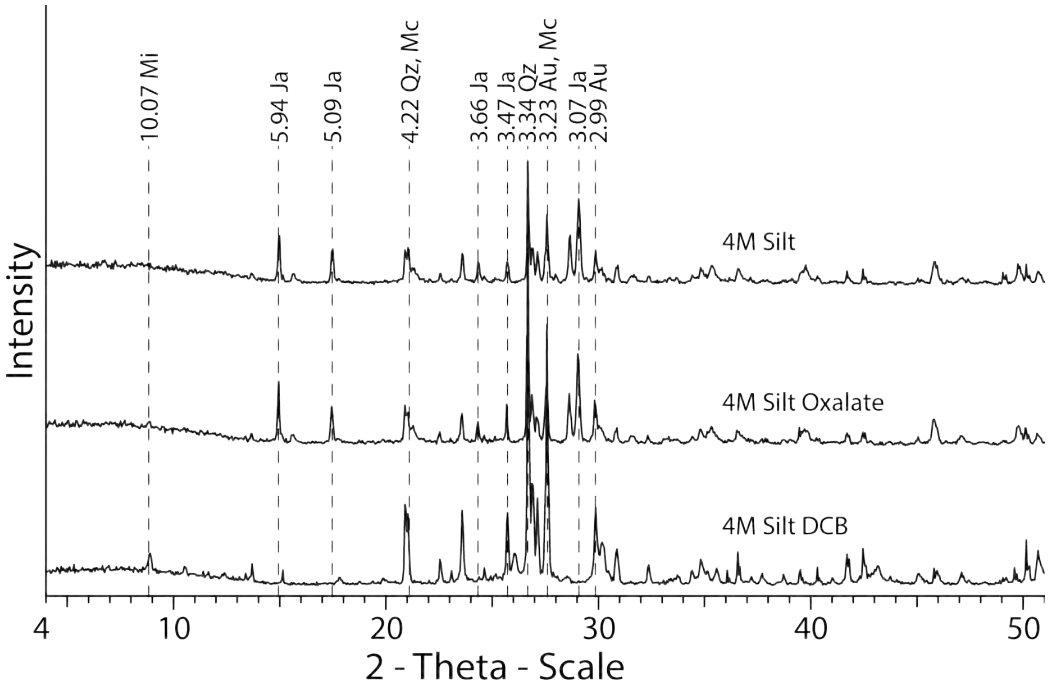

Figure 3.14: Sample 4M silt size fraction underwent selective iron dissolution treatments. Mi = Mica, Ja = Jarosite, Mc = Microcline, Au = Augite, Qz = Quartz.

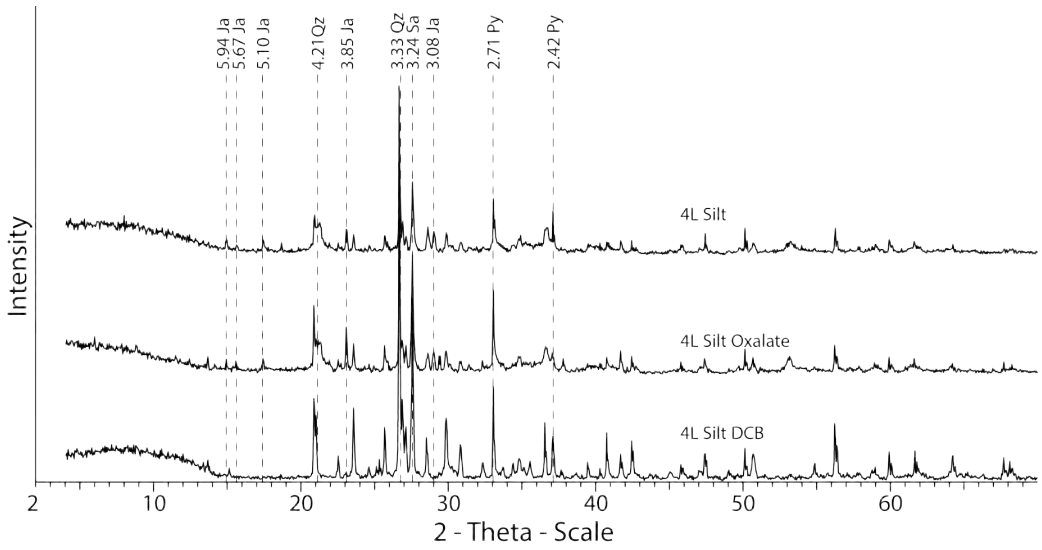

Figure 3.15: Sample 4L silt size fractions that underwent selective iron dissolution treatments of DCB or ammonium oxalate. Ja = Jarosite, Sa = Sanidine, Py = Pyrite, Qz = Quartz.

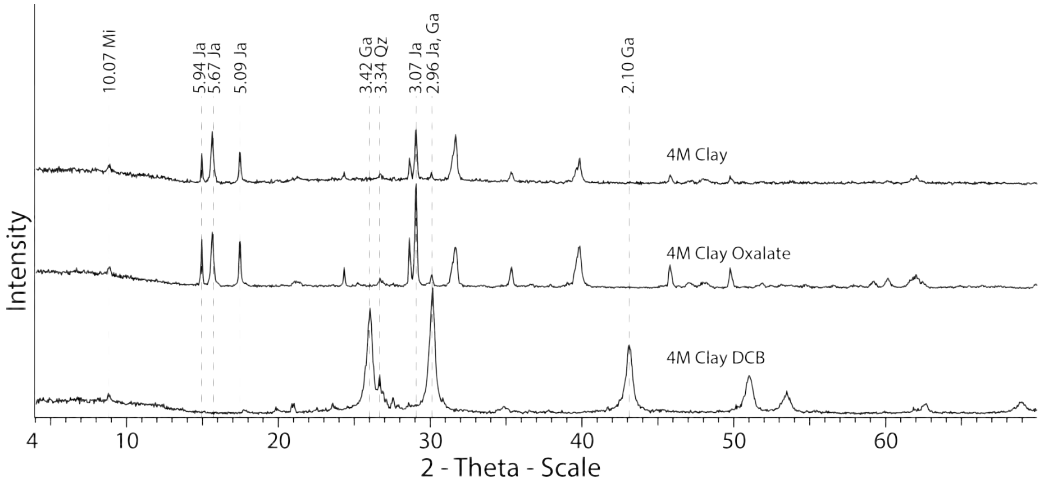

Figure 3.16: Sample 4M clay size fractions that underwent selective iron dissolution treatments of DCB or ammonium oxalate. Mi = Mica, Ja = Jarosite, Sa = Sanidine, Ga = Galena, Qz = Quartz.

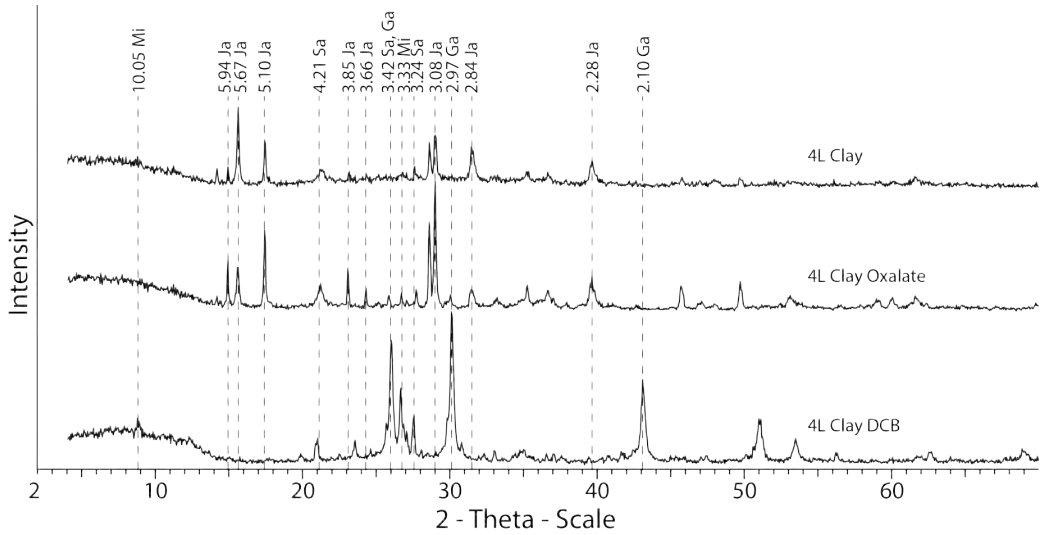

Figure 3.17: Sample 4L clay size fractions that underwent selective iron dissolution treatments of DCB or ammonium oxalate. Mi = Mica, Ja = Jarosite, Sa = Sanidine, Ga = Galena, Qz = Quartz.

3.4.1.2 Unoxidized samples: 4E, 4D, and 4K

Sample 4E had a large phase of magnetic material that was identified as pyrrhotite (Figure 3.18). Sample 4E had signs of mica, hornblende, kaolinite, chlorite, sanidine, pyrite, pyrrhotite, calcite, orthoclase, gypsum, sphalerite, and quartz.

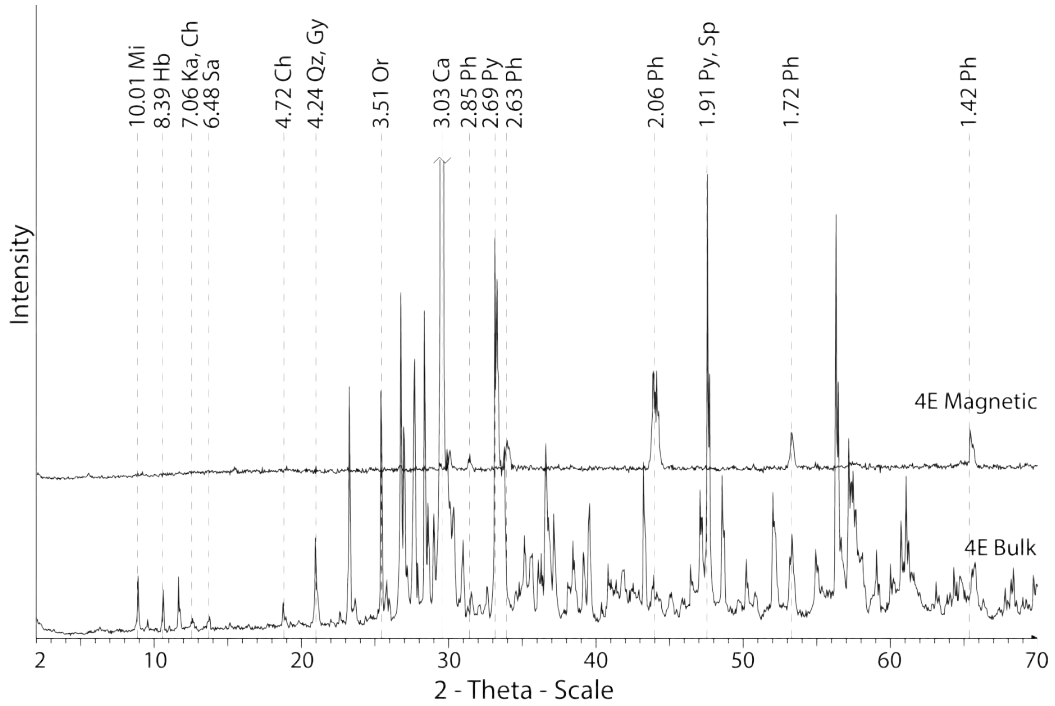

Figure 3.18: Sample 4E bulk and a separated magnetic fraction from a different bulk portion. Mi = Mica, Hb = Hornblende, Ka = Kaolinite, Ch = Chlorite, Sa = Sanidine, Py = Pyrite, Ph = Pyrrhotite, Ca = Calcite, Or = Orthoclase, Gy = Gypsum, Sp = Sphalerite, Qz = Quartz.

In the clay fraction of both 4D and 4K, smectite was identified by the presence of the 18 Å peak on the Mg-glycerol treatment (Figure 3.19). The 15 Å peak in the Mg-glycerol treatment confirmed the presence of vermiculite. The constant peak near 10 Å indicated the presence of mica. The weak peaks at 9.36 Å were attributed to talc. The presence of talc in the unoxidized tailings suggested a low-grade metamorphism in the contact zone when the ore formed.

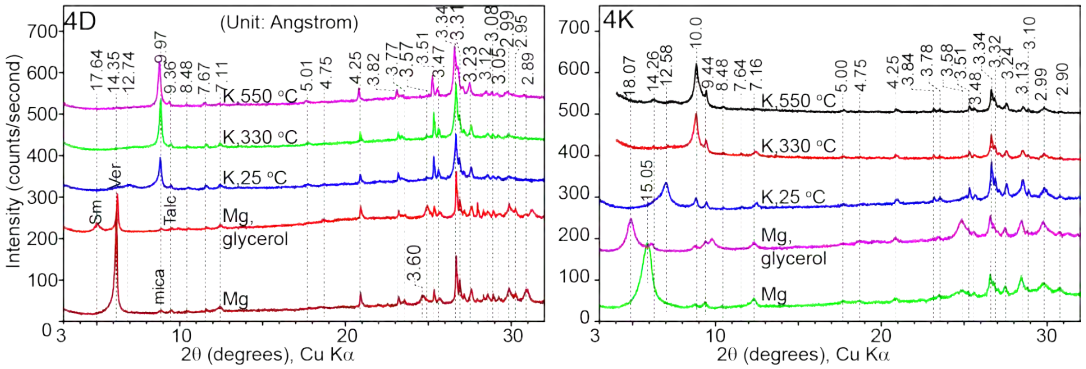

Figure 3.19: XRD of the clay fractions from samples 4D and 4K.

SEM and TEM analysis of sample 4D gave additional confirmation for mineral phases present (Figures 3.20 and 3.21). There were particles of pyrite, arsenopyrite, wollastonite, quartz, feldspar, and vermiculite present. Nanoparticles shown metals incorporation in semi-crystalline phases. Similarly, sample 4K underwent SEM analysis (Figure 3.22). There were particles of pyrite, quartz, feldspar, wollastonite, and diopside present.

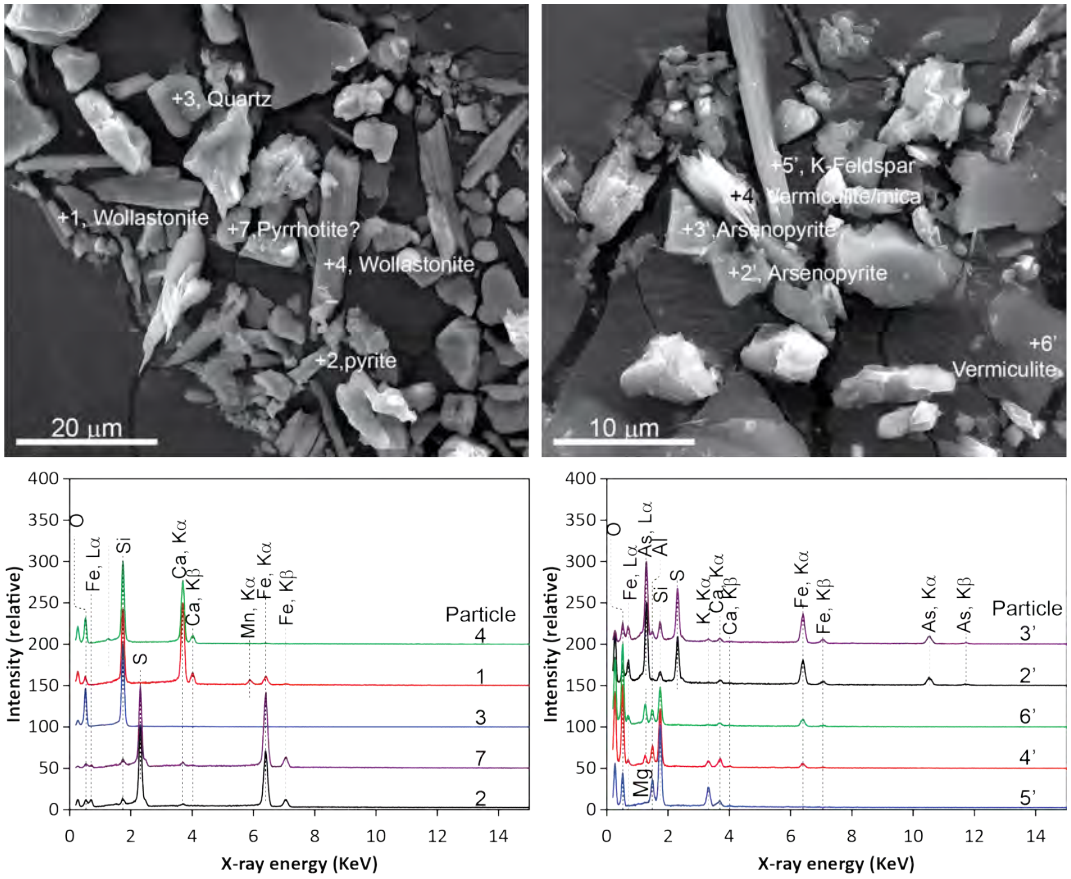

Figure 3.20: SEM analysis of multiple particles from sample 4D. There was evidence of arsenopyrite, pyrite, wollastonite, quartz, feldspar, and vermiculite.

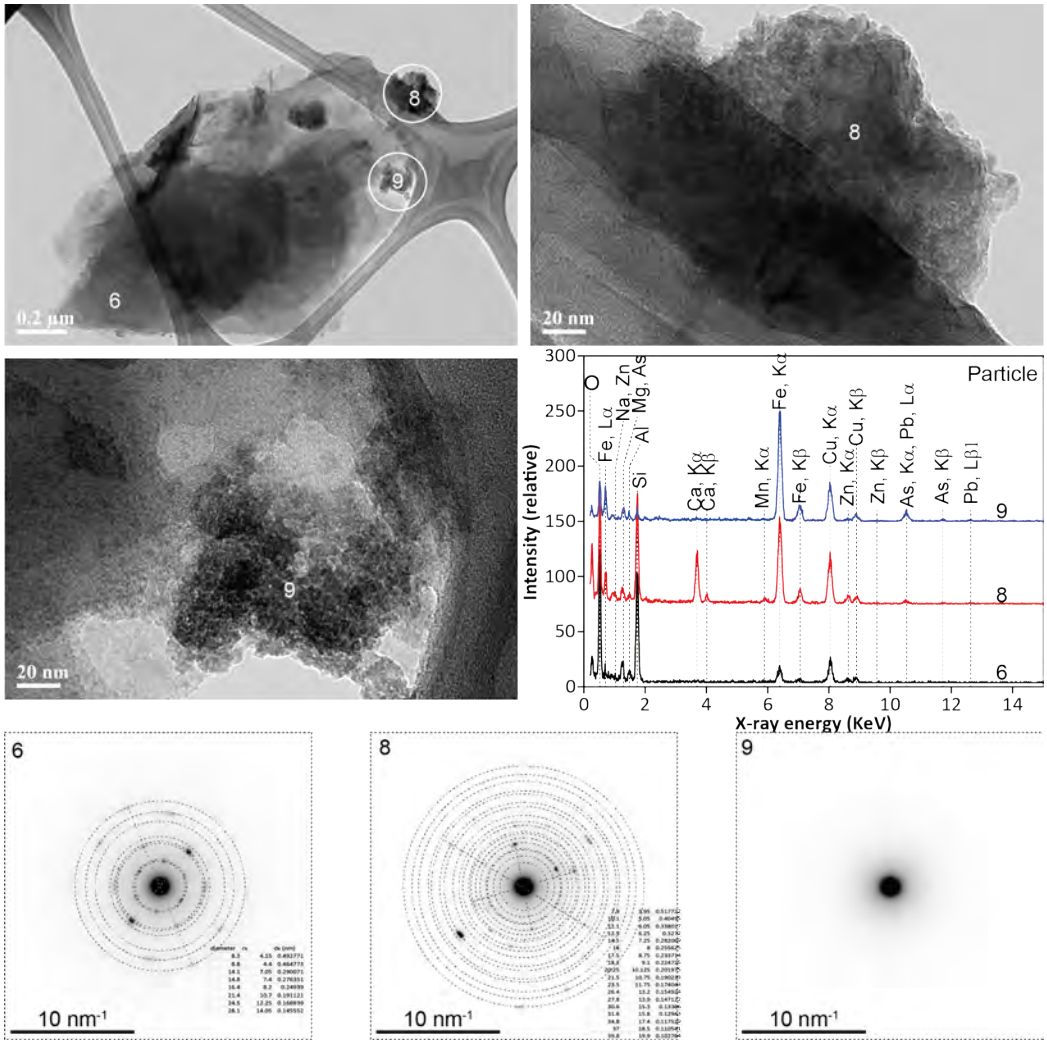

Selected area electron diffraction (SAED)

Figure 3.21: TEM analysis of three particles from sample 4D. Three nanoparticles show evidence of early metal incorporation and semi-crystallization.

The fine particles in the unoxidized tailing materials also showed the formation of amorphous iron oxides (Figure 3.21). Strong EDS peaks of As and Zn indicated that the iron oxides could adsorb or incorporate the heavy metals.

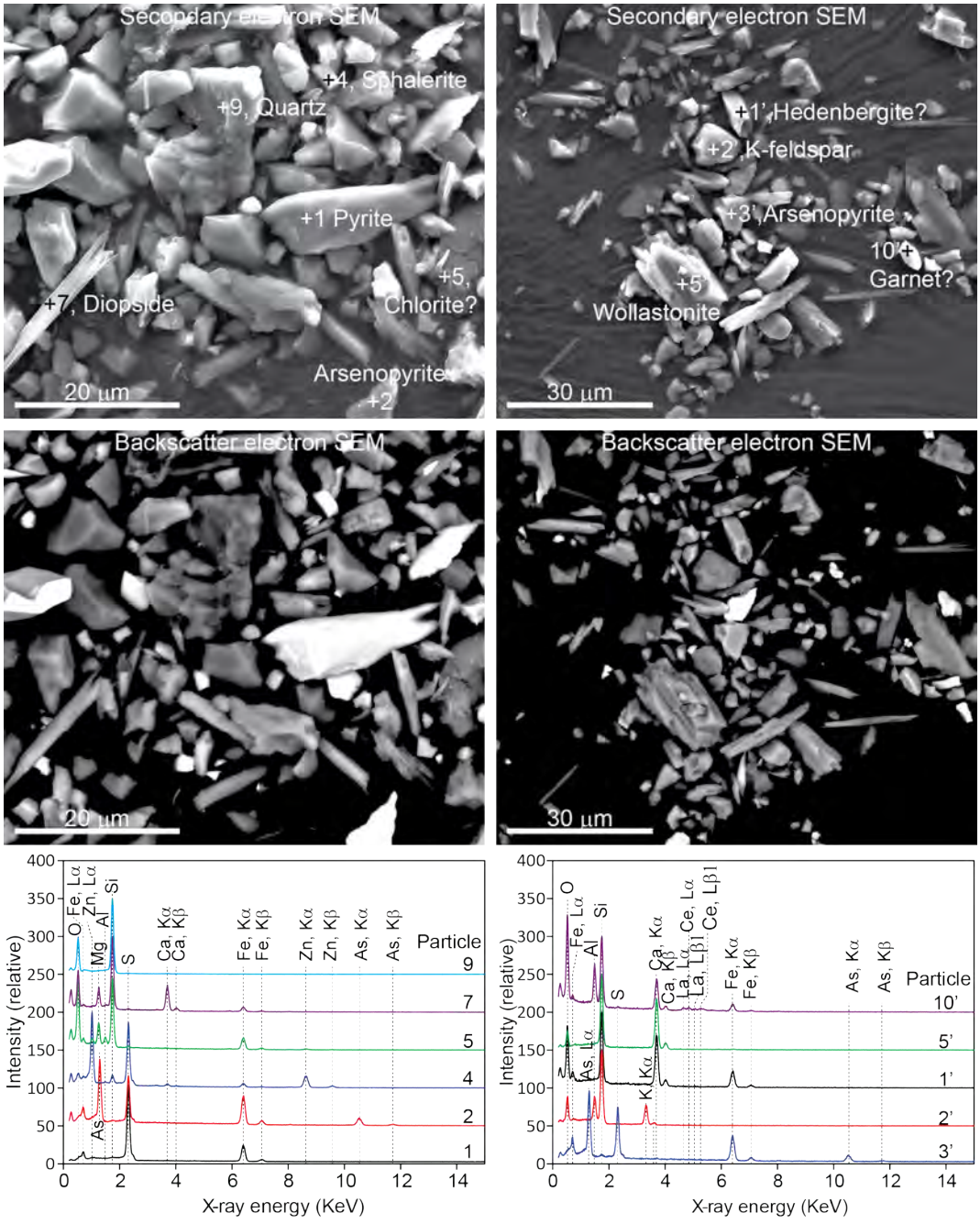

Figure 3.22: SEM analysis of multiples particles from sample 4K. There was evidence of pyrite, arsenopyrite, quartz, feldspar, wollastonite, and diopside.

3.4.1.3 Soluble: 8E

Iron compounds were found to contain ferric, ferrous, and both oxidation states together in some mineral phases. For example, sample 8E contained copious amounts of copiapite, indicated by XRD analysis. Sample 8E was also characterized by McClure (2012). The major constituent of sample 8E was copiaipite, making it almost entirely soluble in water.

The elemental information from XRF analysis of the bulk fraction of samples revealed the preliminary extent of contamination of tailings. All the samples had a level of sulfur from 6.99 to 15.2 percent weight. The oxidized samples 4M and 4L had 6.61 and 2.52 weight percent of Al_2O_3, while soluble 8E had less than 1 weight percent present. Similarly, 4M and 4L had 37.9 and 14.4 weight percent of SiO_2 while 8E had less than 1 weight percent present. Sample 4M had 8.11 weight percent of Fe_2O_3, while 4L and 8E had 25.3 and 29.4 weight percent. Sample 4L had the highest amount of Cu at 1,100 mg/kg. Zinc was high at 4,100 mg/kg in sample 4L and 12,000 mg/kg in sample 8E. The sample 4M had the highest amount of Pb at 7,100 mg/kg, additionally, sample 4L had 3,200 mg/kg Pb. All the samples had high levels of As in them. Sample 4M had 3,300 mg/kg As, 4L had 12,000 mg/kg As, and 8E had 15,000 mg/kg As. Sample 4M had the most Zr at the low level of 100 mg/kg. The unoxidized samples 4D and 4K had low amounts of S 2.04 and 2.82 percent weight. Conversely, they had high amounts of Mg at 2.01 and 2.73 percent weight. Samples 4D and 4K have significant amount of Pb, As, Cu. Both unoxidized samples had the highest amount of Cu recorded, 4K with 1,600 mg/kg and 4D with 1,300 mg/kg (Tables 3.2 and 3.3).

	% (wt)												
Sample ID	Na_2O	MgO	Al_2O_3	SiO_2	P_2O_5	S	Cl	K_2O	CaO	TiO_2	MnO_2	Fe_2O_3	BaO
Oxidized Tailings													
4M	0.22	0.53	6.61	37.9	<0.05	6.99	<0.02	5.57	8.56	0.38	0.03	8.11	0.16
4L	0.08	0.48	2.52	14.4	0.12	15.2	<0.02	1.83	6.86	0.21	0.07	25.3	0.05
Unoxidized Tailings													
4D	<0.05	2.01	4.42	39.8	0.17	2.82	<0.02	1.94	29.7	0.23	0.41	14.1	0.06
4K	<0.05	2.73	3.65	37.4	0.19	2.04	<0.02	1.73	32.2	0.21	0.52	9.64	0.04
Soluble													
8E	<0.05	0.27	0.15	0.15	<0.05	12.1	<0.02	<0.01	0.25	<0.01	0.06	29.4	<0.01

Table 3.2: XRF results in weight percent for samples from Zimapán, Mexico. - = below detection limits.

	mg/kg											
Sample ID	Cr	Co	Ni	Cu	Zn	As	Sn	Pb	Sr	Zr	Rb	Y
Oxidized Tailings												
4M	<10	13	<10	530	961	3,300	72	7,100	243	100	199	11
4L	<50	<50	<50	1,100	4,100	12,000	<100	3,200	100	54	79	<50
Unoxidized Tailings												
4D	75	49	53	1,300	9,200	9,600	<50	2,200	118	52	67	28
4K	78	32	36	1,600	8,900	7,000	<50	2,900	132	49	75	21
Soluble												
8E	<50	<50	<50	287	12,000	15,000	<200	133	<50	<50	<50	<50

Table 3.3: XRF results in mg/kg for samples from Zimapán, Mexico

3.4.2 XANES

The speciation of arsenic in the samples were determined using a synchrotron light source and its microprobe capabilities. XANES experiments were used to identify As speciation and confirm by comparing with standards of As(III), As(V), and arsenopyrite(As(-I)). However, not all samples correlated precisely, indicating additional oxidation states can be present, such as As(0) (Figures 3.23 and 3.24). The samples arsenopyrite, 4D, and 4K had similar activation energies at 11,867.7 eV, indicating they contain the same oxidation state, As(-I). Similarly, the samples scorodite, 4L, 4M, 8E, and As(V) standard share the same activation energy of 11,874.4 eV, indicating the presence of As(V).

Despite the large variation in the silt and clay fractions of samples 4M and 4L, XANE analysis on individual particles showed remarkable similarity. Suggesting they were dominated by As(V) species. The XANE and EXAFS do not appear to be able to differentiate the arsenate absorbed on or incorporated into different minerals such as ferrihydrite, goethite, jarosite, or scorodite.

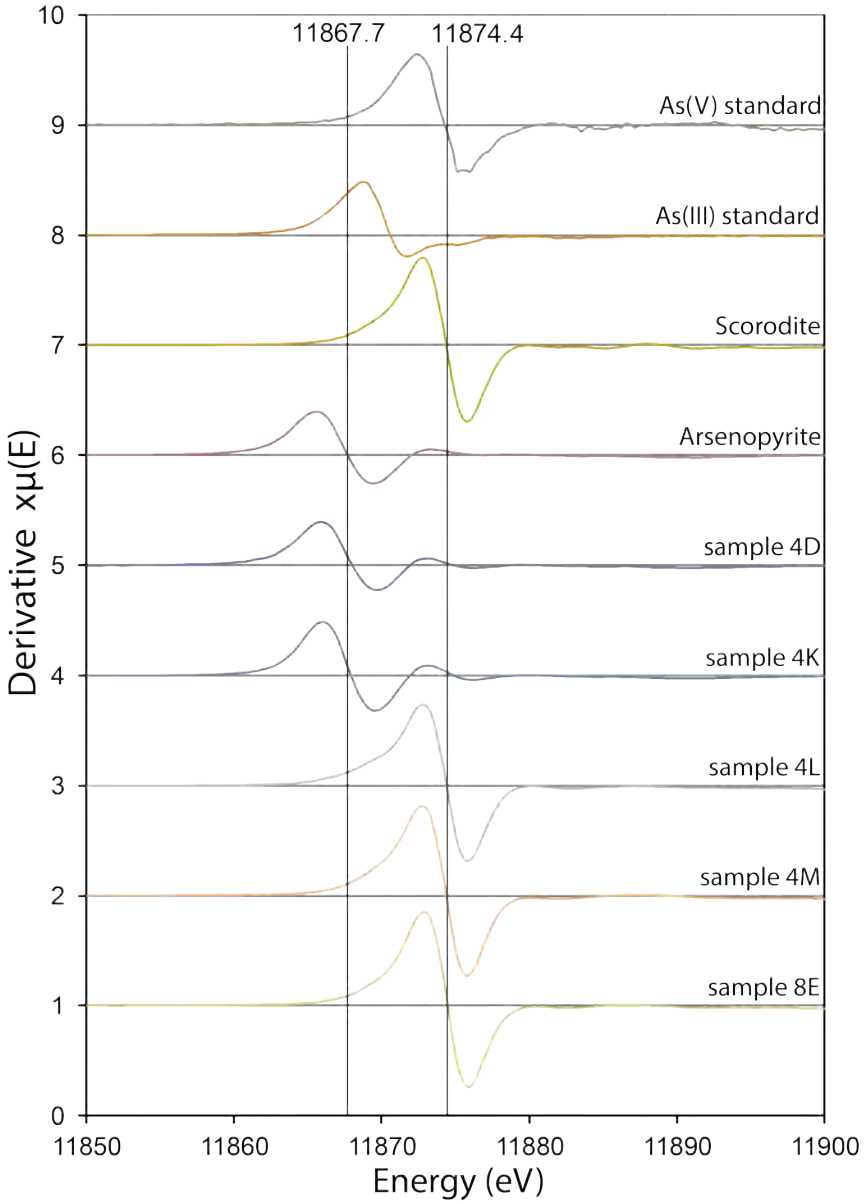

Figure 3.23: XANES results of samples and standards showing a variety of arsenic species present.

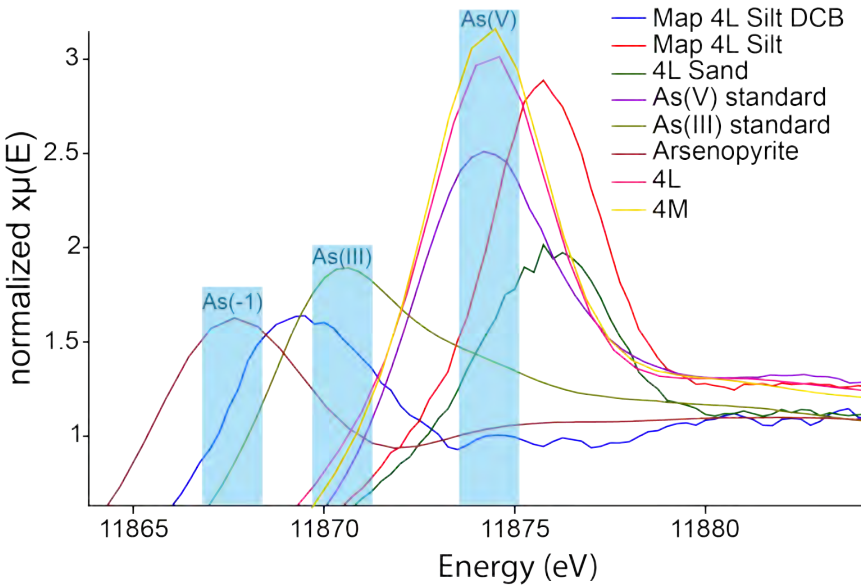

Figure 3.24: Sample binding energies from XANES experiments helped deduce the oxidation states present. The samples 4M and 4L correlated with the As(V) standard. In addition, there were an As(III) standard, and arsenopyrite was used for an As(-I) standard. The samples 4L Sand, Map 4L Silt, and Map 4L Silt DCB did not correlate to a standard for oxidation identification.

A brief X-ray fluorescence (XRF) survey was conducted on the sample 4L silt fraction to get a general idea about the elemental compositions of the sample and to locate the As-rich particles for X-ray absorption spectroscopy analysis. The XRF spectrum of an As-rich particle showed intense Kα and Kβ fluorescence of Fe and As (Fig. 3.25). Moderately intense Zn and weak Cu fluorescence were also observed. Escape peak of Fe Kα and many sum peaks (pile up of two or more X-ray photons) were observed on the spectrum too, which complicated the assignments of the peaks. The X-ray fluorescence was recorded in air, and therefore, most of the low-energy X-rays were absorbed by air. Only weak S, K, and Ca were observed. The X-ray fluorescence intensities of K, Ca, Cr, Mn, Fe, Ni,Cu, Zn, and As were recorded for elemental mapping. Only Fe, As, Cu, Zn, and K were discussed here due to the

relative higher abundance of As, Cu, and Zn in the samples, and the association of these elements with iron oxides and jarosite in the oxidized tailing.

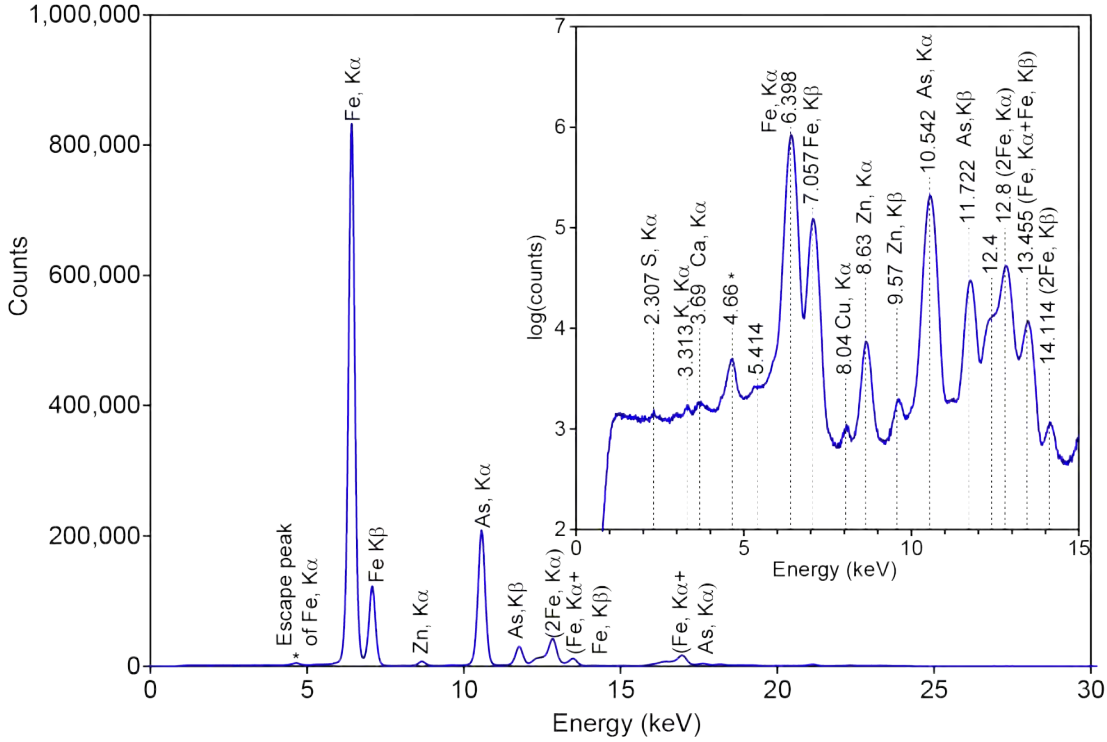

Figure 3.25: X-ray fluorescence spectrum of sample 4L silt recorded in air when the sample was radiated with a source X-ray of energy 12.8 keV.

Elemental mapping was conducted on fresh tailing sample 4K bulk, and oxidized samples 4L (sand and silt) and 4M (silt). Due to the similarity between samples 4L and 4M, only 4L silt was chosen to see the affects of removing iron oxide and jarosite with the DCB method (4L silt+DCB) on the As speciation. Based on the mapping results, selected particles in each sample was analyzed for the As X-ray absorption spectra (XANE and EXAFS). The distributions Fe, As, Cu, Zn, and K were shown in Figure 3.26.

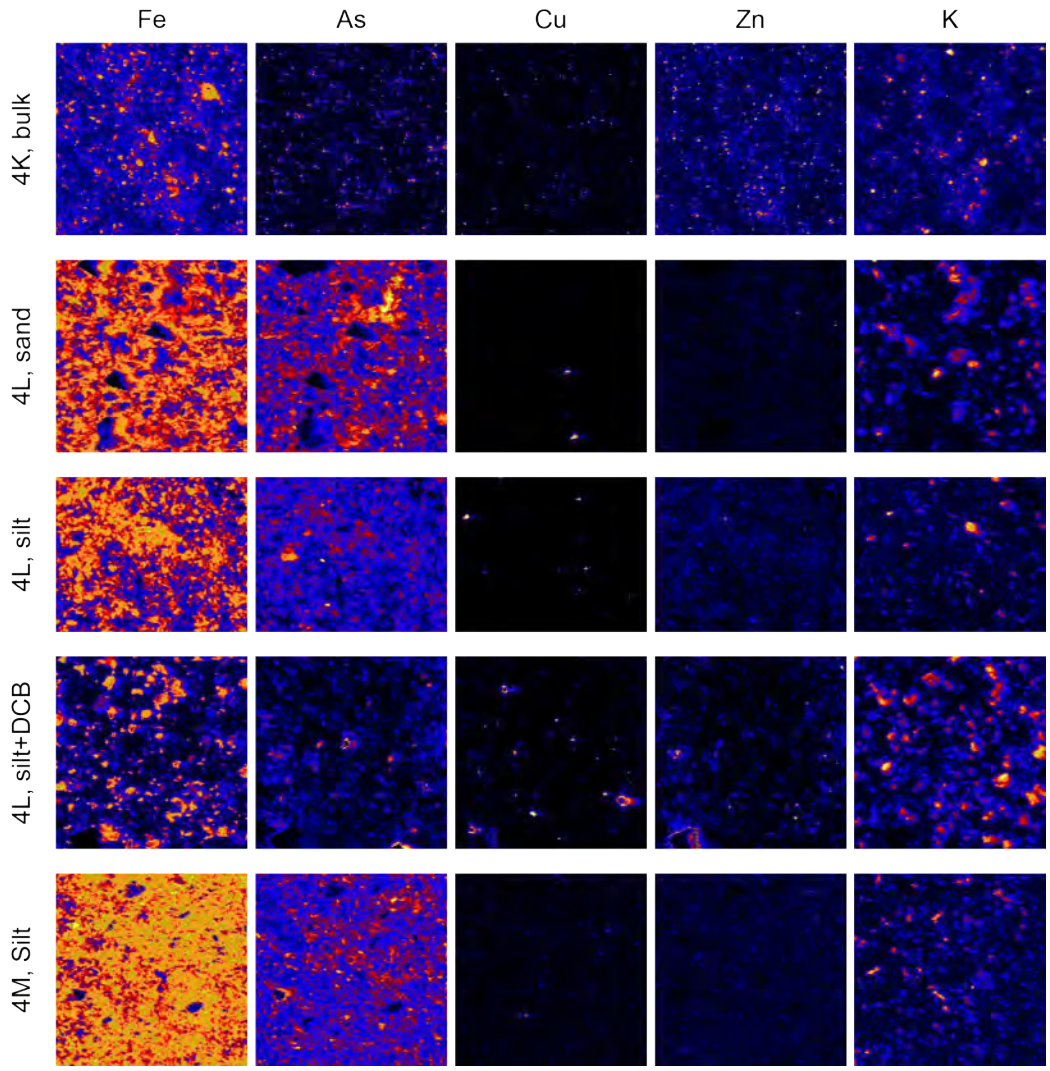

Figure 3.26: Elemental mapping based on the Kα X-ray fluorescence intensities of the elements recorded in air with a radiation source X-ray of energy 12.8 keV.

The element mapping (Fig. 3.26) indicated that Fe and As were more homogeneously distributed in the oxidized samples 4L and 4M, but the fresh sample 4K and the DCB treated 4L silt were more heterogenous. The Cu was distributed more in isolated spots in all samples, where it appeared that Zn was more homogenous in the fresh sample 4K and the DCB treated 4L silt. The K distribution showed much

less variations among the samples.

It is generally believed that As and the heavy metals are associated with iron oxides of iron sulfide minerals. The correlation coefficient analysis on the X-ray fluorescence intensities of the elements indicated different association relationships among the oxidized (4L, 4M) and unoxidized (4K) samples and between the sample before and after the DCB treatment (4L) (Table 3.4, and Figs.3.27 and 3.28). In the fresh tailing sample 4K bulk and the DCB treated 4L silt, Fe did not show high correlations with any of the heavy elements or K. Although, the As was highly correlated to Fe in the oxidized 4L and 4M samples without the DCB treatment.

Element Cu had low correlation with no elements in the five samples analyzed. In sample 4L (sand, silt, and silt+DCB), a high correlation between Zn and As were observed. Moderate to high correlations between Zn and Fe were observed in the oxidized samples 4L and 4M, but such correlation was not observed on the fresh sample 4K bulk or the DCB treated 4L silt. In all of the samples, Cu did not appear to have significant correlations with Fe, As, Mn, Ni. Only moderate correlation was observed between Cu and Zn in 4M silt.

Jarosite was found in the oxidized samples 4L and 4M as indicated by the XRD and electron microscopic data. It was suspected that jarosite might incorporate or adsorb As and other heavy metals. Yet, the K was poorly correlated to all other elements examined.

The correlation differences described above indicated that As and the heavy metals had heterogenous distributions in the fresh tailings. The As and heavy metals were poorly associated with each other when they formed sulfide minerals. When the sulfide or arsenide minerals were oxides, however, the As and heavy metals tend to associate with iron oxides, but not necessarily with a constant compositional ratio. The iron oxides may also not adsorb all of the heavy metals simultaneously. This

could be due to the dynamic changes of the solution chemistry when the iron oxides formed.

The poor correlation between K and the heavy metals implied that jarosite may not have incorporated or adsorbed As or the heavy metals as has been suspected. This appears to contradict the SEM/EDS data reported early.

Element	Sample	Ca	Cr	Cu	Fe	K	Mn	Ni	Zn
As	4K, Bulk	-0.061	0.061	-0.007	0.048	0.017	-0.002	0.095	-0.044
	4L, Sand	-0.076	-0.105	-0.039	**0.583**	-0.029	-0.233	-0.212	**0.484**
	4L, Silt	-0.028	0.311	-0.017	**0.760**	0.115	0.376	0.372	**0.619**
	4L, Silt+DCB	-0.020	0.015	0.109	0.050	-0.021	-0.031	-0.017	**0.479**
	4M, Silt	-0.050	-0.073	0.038	**0.445**	0.069	-0.211	-0.132	0.266
Ca	4K, Bulk		0.003	0.003	0.069	0.113	0.228	0.090	-0.008
	4L, Sand		0.003	-0.010	-0.024	0.109	-0.035	-0.054	-0.047
	4L, Silt		0.042	-0.008	0.071	0.079	0.154	0.040	-0.015
	4L, Silt+DCB		0.028	-0.027	0.120	-0.003	0.207	-0.008	-0.021
	4M, Silt		0.004	-0.032	0.040	0.108	-0.009	-0.020	-0.028
Cr	4K, Bulk			0.053	0.327	0.079	0.258	0.246	0.021
	4L, Sand			0.008	-0.078	-0.046	**0.445**	0.122	-0.021
	4L, Silt			0.013	**0.439**	0.052	0.344	0.270	0.288
	4L, Silt+DCB			0.021	0.171	-0.023	0.205	0.116	0.004
	4M, Silt			-0.008	-0.080	-0.018	**0.474**	0.066	-0.025
Cu	4K, Bulk				0.048	0.027	0.001	0.102	0.110
	4L, Sand				-0.029	-0.020	0.005	0.020	0.118
	4L, Silt				0.014	-0.011	0.023	0.124	0.131
	4L, Silt+DCB				-0.004	-0.003	0.019	0.179	0.215
	4M, Silt				0.176	0.004	-0.050	-0.007	0.396
Fe	4K, Bulk					0.028	0.196	0.033	0.020
	4L, Sand					-0.149	-0.231	-0.222	0.395
	4L, Silt					0.072	**0.532**	**0.446**	**0.707**
	4L, Silt+DCB					-0.216	0.196	0.027	-0.068
	4M, Silt					0.021	-0.306	-0.256	0.339
K	4K, Bulk						0.079	0.029	0.043
	4L, Sand						-0.123	-0.147	-0.021
	4L, Silt						0.030	0.023	0.053
	4L, Silt+DCB						-0.097	-0.089	-0.060
	4M, Silt						-0.098	-0.103	0.001
Mn	4K, Bulk							0.083	0.022
	4L, Sand							0.086	-0.112
	4L, Silt							0.366	0.393
	4L, Silt+DCB							0.246	-0.022
	4M, Silt							0.070	-0.108
Ni	4K, Bulk								0.055
	4L, Sand								-0.079
	4L, Silt								**0.426**
	4L, Silt+DCB								0.150
	4M, Silt								0.029

Table 3.4: Correlation coefficients of the K-α X-ray fluorescence intensities of elements during the XRF mapping analysis when the samples were radiated with an X-ray source of energy 12.8 keV.

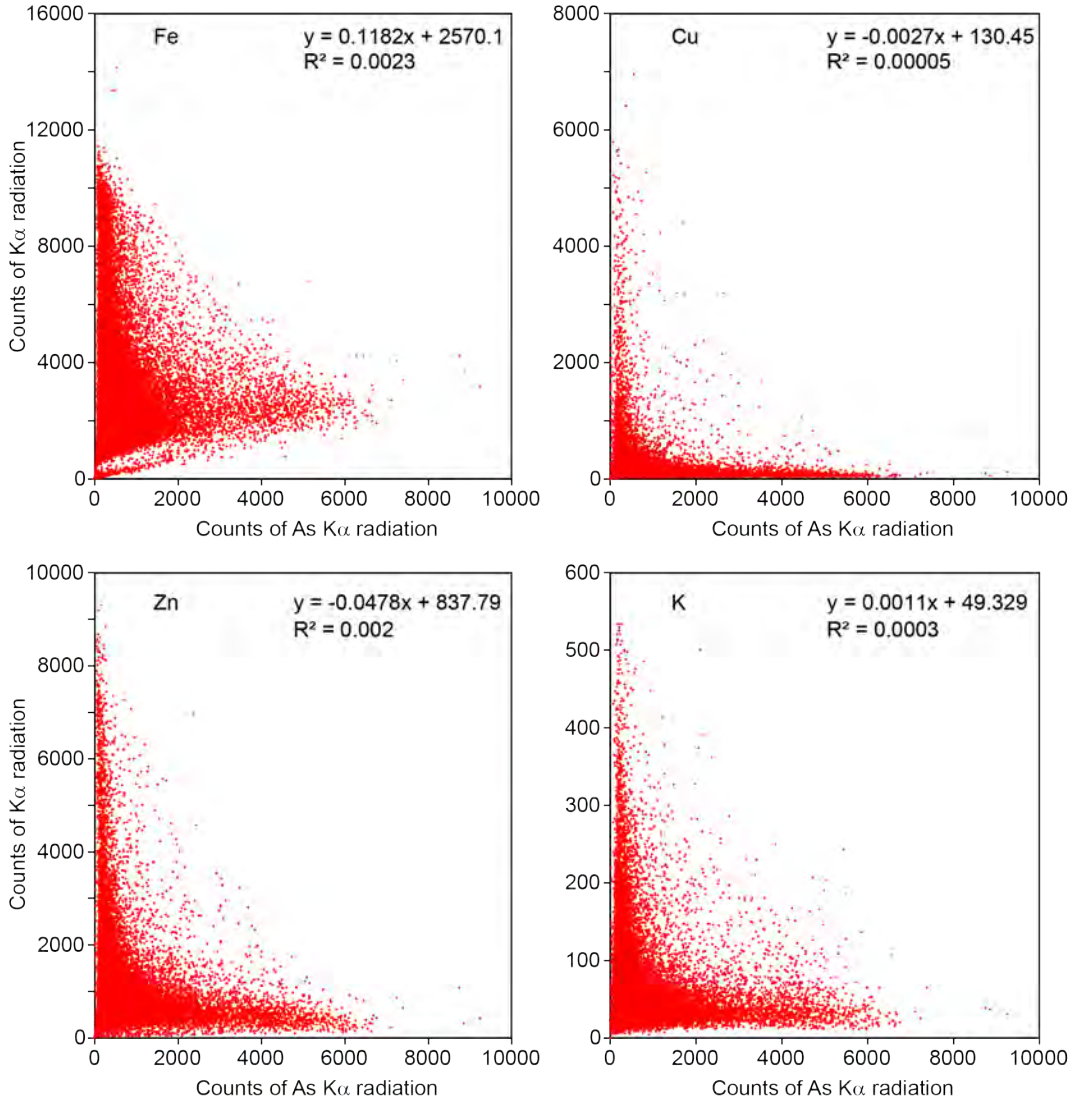

Figure 3.27: Correlations of As with Fe, Cu, Zn, and K in fresh tailing sample 4K bulk based on the Kα X-ray fluorescence intensities of the elements recorded in air with a radiation source X-ray of energy 12.8 keV.

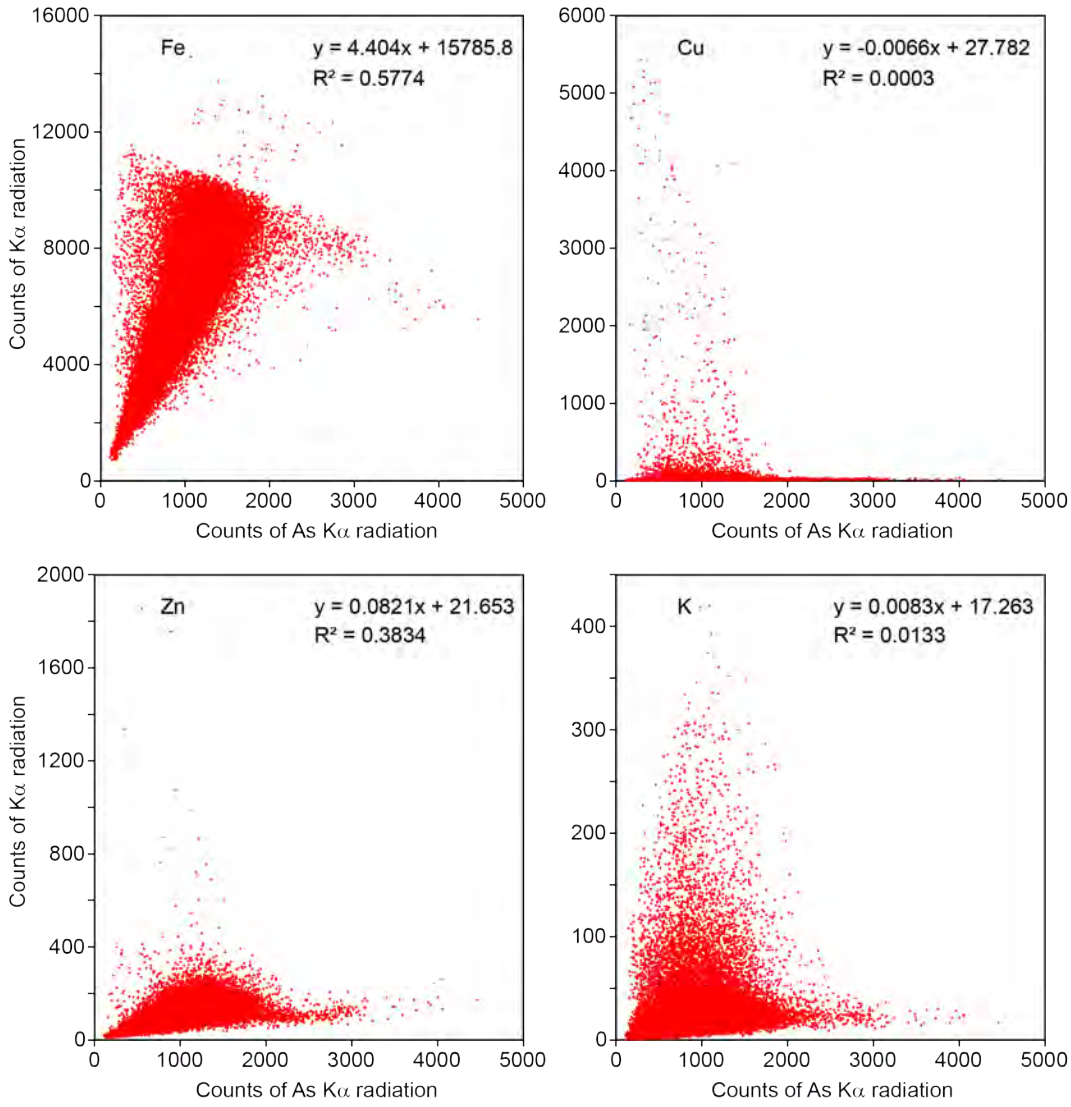

Figure 3.28: Correlations of As with Fe, Cu, Zn, and K in oxidized tailing sample 4L silt based on the Kα X-ray fluorescence intensities of the elements recorded in air with a radiation source X-ray of energy 12.8 keV.

Synchrotron XRF mapping helped deduce trends and changes observed on the XRD patterns that occurred after selective dissolution treatments. After DCB treatment, 4L silt fraction noticeably lost a great amount of iron oxides and jarosite.

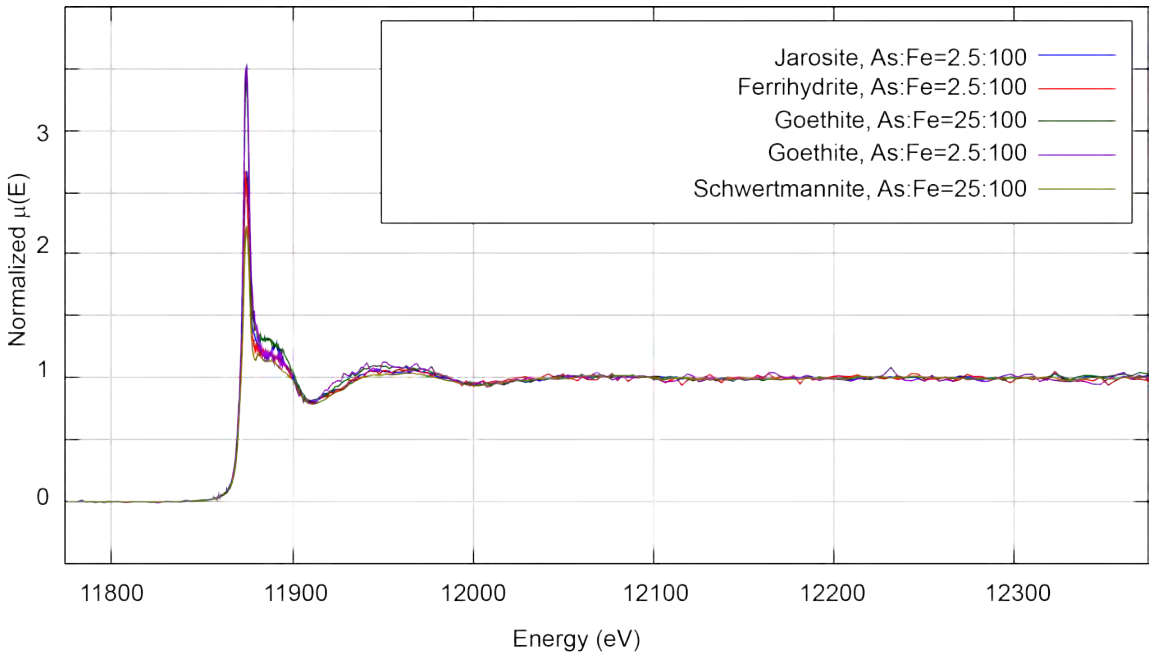

Figure 3.29: The arsenic X-ray absorption spectra of synthetical ferrihydrite, goethite, jarosite, and schwertmannite in the presence of As with a As:Fe molar ratio of 2.5:100 or 25:100.

3.4.3 The X-ray Sorption Spectra of Arsenate Incorporated or Adsorbed by Synthetical Iron Oxides

As jarosite, goethite, ferrihydrite, and possibly schwertmannite were identified in this study, these minerals might adsorb or incorporate As in their structures or surfaces. Relative simple single phases of these minerals were synthesized in the presence of arsenate with a As:Fe molar ratio of 2.5:100. For goethite, a 25:100 As:Fe ratio was also used in hope to get high concentrations of As in the specimen. The X-ray diffraction analysis indicated ferrihydrite and goethite formed at the 2.5:100 As:Fe ratio, yet only short-range ordered ferrihydrite formed at the 25:100 As:Fe ratio.

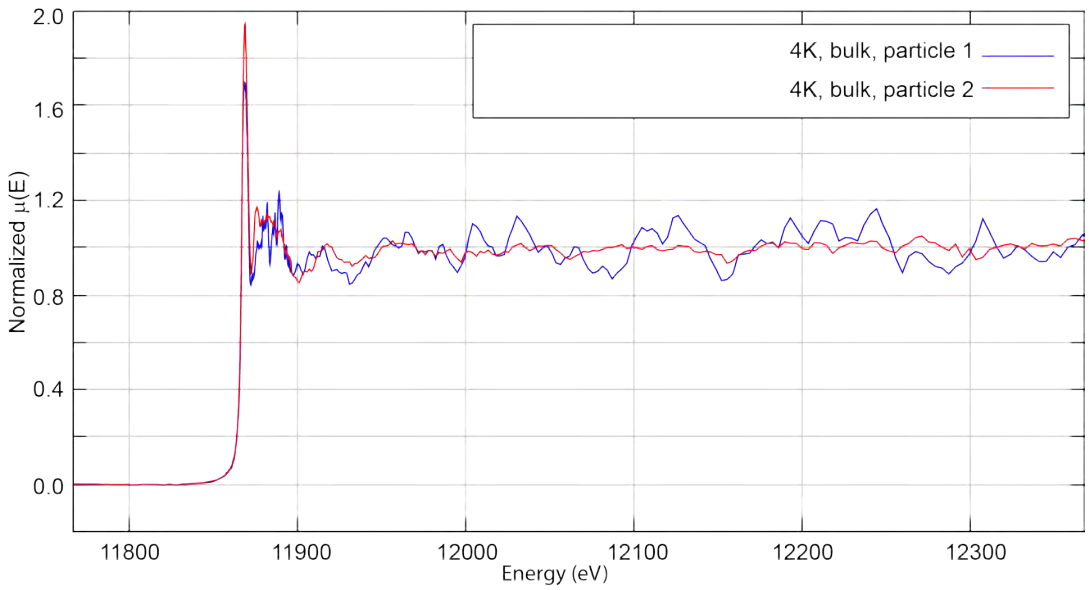

Figure 3.30: Micro arsenic X-ray absorption spectra of selected particles in fresh tailing sample 4K.

For these synthetical phases, their As X-ray absorption spectra (Fig. 3.29) look nearly identical to each other except the white line intensity. The nearly identical edge position and shape in the EXAFS range suggest that arsenate was bonded to the iron oxide surfaces with a very similar mechanism. The similarity of the spectra suggest it will be hard to differentiate the arsenate adsorbed or incorporated by these phases.

3.4.4 X-ray Sorption Spectra of Arsenic in Selected Particles

3.4.4.1 Fresh Tailing Sample 4K Bulk

The micro-Xray sorption spectra of selected particles from the fresh tailing sample 4K were noisy in the EXAFS range, yet the absorption edges of the two spectra occurred at about 11867.7 eV, which was also the As absorption edge or arsenopyrite. The edge positions indicated a more reduced arsenic species in the fresh tailing.

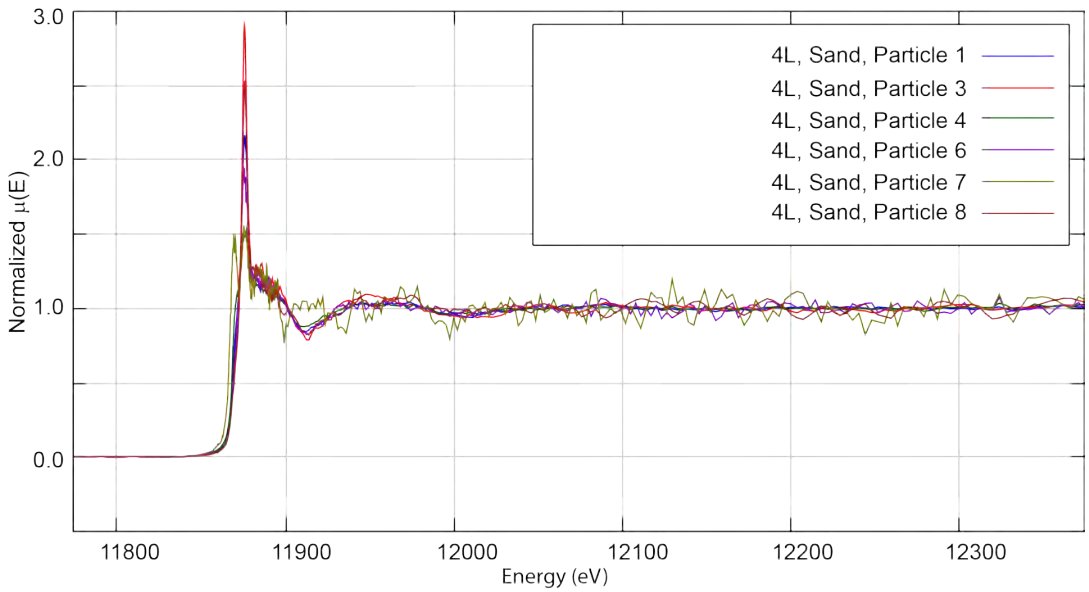

Figure 3.31: Micro arsenic X-ray absorption spectra of selected particles in oxidized 4L, sand fraction.

3.4.4.2 Oxidized Sample 4L Sand and Silt Fraction

The micro X-ray absorption spectra of As in the selected particles in the 4L sand fraction (Fig. 3.31) had different qualities. Yet, two absorption edges were identified: most of the particles had an edge position at 11874.25-11874.75 eV, and a one particle had a absorption edge at 11868 eV. Those two edges indicated that both arsenate and arsenide like in arsenopyrite occurred in the sand particle.

The micro-XAS spectra of selected eight particles in the 4L silt fraction were nearly identical to each other, all of them had a absorption edge in the rand 11874.25-11874.75 eV, and only one particle showed a shoulder at the lower energy side of the edge (Fig. 3.32). The high similarity of the XAS spectra of the particles indicated that the arsenate is the dominate species in the samples, and either the adsorbed/inocorporated As in the minerals had similar bonding environments or the

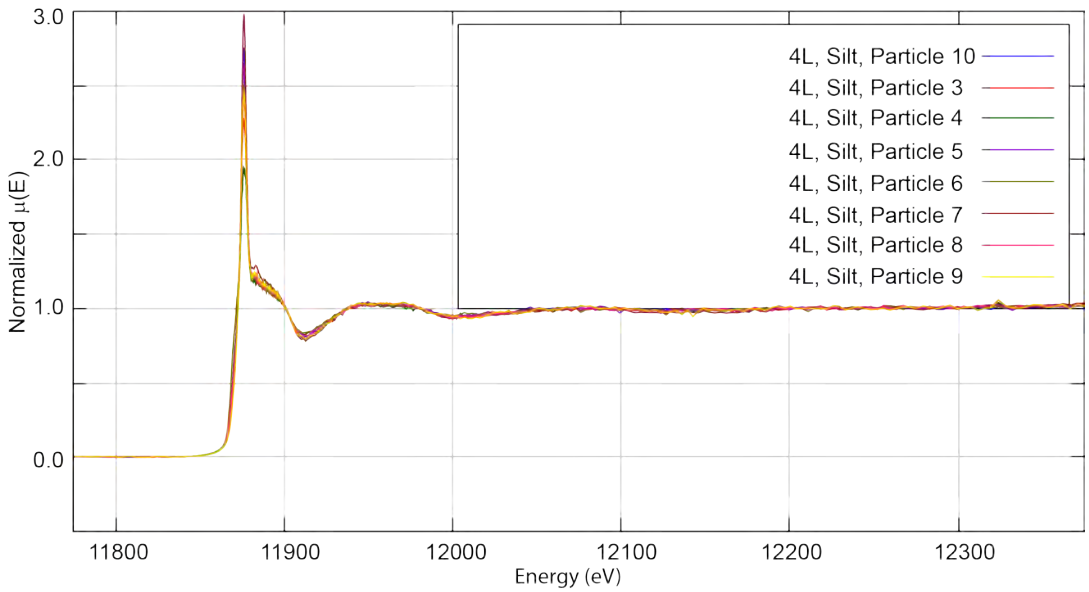

Figure 3.32: Micro arsenic X-ray absorption spectra of selected particles in oxidized 4L, silt fraction.

spatial resolution of the micro-X ray beam was not high enough to different the particles.

When iron oxide and jarosite were removed from the 4L silt fraction, the micro XAS spectra of the particles became noisy again, yet two distinct absorption edge positions, one at 11867.5 eV and the other at 11874.75 eV, showed up (Fig. 3.33). The DCB treatment apparently revealed the unoxidized arsenic species in the samples, which is consistent with the SEM observation. Yet, the occurrence of of absorption edge at 11874.75 eV suggested that there were arsenate species remained in the sample after the DCB treatment. This species must not be ferrihydrite, goethite, or jarosite. We could not positively identify schwertmannite or scorodite with XRD, SEM, TEM,or IR in sample 4L, we would assume this the remaining arsenate was mainly from the scorodite-like phase.

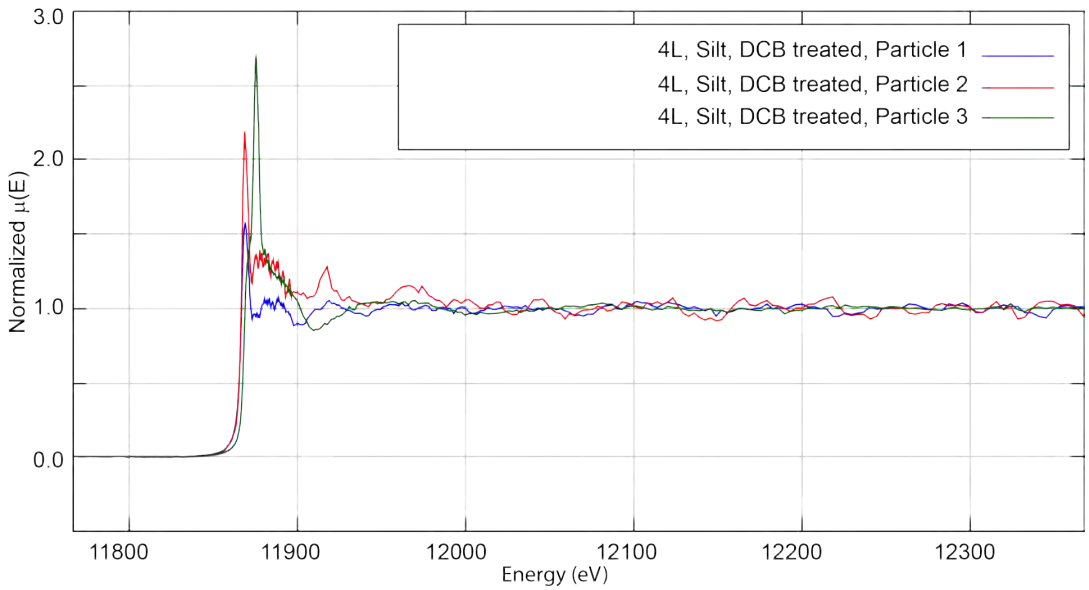

Figure 3.33: Micro arsenic X-ray absorption spectra of selected particles in oxidized 4L, silt fraction, after removing iron oxides and jarosite with DCB treatment.

3.4.4.3 Oxidized Sample 4M Silt Fraction

The micro-XAS spectra of selected six particles in the 4M silt fraction were very similar to those particles in the 4L silt fraction. All of the absorption edges occurred at 1874.75 eV (Fig. 3.34), suggesting arsenate was the dominated species in the particles.

The above micro-XAS analyses of the fresh and oxidized tailing particles suggested there were distinct arsenic species in the tailing materials. It appeared that there were mainly two species: oxides form of arsenate As(V) and the reduced form arsenide As(-I) as in arsenopyrite. In the oxidized tailing samples 4L and 4M, some of the arsenide minerals still remained unoxidized.

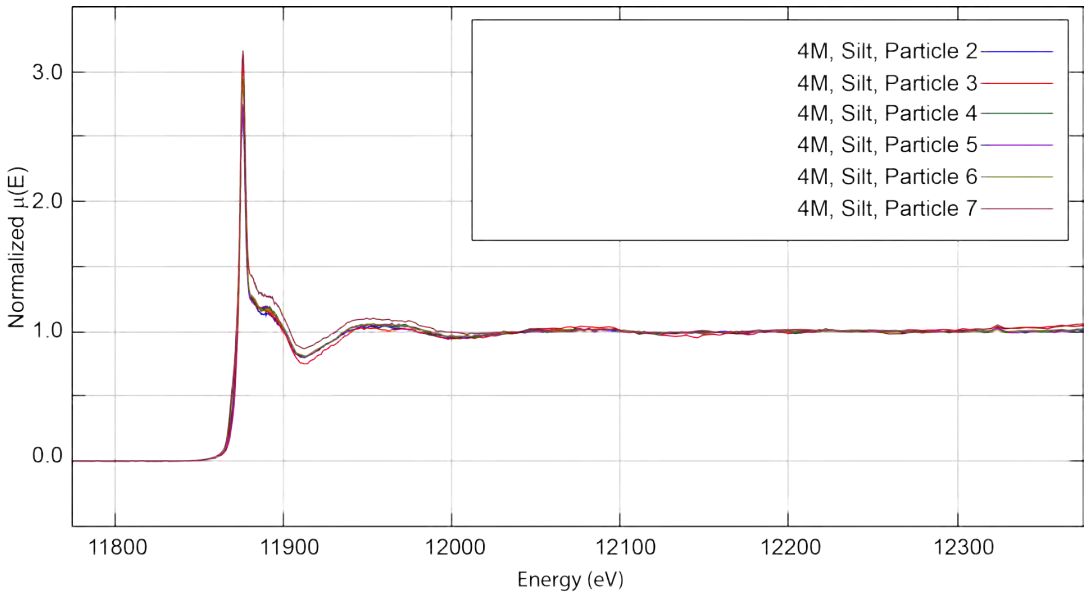

Figure 3.34: Micro arsenic X-ray absorption spectra of selected particles in oxidized 4M, silt fraction.

3.4.5 Linear Combination Analysis of Bulk Samples 4D, 4K, 4L, and 4M

As the arsenic XAS spectra of the five synthetical iron oxides were very similar to each other, it suggested that it would be difficult to get accurate quantitative analysis about the As-adsorbing/incorporating hosting minerals. Yet, the relative ratio of the reduced arsenic species vs. the oxidized arsenate species could be estimated by the linear combination analysis (Fig. 3.35 and Table 3.5). The preliminary linear combination analyses suggested for the oxidized samples 4L and 4M, the fit and the experimental data matched well with the available standards. Yet, the ratio of the arsenate-containing species such as ferrihydrite, jarosite, goethite could not be unambiguously determined by the fitting, this is because of the high similarity of the As XAS spectra of these minerals.

The fitting with current standards suggested more than 85% of the arsenic was in the reduced form like in the arsenopyrite occurred in the fresh tailing samples 4D and 4K, yet obvious absorption mismatch were observed in these two fresh samples, suggesting that there were other reduced arsenic species occurred in the samples, most likely these minerals were other sulfide minerals containing minor amount of arsenic. A more careful comparing with the reference patterns reported in the literature will be needed to narrow down the possible species.

3.5 Discussion

There were large amounts of pyrite with ferrous iron yet to be oxidized, otherwise the majority of iron were found in ferric iron oxide complexes. Iron (oxy)hydroxides and iron sulfates dominated the waste deposits. Ferric iron forms stable mineral phases, although it can be dissolved and mobilized in low pH solutions. Low pH solutions could be present after episodes of heavy rain, promoting pyrite oxidation. Other mines sites in the region have shown varying mobility during rainy/dry sea-

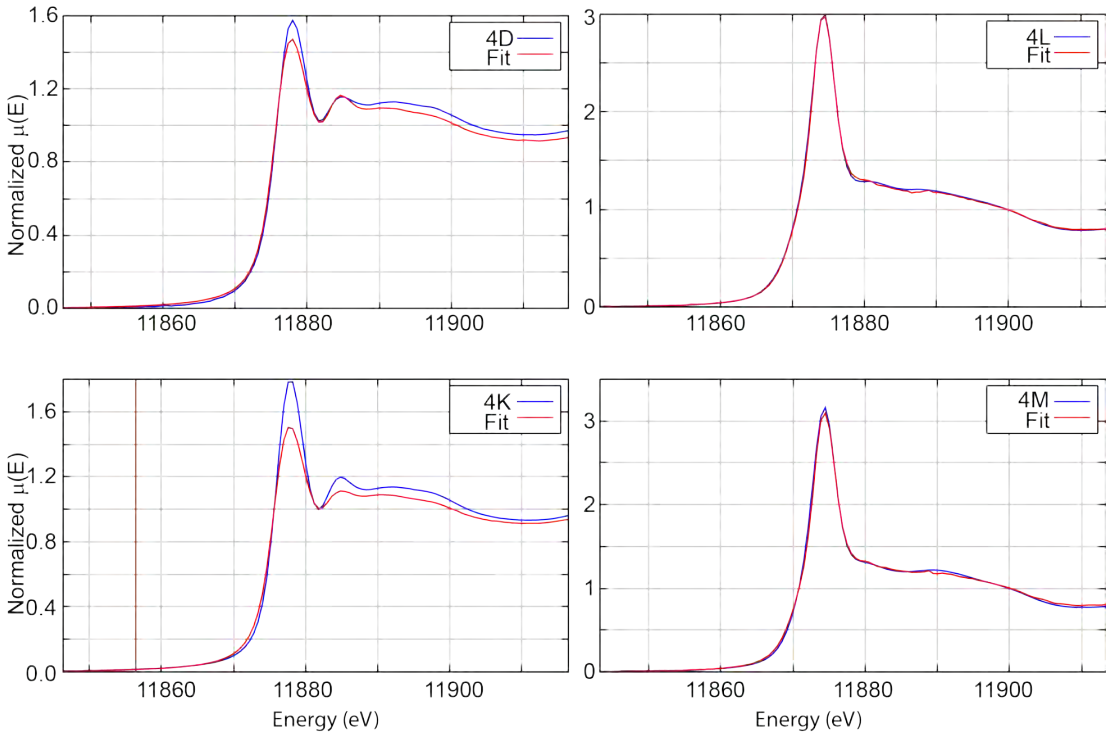

Figure 3.35: The X-ray absorption near edge structure spectra of bulk fresh tailing samples 4D and 4K, and the bulk oxidized tailing samples 4L and 4M, and their linear combination fitting.

sons and with fresh/weathered tailings (Armienta et al., 2016). Mobility of metals suggests a need for proper land management in conjunction with adequate barriers to support all seasonal threats to prevent AMD from leaving the site. The array of metals present would require multiple strategies to be implemented to control them all and provide fail-safes.

Whereas, a significant amount of both ferric and ferrous iron was present, it was beneficial that As associated itself to Fe complexes. Arsenopyrite (As^{-1}) was a common phase, as was pyrite. Scorodite (As(V)), a hydrated ferric arsenate, was found in large quantifies in multiple samples. One of scorodite's precursor is arsenopyrite. Following scorodite, the next transformation can be to iron oxides, such as goethite

Table 3.5: Linear combination fitting of the XANE spectra of bulk samples 4D, 4K, 4L, and 4M with standard samples arsenopyrite, scorodite, soidum arenite As (III), and As-containing synthetical iron oxides gothite, jarosite, ferrihydrite.

Sample	4D	4K	4L	4M
Arsenopyrite	0.853	0.882	0.003	0.000
As(III) standard	0.106	0.099	0.102	0.075
Goethite-25As	0.040	0.000	0.116	0.178
Goethite-2.5As	0.001	0.019	0.213	0.271
Scorodite		0.000	0.566	0.476
Ferrihydrite-As		0.000	0.000	0.000
Jarosite-As		0.000	0.000	0.000
Sum	1.000	1.000	1.000	1.000
R-factor	0.00433	0.01802	0.00065	0.00168
Chi-square	0.09775	0.43103	0.02720	0.07702
Reduced chi-square	0.00122	0.00546	0.00035	0.00099

(Dove and Rimstidt, 1985). The complex transformations within geochemical pathways can be spatially dependent on what type of iron and other contaminants are present in that one specific area. If one phase of mineralization processes consumes all of one element, it may not be available for adjacent reactions.

To note, discrepancies in XAS analysis has been found in literature stemming from varying coordination chemistry. Identical As oxidation states can have different binding energies during XAS experiments due to various bonding, such as As-S and As-O (Smith et al., 2005). Although these elements are present in this system, no evidence of such an occurrence was found. This is another example of how complex the geochemical reactions can take place, making proper analysis more difficult.

In this region of Mexico, modeling by Armienta et al. (2001) found the dissolution of scorodite and arsenopyrite to be the reason behind natural arsenic contamination. This project has found copious amounts of scorodite and arsenoyrite at sample sites

near Zimapán, Mexico, both are major sources and a possible fate of arsenic in this system too. Other research in the region found arsenic's oxidation state, reported by Armienta et al. (2001), was arsenate ($As^{5+}/As^{3+}>0.95$), which coincides the findings of this study. They found that the ratio of As^{5+} to As^{3+} was greater than 95 percent As^{5+} in groundwater. Low Eh and high temperatures were attributed to high As concentrations in groundwater, while the limestone alkaline environment enhanced As^{5+} mobility.

The samples collected for this study, 4M and 4L, were highly oxidized, hence their high amounts of iron oxides, a sign of weathering and age. The tailings underwent weathering for several years allowing for different stages of dissolution and precipitation to be observed. When tailings, like 4M and 4L, leach heavy metals during early oxidation processes, the precipitation of iron oxides can help concentrate or retain heavy metals. This temporary retention makes a potential source of additional heavy metals to be released upon acidification and dissolution of the iron oxides.

3.6 Conclusions

The most dominant species of arsenic were As^{1-} and As^{5+}. In the solid phase, the largest contributor of As^{1-} was arsenopyrite, and As^{5+} was the absorbed/incorporated arsenate in iron oxides. Major mineral phases identified were goethite, hematite, jarosite, plumbojarosite, scorodite, melanterite, pyrite, and lesser so micas, silicates, pyroxenes, and feldspars. The iron oxides were ubiquitous to the tailing samples collected, while precipitated iron sulfates were sporadic but concentrated. There was an excessive amount gypsum present in oxidized tailings. To reiterate, the samples 4L and 4M were highly oxidized, sample 4E was minimally oxidized, and 8E was a secondary precipatate mainly copiapite.

The Zimapán region is located in a carbonate rich region and theoretically could

neutralize AMD, but fails to do so. It can help mitigate transport of AMD, but does not solve the problem of pooling static AMD in drainage ponds and low land. Land management would be essential to mitigate the migration of AMD. For temporary relief, even tailings were saturated with calcite, the pH would not be neutral, but high enough to stabilize iron oxides and prevent dissolution and further release of metals. The stable ferric oxides and sulfates are beneficial when they facilitate the sequestration of metals and limit their mobility.

The oxidation states of arsenic can generally follow the age the tailings because of increased weathering and oxidation of the original mineral species, usually an iron sulfide. The primary minerals, such as arsenopyrite, has a reduced form of arsenic before it is oxidized to form As(III) phases, and furthermore to arsenate, which can be adsorbed/incorporated in iron oxides, or form scorodite. The oxidation of arsenic also makes it significantly less toxic, noting that As^{5+} is less toxic than As^{3+}. Nonetheless, neither are safe, yet can be found in both soil and water all around the region.

4. CONCLUSIONS

The geochemical transformations of mine tailings near Zimapán, Mexico provide a good case study for land management, pollution, risk assessment, mineralogy, and dynamic geochemistry with a 60 year time frame.

Heavy metal contamination is prevalent, notably: copper, zinc, lead, and arsenic. Extremely high concentrations of arsenic has been measured in the sediments, up to 110,000 mg/kg As, which was primarily seen in forms of As^{-1} in the fresh tailings and As^{5+} oxidation states in the oxidized tailings. Dissolution and re-precipitation of solid phase iron (oxy)hydroxides directly affect heavy metal transformations and translocation. Poorly crystalline nanoparticles of iron oxides and silica are easily susceptible to geochemical changes due to their high surface area, structural defects, high surface charge, and variation of elements in their structure. Such colloids and nanoparticles that seem to be beneficially stable solids, then become a dust and inhalation risk.

The mine tailings near Zimapán, Mexico pose a great risk via dust, so it is suggested to cap all tailings frequently as possible, keep distance away from people, and provide proper land management for solid and liquid runoff. The limestone environment can potentially help reduce dynamic acid transport, but it is evident that static AMD and accumulation of acid material is not fully neutralized in a carbonate-rich environment.

REFERENCES

Akcil, A. and Koldas, S. (2006). Acid mine drainage (AMD): causes, treatment and case studies. *Journal of Cleaner Production*, 14(12-13):1139–1145.

Armienta, M. A., Mugica, V., and Resendiz, I. (2016). Arsenic and metals mobility in soils impacted by tailings at Zimapan, Mexico. *Journal of Soils and Sediments*, 16:1267–1278.

Armienta, M. A. and O. Cruz, R. R. (1997). Arsenic content in hair of people exposed to natural arsenic polluted groundwater at Zimapan, Mexico. *Bulletin of Environmental Contamination and Toxicology*, 59:583–589.

Armienta, M. A., Ongley, L. K., Rodriguez, R., Cruz, O., Mango, H., and Villasenor, G. (2008). Arsenic distribution in mesquite (*Prosopis laevigata*) and huizache (Acacia farnesiana) in the Zimapan mining area, Mexico. *Geochemistry: Exploration, Environment, Analysis*, 8:191–197.

Armienta, M. A., RodrÃŋguez, C. R., Ongley, L. K., Brust, H., Morales, F., Aguayo, A., Cruz, O., and Ceniceros, N. (2007). Origin and fate of arsenic in a historic mining area of Mexico. *Trace Metals and other Contaminants in the Environment*, 9:473–498.

Armienta, M. A., Rodriguez, R., Aguayo, A., Ceniceros, N., Villansenor, G., and Cruz, O. (1997). Arsenic contamination of groundwater at Zimapan, Mexico. *Hydrogeology Journal*, 5(2).

Armienta, M. A. and Segovia, N. (2008). Arsenic and fluoride in the groundwater of Mexico. *Environmental Geochemistry and Health*, 30(4):345–53.

Armienta, M. A., Talavera, O., Morton, O., and Barrera, M. (2003). Geochemistry of metals from mine tailings in Taxco, Mexico. *Bulletin of Environmental*

Contamination and Toxicology, 71(2):387–93.

Armienta, M. A., Villasenor, G., Cruz, O., Ceniceros, N., Aguayo, A., and Morton, O. (2012). Geochemical processes and mobilization of toxic metals and metalloids in an As-rich base metal waste pile in Zimapan, Central Mexico. *Applied Geochemistry*, 27(11):2225–2237.

Armienta, M. A., Villasenor, G., Rodriguez, R., Ongley, L. K., and Mango, H. (2001). The role of arsenic bearing rocks in groundwater pollution at Zimapan Mexico. *Environmental Geology*, 40(4):571–581.

Asta, M. P., Cama, J., Martinez, M., and Gimenez, J. (2009). Arsenic removal by goethite and jarosite in acidic conditions and its environmental implications. *Journal of Hazardous Materials*, 171(1-3):965–72.

Augustithis, S.-S. P. (1995). *Atlas of the Textural Patterns of Ore Minerals and Metallogenic Processes*. Walter de Gruyter, New York.

Burton, E. D., Johnston, S. G., Watling, K., Bush, R. T., Keene, A. F., and Sullivan, L. A. (2010). Arsenic effects and behavior in association with the Fe(II)-catalyzed transformation of schwertmannite. *Environmental Science & Technology*, 44(6):2016–21.

Cameron, F. K. (1929). The solubility of ferrous sulphate. *The Journal of Physical Chemistry*, 34(4):692–710.

Carlson, L., Bigham, J. M., Schwertmann, U., Kyek, A., and Wagner, F. (2002). Scavenging of As from acid mine drainage by schwertmannite and ferrihydrite: A comparison with synthetic analogues. *Environmental Science & Technology*, 36(8):1712–1719.

Casteel, S. W., Weis, C. P., Henningsen, G. M., and Brattin, W. J. (2006). Estimation of relative bioavailability of lead in soil and soil-like materials using young swine. *Environmental Health Perspectives*, 114(8):1162–1171.

Cheng, H., Hu, Y., Luo, J., Xu, B., and Zhao, J. (2009). Geochemical processes controlling fate and transport of arsenic in acid mine drainage (AMD) and natural systems. *Journal of Hazardous Materials*, 165(1-3):13–26.

Corkhill, C. and Vaughan, D. (2009). Arsenopyrite oxidation - a review. *Applied Geochemistry*, 24(12):2342–2361.

Cornell, R. M. and Schwertmann, U. (2003). *Iron Oxides: Structure, Properties, Reactions, Occurrences, and Uses*. Wiley-VCH Verlag GmbH & Co. KGaA, Weinheim.

CRC (2007). CRC handbook of chemistry and physics, 88th edition.

Csavina, J., Field, J., Felix, O., Corral-Avitia, A. Y., Saez, A. E., and Betterton, E. A. (2014). Effect of wind speed and relative humidity on atmospheric dust concentrations in semi-arid climates. *Science of the Total Environment*, 487:82–90.

Deng, Y. and Arvide, M. G. T. (2011). Automation of size fractionation to extract clays and silts. *Clay Minerals*, 46(3):515–523.

Deng, Y., White, G. N., and Dixon, J. B. (2012). *Soil Mineralogy Laboratory Manual*. Published by the authors, Department of Soil and Crop Sciences, Texas A&M University, College Station, Texas 77843-2474, 14 edition.

Dove, P. M. and Rimstidt, D. J. (1985). The solubility and stability of scorodite, $Fe^{3+}As^{5+}O_4 \cdot 2\,H_2O$. *American Mineralogist*, 70:838–844.

Drahota, P. and Filippi, M. (2009). Secondary arsenic minerals in the environment: A review. *Environment International*, 35(8):1243–55.

Dutrizac, J. E. and Jambor, J. L. (2000). Jarosites and their application in hydrometallurgy. *Reviews in Mineralogy and Geochemistry*, 40(1):405–452.

Espinosa, E., Armienta, M. A., Cruz, O., Aguayo, A., and Ceniceros, N. (2009). Geochemical distribution of arsenic, cadmium, lead and zinc in river sediments

affected by tailings in Zimapan, a historical polymetalic mining zone of Mexico. *Environmental Geology*, 58(7):1467–1477.

Figueiredo, M. O. and da Silva, T. P. (2011). The positive environmental contribution of jarosite by retaining lead in acid mine drainage areas. *International Journal of Environmental Ressearch and Public Health*, 8(5):1575–82.

Garcia, G. and Querol, F. (1991). Description of some deposits in the Zimapan District, Hidalgo: The geology of North America. *The Geology of North America*, v. P-3:295–313.

Giere, R., Sidenko, N. V., and Lazareva, E. V. (2003). The role of secondary minerals in controlling the migration of arsenic and metals from high-sulfide wastes (Berikul gold mine, Siberia). *Applied Geochemistry*, 18(9):1347–1359.

Guggenheim, S. and Martin, R. T. (1995). Definition of clay and clay mineral: Joint report of the aipea nomenclature and CMS nomenclature committees. *Clays and Clay Minerals*, 43(2):255 – 256.

Hammarstrom, J. M., Seal, R. R., Meier, A. L., and Kornfeld, J. M. (2005). Secondary sulfate minerals associated with acid drainage in the eastern US: recycling of metals and acidity in surficial environments. *Chemical Geology*, 215(1-4):407–431.

Harvey, M. C., Schreiber, M. E., Rimstidt, J. D., and Griffith, M. M. (2006). Scorodite dissolution kinetics: Implications for arsenic release. *Environmental Science & Technology*, 40:6709–6714.

Hayes, S. M., Webb, S. M., Bargar, J. R., O'Day, P. A., Maier, R. M., and Chorover, J. (2012). Geochemical weathering increases lead bioaccessibility in semi-arid mine tailings. *Environmental Science & Technology*, 46(11):5834–41.

Hildebrand, M. and J.L. Lerch, S. (2015). Diatom silica biomineralization: Parallel development of approaches and understanding. *Seminars in Cell & Developmental*

Biology, 46:27–35.

IARC (2012). Arsenic, metals, fibres, and dusts. *IARC monographs on the evaluation of carcinogenic risks to humans / World Health Organization, International Agency for Research on Cancer*, 100(Pt C):11–465.

INEGI (2010). Censo de poblacion y vivienda. *INEGI*.

Johnson, D. B. and Hallberg, K. B. (2005). Acid mine drainage remediation options: a review. *Science of the Total Environment*, 338(1-2):3–14.

Kalin, M., Fyson, A., and Wheeler, W. N. (2006). The chemistry of conventional and alternative treatment systems for the neutralization of acid mine drainage. *Science of the Total Environment*, 366(2-3):395–408.

Kempton, H. and Atkins, D. (2000). Delayed environmental impacts from mining in semi-arid climates. In *In Proceedings from the Fifth International Conference on Acid Rock Drainage*, volume Vol. 2, pages 1299–1308. Published by Society for Mining, Metallurgy, and Exploration, Inc.

Khalil, A., Hanich, L., Bannari, A., Zouhri, L., Pourret, O., and Hakkou, R. (2013). Assessment of soil contamination around an abandoned mine in a semi-arid environment using geochemistry and geostatistics: Pre-work of geochemical process modeling with numerical models. *Journal of Geochemical Exploration*, 125:117–129.

Kuyucak, N. (2012). Acid mine drainage prevention and control options. *Mine, Water and Environment*, 1999 IMWA Congress(Sevilla, Spain).

Labastida, I., Armienta, M. A., Lara-Castro, R. H., Aguayo, A., Cruz, O., and Ceniceros, N. (2013). Treatment of mining acidic leachates with indigenous limestone, Zimapan Mexico. *Journal of Hazardous Materials*, 262:1187–95.

Li, Z. and Qvarfort, U. (1996). Predicting the mobillity of zn, fe, cu, pb, cd from roasted sulfide(pyrite) residues - a case study of wastes from the sulfuric acid

industry in sweden. *waste management*, 16(8):671–681.

Lu, D., Wang, W., Chang, Y., Xie, F., and Jiang, K. (2016). Thermodynamic analysis of possible chalcopyrite dissolution mechanism in sulfuric acidic aqueous solution. *Metals*, 6(12):303.

Majzlan, J., Drahota, P., and Filippi, M. (2014). Parageneses and crystal chemistry of arsenic minerals. *Reviews in Mineralogy and Geochemistry*, 79(1):17–184.

McClure, R. J. (2012). *Mineralogy and Geochemistry of Pb, Zn and Ag Mine Tailings Originating from Carbonate-Rich Deposits*. Thesis, Texas A&M University.

McLean, J. E. and Bledsoe, B. E. (1992). Behavior of metals in soils.

Meendez, M. and Armienta, M. A. (2003). Arsenic phase distribution in Zimapan mine tailings, Mexico. *Geofisica Internacional*, 42(1):131–140.

Moncur, M., Jambor, J., Ptacek, C., and Blowes, D. (2009). Mine drainage from the weathering of sulfide minerals and magnetite. *Applied Geochemistry*, 24:2362 – 2373.

Ongley, L. K., Armienta, A., and Mango, H. (2003). Concentrations of heavy metals in soil, Zimapan, Mexico. *Journal de Physique*, IV(107).

Ongley, L. K., Armienta, M. A., Heggeman, K., Lathrop, A. S., , Mango, H., Miller, W., and Pickelner, S. (2001). Arsenic removal from contaminated water by the Soyatal Formation, Zimapan Mining District, Mexico - a potential low-cost low-tech remediation system. *AEG/Geological Society*, 1:23–31.

Ongley, L. K., Sherman, L., Armienta, A., Concilio, A., and Salinas, C. F. (2007). Arsenic in the soils of Zimapan, Mexico. *Environmental Pollution*, 145(3):793–9.

Ramirez-Aldaba, H., Valles, O. P., Vazquez-Arenas, J., Rojas-Contreras, J. A., Valdez-Perez, D., Ruiz-Baca, E., Meraz-Rodriguez, M., Sosa-Rodriguez, F. S., Rodriguez, A. G., and Lara, R. H. (2016). Chemical and surface analysis during evolution of arsenopyrite oxidation by acidithiobacillus thiooxidans in the pres-

ence and absence of supplementary arsenic. *Science of The Total Environment*, 566-567:1106–1119.

Ranjan, R., Rani, R., Bavishi, A., Sharma, S., and Choudhary, M. (2012). Speciation of arsenic across water-sediment interface of Falgu River. *American Journal of Environmental Sciences*, 8(6):615–621.

Razo, I., Carrizales, L., Castro, J., Diaz-Barriga, F., and Monroy, M. (2004). Arsenic and heavy metal pollution of soil water and sediments in a semi arid climate mining area in Mexico. *Water, Air, and Soil Pollution*, 152:129–152.

Roca, A., Vinals, J., Arranz, M., and Calero, J. (1999). Characterization and alkaline decomposition/cyanidation of beudantite jarosite materials from Rio Tinto gossan ores. *Canadian Metallurgical Quarterly*, 38(2):93–103.

Romero, F. M., Armienta, M. A., and Carrillo-Chavez, A. (2004). Arsenic sorption by carbonate-rich aquifer material, a control on arsenic mobility at Zimapan, Mexico. *Archives of Environmental Contamination and Toxicology*, 47:1–13.

Romero, F. M., Armienta, M. A., and Gonzalez-Hernandez, G. (2007). Solid-phase control on the mobility of potentially toxic elements in an abandoned lead/zinc mine tailings impoundment, Taxco, Mexico. *Applied Geochemistry*, 22(1):109–127.

Romero, F. M., Armienta, M. A., Gutierrez, M. E., and Guadalupe, V. (2008). Geological and climatic factors determining hazard and environmental impact of mine tailings. *Revista internacional de contaminacion ambiental*, 24(2):43–54.

Romero, F. M., Nunez, L., Gutierrez, M. E., Armienta, M. A., and Ceniceros-Gomez, A. E. (2011). Evaluation of the potential of indigenous calcareous shale for neutralization and removal of arsenic and heavy metals from acid mine drainage in the Taxco mining area, Mexico. *Archives of Environmental Contamination and Toxicology*, 60(2):191–203.

Savage, K. S., Bird, D. K., and O'Day, P. A. (2005). Arsenic speciation in synthetic

jarosite. *Chemical Geology*, 215(1-4):473–498.

Simons, F. S. and Mapes V., E. (1956). Geology and ore deposits of the Zimapan mining district state of Hidalgo Mexico. *Geological Survey Professional Paper 284*.

Skougstad, M. and Horr, A. C. (1963). Occurence and distribution of strontium in natural water. *Geological Survey*, 1496-D.

Smart, R. S., Miller, S. D., Stewart, W. S., Rusdinar, Y., Schumann, R. E., Kawashima, N., and Li, J. (2010). In situ calcite formation in limestone-saturated water leaching of acid rock waste. *Science of the Total Environment*, 408(16):3392–402.

Smeaton, C. M., Walshe, G. E., Smith, A. M., Hudson-Edwards, K. A., Dubbin, W. E., Wright, K., Beale, A. M., Fryer, B. J., and Weisener, C. G. (2012). Simultaneous release of Fe and As during the reductive dissolution of Pb-As jarosite by Shewanella putrefaciens CN32. *Environmental Science & Technology*, 46(23):12823–31.

Smith, A. M. L., Dubbin, W. E., Wright, K., and Hudson-Edwards, K. A. (2006). Dissolution of lead- and lead-arsenic-jarosites at ph 2 and 8 and 20C: Insights from batch experiments. *Chemical Geology*, 229(4):344–361.

Smith, P. G., Koch, I., Gordon, R. A., Mandoli, D. F., Chapman, B. D., and Reimer, K. J. (2005). X-ray absorption near edge structure analysis of arsenic species for application to biological environmental samples. *Environmetnal Science & Technology*, 39(1):248–254.

Sracek, O., Armienta, M. A., Rodriguez, R., and Villasenor, G. (2010). Discrimination between diffuse and point sources of arsenic at Zimapan, Hidalgo state, Mexico. *Journal of Environmental Monitoring*, 12(1):329–37.

Stoffregen, R. E., Alpers, C. N., and Jambor, J. L. (2000). Alunite-jarosite crystallography, thermodynamics, and geochronology. *Reviews in Mineralogy and Geo-*

chemistry, 40(1):453–479.

Stuben, D., Berner, Z., Kappes, B., and Puchelt, H. (2001). Environmental monitoring of heavy metals and arsenic from Ag-Pb-Zn mining a case study over two millennia. *Environmental Monitoring and Assessment*, 70:181–200.

Tchounwou, P. B., Yedjou, C. G., Patlolla, A. K., and Sutton, D. J. (2012). Heavy metal toxicity and the environment. *Experientia Supplementum*, 101:133–64.

Vodyanitskii, Y. N. (2009). Mineralogy and geochemistry of manganese: A review of publications. *Eurasian Soil Science*, 42(10):1170–1178.

Yadav, S. K. (2010). Heavy metals toxicity in plants: An overview on the role of glutathione and phytochelatins in heavy metal stress tolerance of plants. *South African Journal of Botany*, 76(2):167–179.

Zeng, W., Qiu, G., and Chen, M. (2013). Investigation of cu-s intermediate species during electrochemical dissolution and bioleaching of chalcopyrite concentrate. *Hydrometallurgy*, 134-135:158–165.

Zhang, X., Jia, Y., Wang, S., Pan, R., and Zhang, X. (2012). Bacterial reduction and release of adsorbed arsenate on Fe(III)-, Al- and coprecipitated Fe(III)/Al-hydroxides. *Journal of Environmental Sciences*, 24(3):440–448.

Zvimba, J. N., Mulopo, J., Bologo, L. T., and Mathye, M. (2012). An evaluation of waste gypsum-based precipitated calcium carbonate for acid mine drainage neutralization. *Water Science & Technology*, 65(9):1577–82.